Six Degree of Freedom Flight Dynamics Model of a Tilt-Wing Aircraft with Trim and Stability Analysis

Implemented on the Canadair CL-84 Dynavert for Hover and Transition

Nadav Eldar

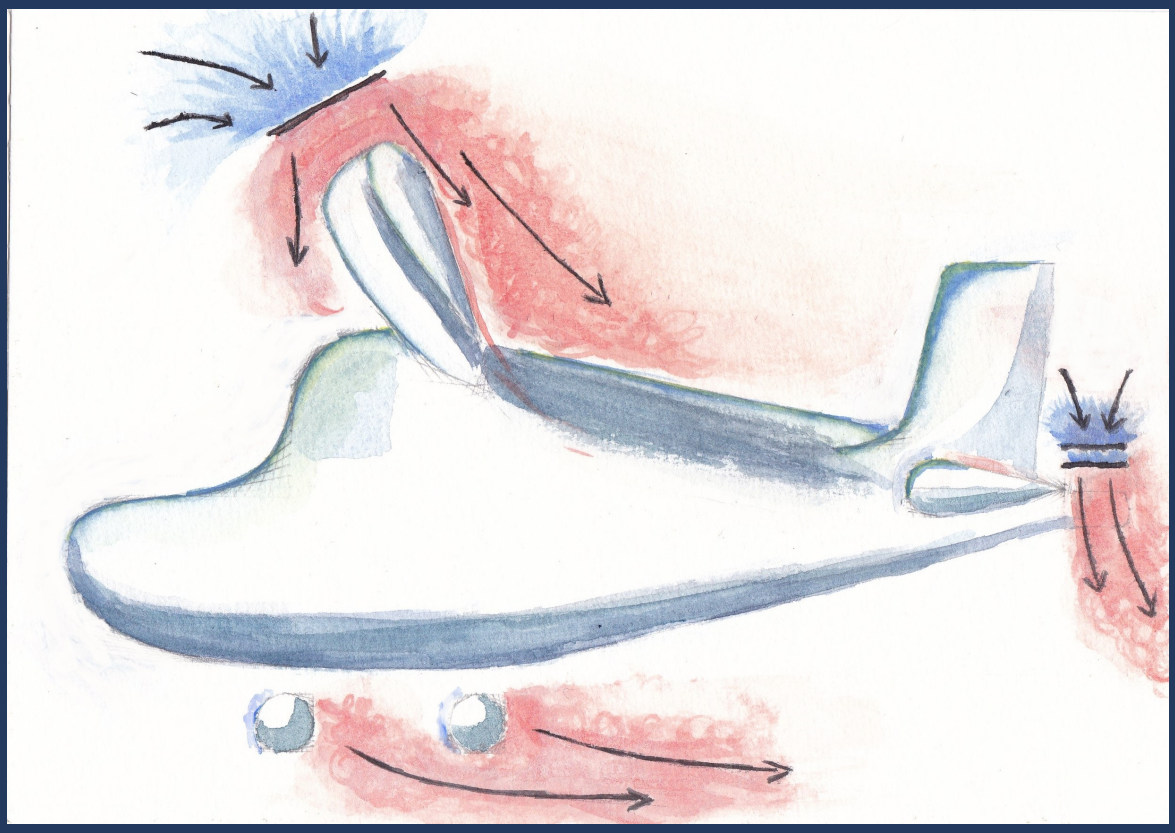

TU Delft

Six Degree of Freedom Flight Dynamics Model of a Tilt-Wing Aircraft with Trim and Stability Analysis

Implemented on the Canadair CL-84 Dynavert for Hover and Transition

Thesis report

by

Nadav Eldar

to obtain the degree of Master of Science
at the Delft University of Technology
to be defended publicly on September 17, 2024 at 10:00

Thesis committee:

Chair:	Prof.Dr. E.J. van Kampen
Supervisors:	Dr. Marilena Pavel
Place:	Faculty of Aerospace Engineering, Delft
Project Duration:	December, 2023 - September, 2024
Student number:	5704383

An electronic version of this thesis is available at
https://brightspace.tudelft.nl/d2l/le/content/560234/Home.

Faculty of Aerospace Engineering · Delft University of Technology

Contents

Nomenclature

List of Abbreviations

AAM	Advanced Air Mobility
CG	Center of Gravity
kW	Kilowatt
SAS	Stability Augmentation System
shp	Shaft Horsepower
UAV	Unmanned Areal Vehicle
V/STOL	Vertical and/or Short Take-off and Landing

List of Symbols

α	Angle of attack [rad]
α_c	Angle of attack of the control plane [rad]
$\bar{c}$	Average wing chord [m]
$\bar{c}_e$	Average elevator chord [m]
$\bar{c}_f$	Average flap chord [m]
$\bar{c}_w$	Average wing chord [m]
$\bar{q}$	Dynamic pressure $\frac{1}{2}\rho {V_\infty}^2$ [$\frac{N}{m^2}$]
$\bar{q}_s$	Slipstream dynamic pressure $\frac{1}{2}\rho {V_s}^2$ [$\frac{N}{m^2}$]
β	Angle of side slip [rad]
$\boldsymbol{\Omega}$	Vector of rotational velocity components $[p, q, r]$ in the body reference frame [$\frac{rad}{s}$]
$\boldsymbol{F}$	Vector of force components $[X, Y, Z]$ in the body reference frame [N]
$\boldsymbol{I}$	Matrix of moment inertia in the body reference frame [$kg \cdot m^2$]
$\boldsymbol{M}$	Vector of force components $[L, M, N]$ in the body axis [Nm]
$\boldsymbol{v_i}$	Eigenvector corresponding to the i^{th} eigenvalue
$\boldsymbol{V}$	Vector of translational velocity components $[u, v, w]$ in the body reference frame [$\frac{m}{s}$]
δ_a	Aileron deflection [rad]
δ_e	Elevator deflection [deg]
δ_f	Flap deflection [deg]
δ_{HS}	Movable horizontal tailplane incidence [deg]
δ_r	Rudder deflection [rad]
ϵ	Downwash angle [rad]
η	Wing tilt angle [rad]
γ	Flight path angle [rad]
λ_c	Coefficient of inflow velocity at the control plane $\lambda_c = \frac{V sin\alpha_c}{\Omega R}$
λ_i	Coefficient of rotor induced velocity
μ	Advance ratio $\mu = \frac{V cos\alpha_c}{\Omega R}$
Ω	Rotor angular velocity [$\frac{rad}{s}$]
ϕ	Roll angle [rad]
ψ	Directional angle [rad]
ρ	Air density at sea level [$\frac{kg}{m^3}$]
θ	Pitch angle [rad]
ζ	Angle of slipstream [rad]
$c_{d_{of}}$	Fuselage zero-lift drag coefficient
c_{db}	Basic drag coefficient for cylindrical bodies
c_{l_α}	Lift coefficient of (propeller) blade element
$c_{l_{W-o}}$	Lift coefficient of the wing at $\alpha = 0$
c_{l_W}	Lift coefficient of the wing
C_T	Thrust coefficient normalized by $T = C_T \pi \rho (\Omega R)^2 R^2$
D_W	Drag force generated by the wing [N]
D_e	Drag force generated by the elevator [N]
D_F	Drag force generated by the fuselage [N]

D_{HS} Drag force generated by the horizontal stabilizer [N]

D_N Drag force generated by the nacelles [N]

F_f Fuselage equivalent plate area for drag estimate [m^2]

I_{ij} Moment of inertia about the i-j plane [$kg \cdot m^2$]

L Rolling moment [Nm]

l Wingspan [m]

L_i Moment about the body x-axis generated by component i. E.g. M_P for propulsive, Z_W for wing, etc... [Nm]

L_W Lift force generated by the wing [N]

L_e Lift force generated by the elevator [N]

L_F Lift force generated by the fuselage [N]

L_{HS} Lift force generated by the horizontal stabilizer [N]

L_N Lift force generated by the nacelles [N]

M Pitching moment [Nm]

M_i Moment about the body y-axis generated by component i. E.g. M_P for propulsive, Z_W for wing, etc... [Nm]

M_{AC_W} Moment generated by the wing at the aerodynamic center [Nm]

M_{AC_e} Moment generated by the elevator at the aerodynamic center [Nm]

$M_{AC_{HS}}$ Moment generated by the horizontal stabilizer at the aerodynamic center [Nm]

N yawing moment [Nm]

N_i Moment about the body z-axis generated by component i. E.g. M_P for propulsive, Z_W for wing, etc... [Nm]

p Roll rate [$\frac{rad}{s}$]

q Pitch rate [$\frac{rad}{s}$]

R Rotor radius [m]

r Yaw rate [$\frac{rad}{s}$]

S_F Fuselage cross-sectional area [m^2]

S_I Wing planform area inside slipstream [m^2]

S_P Rotor surface area [m^2]

T_i Thrust produced by rotor i [N]

u Velocity component along the body x-axis [$\frac{m}{s}$]

v Velocity component along the body y-axis[$\frac{m}{s}$]

V_∞ Free stream velocity [$\frac{m}{s}$]

V_s Slipstream inflow velocity [$\frac{m}{s^2}$]

W Aircraft weight [N]

w Velocity component along the body z-axis [$\frac{m}{s}$]

X_i Force in the body x-axis generated by component i. E.g. X_P for propulsive forces, X_W for wing forces, etc... [N]

x_i Distance from location i to the C.G. along the body x-axis [m]

Y_i Force in the body y-axis generated by component i. E.g. Y_P for propulsive forces, Y_W for wing forces, etc... [N]

y_i Distance from location i to the C.G. along the body y-axis [m]

Z_i Force in the body z-axis generated by component i. E.g. Z_P for propulsive forces, Z_W for wing forces, etc... [N]

z_i Distance from location i to the C.G. along the body z-axis [m]

$\Delta_{c_{l_{flap,max}}}$ Max increase in lift coefficient by full flap deflection

θ_0 Propeller blade collective pitch [rad]

C_{l_v} Dihedral stability derivative $C_{l_v} = \frac{\Delta L}{\Delta v} \cdot \frac{V_\infty}{\bar{q}Sl}$

C_{m_u} Speed stability derivative $C_{m_u} = \frac{\Delta M}{\Delta u} \cdot \frac{V_\infty}{\bar{q}S\bar{c}}$

C_{m_w} Incidence stability derivative $C_{m_w} = \frac{\Delta M}{\Delta w} \cdot \frac{V_\infty}{\bar{q}S\bar{c}}$

C_{n_v} Weathercock stability derivative $C_{n_v} = \frac{\Delta N}{\Delta v} \cdot \frac{V_\infty}{\bar{q}Sl}$

List of Figures

List of Tables

Part I

Literature Review & Research Definition

1

Introduction

Flight dynamics models provide valuable insight into the behaviour of vehicles at many stages of life. Fully developed vehicles benefit from flight dynamics models to design powerful controllers that improve performance and robustify them to unforeseen disturbances. Engineers in the mid-stages of vehicle design lean on models to help optimize costly flight tests by predicting the vehicle's behaviour, in some cases even replacing flight tests altogether. Low-fidelity models are also helpful in the early stages of design to approximate the behaviour of a conceptual vehicle and determine the viability of the design configuration.

The purpose of this report is to explore the flight mechanics of a tilt wing configuration aircraft with thrust vectors aligned with the wing chord. Understanding such an aircraft's mechanics and modeling its dynamics provides insight valuable to conceptual design tasks that consider the tilt wing configuration. As will be explore in Chapter 2, existing flight dynamics models for tilt wing aircraft rely on experimental and flight test data with protected access. These methods rely on large amounts of proprietary data about how the aircraft behaves at specific flight conditions to extrapolate a continuous model. This report adopts the alternative approach of estimating the behavioural factors of the aircraft using analytical means. Therefore, this report will endeavour to produce a low-fidelity model that can approximately predict the behaviour of a tilt wing aircraft. This model will be implemented on the Canadair CL-84 Dynavert tilt wing.

The following research questions are identified for investigation in this report. The principal interest lies in the flight dynamic characteristics of the tilt-wing configuration. This area of interest leads to the first research question.

Research Question 1

What are the flight dynamic characteristics of the non-linear model of a tilt-wing aircraft?

To address Research Question 1, a flight dynamics model needs to be designed. To keep verification at the center of the process, a three degree of freedom should be designed and verified before adding the complications of a six degree of freedom model. Within the understanding of the flight dynamic characteristics of the tilt wing configuration, the wing tilt transition is a very important component. As such, the research will require an understanding of the aircraft at many operating points inside this transition, introducing another research question.

Research Question 2

What is the trim corridor of a tilt-wing aircraft?

Indeed, it is important to observe the behaviour of the aircraft at trim throughout the wing tilt transition. However, the trim configuration obtained by the model at these operating points needs to be evaluated for reliability. Again, verification and validation is a crucially part of this research, without which the conclusions of this report are undermined.

Research Question 3

How can the non-linear model, implemented on Canadair's CL-84 Dynavert tilt-wing, be validated against flight test data?

Although limited, some data exists that can be used as validation for the model. The answer to Research Question 3 directly impacts the quality of the research put forward in this work. To develop the analysis of the natural behaviour of the aircraft throughout its wing tilt transition envelope, the so-called transition corridor of the aircraft should be considered in particular.

Research Question 4

What is the impact of the angle of wing tilt on the general dynamics and in particular on the stability? Similarly, what is the impact of the airspeed on these dynamics?

Research Question 4 proposes to use the model to perform some preliminary analysis of the tilt wing configuration. Answering this question sets the stage for further development of the research into tilt wing aircraft. Motivated by the questions, the research objective is formulated in steps.

Research Objective

- Develop a non-linear 3 degree of freedom longitudinal flight dynamics model of a tilt-wing aircraft.
- Study the trim, validate the model, and establish a flight envelope.
- Extend the non-linear flight dynamics model to 6 degrees of freedom with lateral and directional dimensions.
- Study the trim, validate the model, and establish a flight envelope.
- Linearize the 6 degree of freedom model and analyse the characteristics.

The model will be implemented on the Canadair CL-84 Dynavert using information available from Taylor (1960) and Nieusma (1993). The geometry used in the model can be found in Appendix B.

2

Literature Review

2.1. Vertical Take-Off and Landing

The purpose of this literature review is to provide and overview of what are tilt wing configuration aircraft and of the state of the art in tilt-wing flight dynamics modeling. As Perez et al. (2023) point out, the development of Urban Air Mobility (UAM) raises new questions about aircraft capable of vertical take-off and landing (VTOL), including the tilt wing solution. The goal of this report is to develop a model of tilt wing flight dynamics adapted for iterative design based on geometry rather than test data or computation fluid dynamic analysis. To do so, the evolution of tilt-wing technology and the flight control tools of such configurations need to be examined.

First, Section 2.2 will start with an introduction to tilt-wing aircraft, including its history and some of the advantages and disadvantages of this configuration. Then, Section 2.3 will present known challenges to developing flight dynamic models and the state-of-the-art in doing so for tilt-wing configurations. The CL-84 holds a place of special emphasis in this review: thanks to the data available on this aircraft, it is selected as a test case for the model developed in this report.

2.2. History of Tilt Wing Aircraft

This section discusses the history and background of tilt-wing aircraft. Research into V/STOL capable aircraft outside the scope of helicopters began in the mid-1950s with many different types of configurations, including convertiplanes, vectored thrust, tilt-rotors, and tilt-wings (Chana and Sullivan, 1994). In the technological expansion of the post WWII era, helicopters had already become a familiar technology with proven advantages, but also known limitations. Chana and Sullivan (1994) highlight the economic and operational limitations of the helicopters, while underlining the gap in technology for a vehicle with hybrid vertical take-off and efficient cruise capability. They also predicts a come-back for tilt-wing configuration, comparing it favourably with the tilt-rotor configuration. In recent years the industry of aerial transportation has once again began to reevaluate novel configurations in a revolutionary way. At the root of the current revolution are improvements in electric technology and structural materials and several players are racing to certify their vehicle, with for example Archer, Joby, Lilium, Volocopter, etc.... To anticipate the coming innovations that will undoubtedly emerge from this context, the tilt wing configuration will be examined in this report.

Although there is no formal definition of tilt-wing aircraft, the configuration is broadly described by a patent by Kress and Gebhard (1991): “The wing is pivotally mounted on the fuselage for rotation from a cruise position in which the upper surface of the wing is flush with the upper surface of the fuselage to a hover position in which the wing is perpendicular to the upper surface of the fuselage”. When the wing pivots, the thrust vector for each engine mounted on the wings also rotates. Thus the direction of thrust ranges, along with the rotation of the wing, from horizontal to vertical. In general, in order to be fully capable to vertical flight, the wings should tilt through at least 90° so as to range from fully aligned with the vertical axis to fully flush with the fuselage’s horizontal axis. For example, the Canadair CL-84 Dyanvert tilts from 2° to 102° relative to the fuselage horizontal plane, amounting to a baseline 2° incidence angle for the wing in cruise configuration (Michaelsen, 1971).

The trade-off for optimizing both cruise and hover comes at the expense of mechanical and predictive complexity. Several solutions for tilt-wing were explored in the 50s through to the mid-70s when the

CL-84's took her last flight. Efforts were renewed to revisit the concept in the 90s, unfortunately resulting in the cancellation of the Ishida TW-68. According to Totah (1992), technological advances in "materials, thrust/power systems, and fly-by-wire control system [and] state-of-the-art augmentation and optimization techniques to yield improved handling qualities" were all factors responsible for a resurgence in interest in tilt-wing aircraft. Even though the efforts of those brilliant minds in the 90s took some time to find traction, NASA eventually developed the Greased Lightning GL-10 in 2014 and Airbus the Vahana A^3 between 2016 and 2019, both modern examples of what tilt-wings can be. Following this trend, and in the context of rapidly expanding interest in Advanced Air Mobility (AAM) development, it seems likely that the tilt-wing configuration will attract more attention in the coming years. Their unique capability for long range endurance coupled with a respectable ability to hover with far less download than tilt-rotors (Chana and Sullivan, 1994) makes tilt-wings ideal for a wide range of applications such as search-and-rescue operations, long-distance freight or passenger transport to places with difficult access, urban air mobility, not to mention recreational uses.

According to Chana and Sullivan (1994), the first tilt-wing aircraft to be developed was Boeing's Vertol VZ-2 featured in Figure 2.1. Development began in 1956, the first vertical flight executed in August of 1957, and the first horizontal flight in January 1958. This aircraft claimed the first complete transition in July 1958. This trail-blazer completed 450 flights and 34 transitions before its last flight in 1965 (VFS, 2024). In its hover configuration, the VZ-2 used ducted fans mounted on the empennage for pitch and yaw control, and a differential thrust collective for roll control. In cruise configuration, it was fitted with differential flaperons for roll, a rudder for yaw, and a full motion horizontal stabilizer for pitch. The empennage ducted fans were available in all phases of flight (Totah, 1992). Two other early tilt-wing aircraft entered various stages of design but never took flight: the Weserflug P.1003 in 1938 was never built, and the Kaman K-16B (1959) which only reached the stage of preliminary tests (Taylor, 1960). The Hiller X-18, Figure 2.2, began development in 1957 but never hovered successfully due to delays in pitch control commands. This heavy-lifter capable of 33,000 lb maximum take-off weight was mounted with two counter-rotating propellers on each wing, but unfortunately only reach a wing transition angle of 33° before the project was discontinued (VFS, 2024). By contrast, the LTV-HIller-Ryan XC-142A enjoyed more promising outcomes. With the successful transition of the wings through 100°, it was able to hover even in tailwind conditions. In hover configuration the fuselage pitch attitude was controlled with variable pitch tail rotor. Roll was controlled just like a helicopter with cyclic propeller pitch, and yaw was controlled using the ailerons activated by the rotor slipstream. Although 5 were built and accumulated 420 flight hours, there were structural issues that resulted in the discontinuation of this model (VFS, 2024).

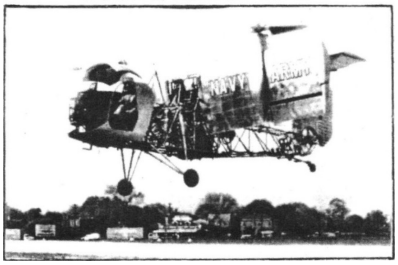

Figure 2.1: Vertol VZ-2 (Chana and Sullivan, 1994).

Figure 2.2: Hiller X-18 (Chana and Sullivan, 1994).

Figure 2.3: XC-142A (Chana and Sullivan, 1994).

Figure 2.4: Canadair CL-84 (Chana and Sullivan, 1994).

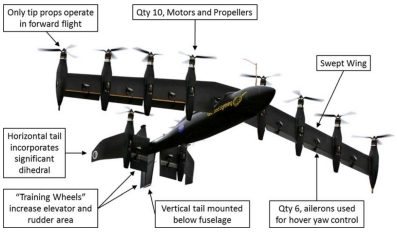

Figure 2.5: GL-10 (Fredericks et al., 2017).

Figure 2.6: Vahana A^3 (VFS, 2020).

In 1963 the development of the Canadair CL-84 Dynavert began, with a first flight in May 1965 (VFS, 2024). The CL-84 was fitted with traditional fixed-wing flight controls in the cockpit with a control stick for pitch and roll commands and pedals for yaw inputs, these were linked through a mixing box to different control surfaces depending on the wing tilt configurations. The aircraft was fitted with full length ailerons/flaps on the wing trailing edge, leading edge slats, a full motion stabilizer, a rudder, as well as variable pitch propellers and a tail rotor. Altogether this aircraft had 11 actuated controls, with the marked absence of an helicopter-like swashplate on the main rotors. A succinct tabular summary of the fly-by-wire system can be found in (Longhurst, 1966) and is reproduced in Table 2.1.

Table 2.1: CL-84 control system (Longhurst, 1966)

Axis	Cruising Flight	Transition Inbound (to hover)	Hovering Flight
Pitch	Stick to elevator	Stick to elevator active and tail rotor active	Stick to tail rotor active
Roll	Stick to flap/aileron	Stick to flap/aileron phase out and stick to differential propeller pitch phased in	Stick to differential propeller pitch
Yaw	Pedals to rudder	Pedals to flap/aileron phase in and differential propeller pitch phased progressively in and out	Pedals to flap/aileron
Height	Power lever to engine thrust	Power lever to collective propeller pitch phased in	Power lever to engine and collective propeller pitch

Note: Transition outbound is the reverse of transition inbound

Further, it is noted that as the wing tilt angle transitions to conventional cruise configuration, differential thrust effectiveness in roll is gradually replaced by yaw, and the reverse is true for the differential flaps/ailerons. In (Longhurst, 1966) it is clarified that during this transition of control effectiveness, “the differential thrust yields pro-yaw for roll demand and pro-roll for yaw demand, while the differential flaps give adverse yaw and adverse roll, respectively”. Thanks to this effect and its powerful SAS mixing box, both command mechanisms were applied together in transition with scheduled gains for both yaw and roll pilot inputs, such that only the demanded input was observed by the aircraft and the undesirable effect was cancelled by careful control allocation. As a result, the CL-84 can perform pure roll and pure yaw manoeuvres throughout its transition with the same effectiveness as in hover configuration.

Four CL-84 aircraft were built and underwent a number of extensive operational tests in an effort to secure a contract with either the Canadian or the U.S. defense departments, with some encouraging results. Chana and Sullivan (1994) recall some of the test pilots’ words, “The CL-84 aircraft was suitable (as demonstrated) for search and rescue, surveillance, light transport and utility type missions”, suggesting that the aircraft was adapted for many kinds of missions. The success achieved by the CL-84 in its transition and hovering capabilities is further corroborated by Michaelsen (1971) in his assessment of the aircraft’s

handling qualities. Indeed, although there was “[admittedly] considerable room for further development and improvement of the handling qualities of the aircraft, the greater desire expressed by most pilots [was] for improvements in the conventional flight regiment rather than in the V/STOL regime”. It is important to note that vast improvements have been made in handling qualities of conventional fixed-wing aircraft since those days. Ultimately the project was discontinued, for reasons that Frederick (1990) attributes to a “lack of success in a military market dominated by jet and helicopter advocates” and to the stiff competition provided by the V-22 tilt-rotor.

As one of the motivation for his own thesis, Nieusma (1993) remarks that all tilt-wing configurations up to that time featured a tail rotor to maintain pitch control in hover configuration. He explored the possibility of reducing the number of control features to simplify the complexity of the configuration. However, subsequent tilt-wing configurations that successfully entered flight test stages had more tail rotors were added, not less! This was made possible by technological advancements, particularly in distributed electric propulsion, that permitted more independence to propulsive features without significant increases in weight. Thus additional propulsive systems offer an additional redundancy safety feature instead of cannibalising weight capacity from the vehicle payload.

With the advance of technologies in electric propulsion and composite materials to address some of the vibration, noise, and control delay problems, the tilt-wing configuration was revisited by NASA in 2014 with the unmanned Greased Lightning GL-10. Similar to the CL-84, the GL-10 used a mixing box to fade aileron control from yaw at wing angle 90° to roll at wing angle 0°. Inversely, differential thrust was faded from roll control at wing angle 90° to yaw control at wing angle 0°. This aircraft also engaged in more complicated control allocation capabilities adopted from the field of unmanned areal vehicle. Pitch was controlled in hover configuration through the aft propellers and in cruise configuration through elevator deflections Fredericks et al. (2017).

Finally, between 2016 to 2019, Airbus developped the Vahana A^3 remote controlled, over-actuated proof-of-concept eVTOL just large enough for one person to fit inside. Similar to the GL-10, the Vahana was also a tandem tilt-wing, though it featured an even 4 rotors on each wing. Its 22 actuators included independent wing tilt (2), individual thrust control for each rotor (8), individual blade pitch angle control for each rotor (8), as well as two independent elevator surfaces (2) and similarly independent aileron surfaces (2), along with a static vertical stabilizer (May et al., 2021). The open-source publication of the design and development resources of this aircraft has revitalized interest in the tilt-wing configuration.

2.3. Flight Dynamics

It is very expensive to develop a totally new configuration of aircraft because its behaviour needs to be thoroughly understood. This implies extensive and expensive flight tests, which require a functional prototype. However, once a prototype exists, it is difficult and costly to make significant or iterative changes to the base design. To facilitate the design process in its most iterative stage, the mechanics of a configuration can be estimated based on predictions about how the aircraft will behave. The prediction of aerodynamic behaviour combined with an estimate of the propulsive capacity of the design paves the way for a flight dynamics model. Naturally, the accuracy of the predictive capability of a flight dynamics model depends on the selection of the elements to be included in the model and the complexity they are considered with. Durham (2013) describes in great detail the most common conventions used for fixed-wing. Similarly, van Holten and Melkert (2002) discusses common conventions used for helicopters. Since a tilt-wing flight dynamics model requires understanding both fixed and rotary wing, both resources are helpful. The art of estimating forces acting on aircraft is discussed in greater depth in Section 2.3.1 before the state of the art in tilt wing flight dynamics models is presented in Section 2.3.2.

2.3.1. Estimating Forces and Moments

There are three different kinds of methods that can be used to estimate the forces acting on an aircraft. The most rudimentary is the built-up method, using the geometry and the physics of the aircraft to estimate the forces acting on it. A more accurate method is the use of computational fluid dynamics, which makes use of flow analysis methods applied to a rendering of the object of interest. Finally, the most accurate method is to perform flight tests to measure directly the behaviour of the aircraft.

The most adapted method for representing the forces and moments acting on a aircraft depends largely on the stage of development. A common methods of estimating the aerodynamic contributions of each

component is to perform tests in wind tunnel or flight conditions and directly measure the effect of each of the aircraft's surfaces on each of the states that they affect. For example, the effect of the elevator δ_e on the pitching moment M will be measured for a range of angle of attack α, airspeeds V_∞, air density ρ, etc... and then represented as a function of those variables, $C_{M_{\delta_e}}(\alpha, \rho, V_\infty)$ (Durham, 2013). This is typically left to later stages of the design process because it requires at least a scaled prototype of the design. This is an attractive method because it can overlap significantly with certification requirements but it also implies that the dynamics and controllability results will have limited influence on the design, since it is already mostly decided. The advantage of using test data is the high accuracy obtained for each measured component. Coefficients obtained using testing methods, especially flight tests, consider the influence of many implicit parameters. Flight test data can then be arrange in look-up tables that track how parameters change with respect to other parameters. Of course, these changes need to be test for a wide array of condition, but with sufficient test data comprehensive look-up tables can be filled and interpolation can fill the gaps between flight conditions. This method yields high-fidelity and costly models. Depending on the parameter under examination it could be difficult to correctly predict which other parameters will be influential over what range. A small source of uncertainty will also come from measurement noise.

To reduce cost at earlier iterations of the design process, it is possible to approximate the wind tunnel and flight data using computational fluid dynamics (CFD). This can be done with a virtual representation of the aircraft so it is easier to use the identified flight characteristics into the design iteration process. However, high-fidelity CFD also requires a well developed design, which means that the aircraft's stability and control properties obtained in this process are not considered at the conceptual stage. Although CFD can come fairly close to test data it necessarily involves making simplifying assumptions, which increases the uncertainty in the model. This method is a great tool to refine a model during late stage iterative design to confirm design decisions.

By contrast, the build-up method, which consists in estimating all the parameters theoretically, can yield low-fidelity models capable of predicting behaviour relatively well. The accuracy of such models depend largely on the assumptions made to estimate the dynamic coefficients. This method is ideal for considering flight dynamics and control in early stage conceptual design (Lawrence et al., 2016). The build-up method can provide information about the flight dynamics of an aircraft across all flight configurations before the aircraft's design is fully decided. Therefore, although experimental data and CFD results tend to be more accurate at the tested conditions, the build up method provides insight into configurations that are not well known, such as the tilt wing. Since the CL-84 is no longer available for tests, the build-up method is the only way to explore its dynamics throughout the wing tilt transition.

In addition to these general resources for building flight dynamics models, Englar and Kirkpartick (1969) spent a lot of energy to understand how to model tilt wing aircraft via the CL-84. They did so in the context of comparing the thrust and power requirements of tilt wing and tilt rotor configurations so they were consequently not preoccupied with the natural behaviour of either configuration. Still, there are significant lessons to be drawn from this work. Namely, methods for estimating the aerodynamic forces on the wings, nacelles, and fuselage-empannage combination. In this endeavour, they publish wind tunnel data for the lift and drag coefficients of NACA63_3418 equipped with the CL-84's leading edge devices. Additionally, they propose a method for estimating the interaction between the wing-mounted rotor induced flow and the wing surface. They suggest making the assumption that the rotor slipstream produces a constant and uniform change to the effective angle of attack on the wing. Further, they suggest that this change in angle of attack can be estimated via the change in dynamic pressure due to the rotor induced flow. Despite the invaluable insight into the aerodynamic effects acting on the CL-84 in flight, Englar and Kirkpartick (1969) largely disregard the effect of the empennage. Preoccupied with thrust estimates and not stability, they make the assumption that the horizontal tail produces little lift, and therefore the weight of the aircraft is carried between the main rotors and the wings in different proportions depending on the tilt angle of the wings.

As a result, insight into the wing-tail interaction comes from another source. Gudmundsson (2014) shows that the disturbance caused by the wing on the mass of air traversed by the horizontal tail cannot be neglected. In addition to providing conceptual design approaches to estimating the aerodynamic effects of various aircraft surfaces, Gudmundsson (2014) also suggests methods for estimating the wing-tail interaction.

2.3.2. State-of-the-Art

There are considerable challenges to modeling the dynamics of tilt-wing aircraft. Although some work has been done to model the flight dynamics of tilt-rotor VTOL vehicles, Milz and Looye (2022) reiterate that such attempts for the tilt-wings are sparse. To better understand the scope of the challenge, May et al. (2021) list some of the following difficulties:

- Large angles of attack on lifting surfaces.
- Large incidence angles on propeller blades.
- Over-actuated controls.
- Rotor-wing slipstream aerodynamic integration.
- Variable pitch rotor blades.
- Propulsion-airframe aerodynamic integration.
- Shifting CG and inertia with wing tilt angles.
- Large flight envelope to include hover and cruise configurations.
- Multi function lifting surfaces - flaps/ailerons, slats, elevator.
- A SAS is typically required for tilt-wing aircraft to be controllable by a human pilot.

An early attempt to simulate the CL-84 to study its handling qualities was made by the manufacturer, Canadair, in 1965. McGregor (1965) uses an in-flight simulator to investigate delays during the operation of the CL-84 and how they might cause SAS failures. To this end, he models “the dynamics of the engine, the propeller, the blade angle servo, the governor, and the aircraft’s vertical damping term” and monitors identified sources of backlash. This model is highly simplified with a very specific intended use. As a result, the flight mechanics, aerodynamics, and propulsive models were all integrated and summarized by experimentally obtained coefficients, protected by intellectual property. This makes the model very difficult to use for reproduction or further research, especially into aircraft other than the CL-84.

In the late 1960s, NASA endeavoured to make a flight dynamic model of a 1/9 scale VTOL aircraft with 4 engines, with separate longitudinal portion (Chambers and Grafton, 1968) and lateral-directional portion (Chambers and Grafton, 1970). The model produced used stability derivatives obtained from wind tunnel experiments at specified wing-tilt angles and extrapolated between them linearly to account for the non-linearities involved in tilting the wing. Even though this model was not produced analytically and therefore requires expensive wind tunnel experiments to expand with a satisfactory amount of fidelity, it can be useful perform some basic verification of an analytical model. This model has also been used in the more recent study by Perez et al. (2023), although they had to pass a scaled virtual rendering through high-fidelity CFD to obtain a usable flight dynamics model. The special emphasis placed on the aerodynamic effects allow them to focus on the rotors’ dynamics and their interactions with the airframe and control surfaces. They used OVERFLOW to solve the Navier-Stoke equations, then the CAMRAD II solver to trim their model. Since their focus was not on the flight dynamics, but rather on the rotor wake and airframe interference, they do not present the model obtained from the OVERFLOW.

Similarly, Nieusma (1993) developed a model of the CL-84 based on available experimental data, with stability coefficients taken at prescribed wing-tilt angles. The goal of this study was to facilitate the design of future tilt-wing aircraft by testing the effectiveness of different types of flaps and control methods that might eliminate the aerodynamically costly tail rotor. His goal was to design a reasonably reliable model so that design engineers might be able to experiment with different configurations virtually. Another important point to note about this effort is that it did not considering ground effect and the reliability at and around hover did not closely match flight test data. Unfortunately, the model is wholly inaccessible. However, he supplies very convenient flight test data and critical geometry from the CL-84 to evaluate the reliability of his model. As such, this study represents a valuable source of validation information.

In a master thesis, Rubin (2018) developed an effective low-fidelity tilt-wing model based on experimental data from Dufour Aerospace’s aeRo 2. The author achieved a model for a novel aircraft using historical statistical data. Although a certain amount of complexity is introduced, with a shifting CG and a wing downwash model for example, the model is specific to an uncommon configuration, with the values of the selected stability coefficients remaining proprietary.

In addition, May et al. (2021) present a thorough mid-fidelity flight dynamics model of the Vahana A^3 that includes 3 detailed parts. This is by far the most detail model available for tilt-wing. The model is based on coefficients determined using CFD, designed to produce a pragmatic model that can be immediately used for more advanced control tasks such as performed in the follow-up article (Milz and Looye, 2022). The flight mechanics modelled responds to changes in CG via a second order polynomial fit to known CG location with respect to wing tilt angles. The tensor of moments of inertia is also considered but found to vary little enough with respect to wing tilt angles (about 3%) that it could be considered constant. A complex aerodynamic model is presented with considerations for non-linear and post-stall lift, rotor-induced slipstream, gusts, ground effect, and even vortex ring state. Finally, the propulsion model takes into account a simple battery model, individual engine torques, changing blade pitch angle, blade flapping, and gyroscopic torque. This complexity produces a model capable of backwards flight and reversing propeller directions, passing through zero blade rotations per minute. May et al. (2021) show a flight simulation through the wing tilt transition at $0°$ angle of attack, meaning a constant and level pitch attitude. This effort also features a verification of the rotor dynamics model and trim examples for specified conditions. Conveniently, it is based on the Vahana's open source data but it is based on a detailed CFD analysis of a tested aircraft. As such, this model is well adapted for experimental control methods rather than iterative design. Although this is by far the most developed flight dynamics model for a tilt-wing configuration, there is no preoccupation with the natural behaviour of the aircraft. The authors simulate some time domain performance tasks, but do not engage with the implications on the stability. Then Milz and Looye (2022), continuing this line of research, launch immediately into advanced control methods.

There also exist several models of tilt wing unmanned areal vehicles. Sanchez-Rivera et al. (2020) offer an excellent and representative example of such models. This model begins with non-linear equations of motion intended for use for the full wing tilt transition. The terms of these equations are estimated with a combination of CFD and flight tests and are not revealed. The model is demonstrated via some tracking performance through a wing tilt transition and the discussion immediately goes to control. Once again the natural behaviour of the aircraft is not discussed.

3

Project Plan

3.1. Methodology

This chapter will introduce the intended strategy to address the research questions presented in Chapter 1. The model will be developed in three distinct phases. In the first research phase a longitudinal model will be developed, featuring three degrees of freedom. Then, in the second research phase this model will be incremented with lateral-directional considerations, extending it to six degrees of freedom. Finally, the third research phase will consist in linearizing the model obtained in the second phase.

In research phase 1, the longitudinal model will have a degree of freedom along the x-axis, z-axis, and in the rotation about the y-axis. The steps taken to develop the model will follow this sequence:

1. Establish a schematic representation of the aircraft. This representation needs to include all major longitudinal forces and moments, as well as the aerodynamic angles. It will also be important to define the sign conventions for all the components acting on the aircraft.
2. Determine how the center of gravity of the aircraft changes with a varying angle of wing tilt.
3. Formulate functions for each of the aerodynamic and thrust forces acting on the aircraft. These functions will need to consider variable angles of attack as well as variable angles on wing-tilt.
4. Assemble the equations of motion and solve them for a set of defined input vectors. If applied to a set of input vectors ranging the span of all possible wing tilt angles, this will result in trim settings throughout the wing tilting transition.
5. Verify that the transition behaviour is comparable to other tilt-wing model behaviour in literature.
6. Validate the model behaviour against flight test data from the CL-84.

Research phase 2 will oversee the extension of the model developed in phase 1 with lateral-directional motion. The model will therefore be capable of describing the longitudinal motion described in research phase 1, as well as lateral motion along the y-axis and rotations about the x-axis and z-axis. The steps taken to develop the model will follow this sequence:

1. Extend the schematic representation of the aircraft. This representation will include important longitudinal, lateral, and directional forces and moments. In addition to the angle of attack at various aerodynamic surfaces, the angle of sideslip will also be defined. Naturally, this representation will define the sign conventions.
2. Formulate functions for each of the aerodynamic and thrust forces acting on the aircraft. Some of the longitudinal functions will need adjustment because the behaviour on the left and right side of the wing, including differential thrust, needs to be accounted for. These functions will still need to consider variable angles of attack as well as variable angles on wing-tilt. In addition, the lateral-directional aerodynamic functions needs to vary with the angle of sideslip.
3. Assemble the equations of motion and solve them for a set of defined input vectors. If applied to a set of input vectors ranging the span of all possible wing tilt angles, this will result in trim settings throughout the wing tilting transition.
4. Verify that the transition behaviour is comparable to the transition behaviour obtained in research phase 1. This verification will also serve as a comparison to literature by extension.

5. In the absence of lateral-directional validation data for the CL-84, a study of the static stability characteristics can be performed to validate the model's predicted stability characteristics.

Finally, research phase 3 will present a linearization of the model obtained in research phase 2. This research phase will provide insight in the natural dynamic behaviour of the aircraft, as predicted by the model. The steps taken to develop the model will follow this sequence:

1. Determine how the moments of inertia of the aircraft change with respect to the angle of wing tilt.
2. Rewrite the equations of motion so as to isolate the state derivatives.
3. Derive the new equations of motion with respect to each state and each control variable. Then, these derivatives and be evaluated at selected trim points.
4. Organize the resulting values into the state space A and B matrices, for the derivatives with respect to the states and control inputs respectively.
5. Evaluate the dynamic behaviour at a selection of wing tilt angles. This can be done by calculating the eigenvalues of the A matrix for trim point along the transition.
6. Perform an eigen mode analysis via the modal matrix to track how the natural behaviour of the aircraft model changes with the tilting of the wings.

3.2. Expected Results

One expected output of the model is a reasonable estimate of the wing tilt behaviour in the transition. During transition, it is intuitive that the aircraft should be incapable of low speed flight high tilt angles. At low angles of wing-tilt, the model is expected to resemble fixed-wing behaviour, meaning that it requires increasingly significant forward speed to maintain flight as the wing tilt approaches parallelism with respect to the fuselage waterline. Likewise, at high wing-tilt positions, the model should exhibit behaviour similar to helicopters with the additional limitation from the lack of swashplate. This means that the maximum speed of the model will be lower at higher tilt angles, simply for lack of a significant horizontal thrust vector. Therefore, the success of the model can be examined in part in the shape of the transition, when the wing-tilt angle η is plotted against forward velocity u. The general shape of the transition can be found in literature as well for some UAVs (Sanchez-Rivera et al., 2020), the Vahana (May et al., 2021). Hindson et al. (1993) even presents the CL-84 transition, as shown in Figure 3.1, considering small variations in fuselage pitch attitude.

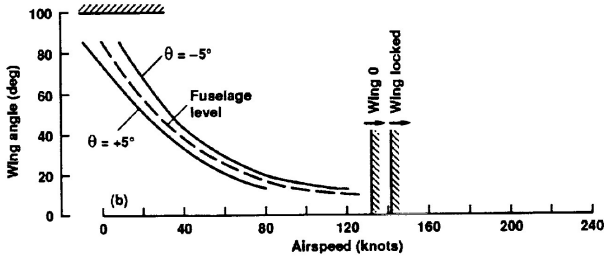

Figure 3.1: CL-84 wing tilt angle transition in forward flight (Hindson et al., 1993)

Although an excellent qualitative comparison point, very little is known about how the data used to plot Figure 3.1 was acquired. Most likely it is based on the flight envelope of the CL-84 from flight tests. As a point of comparison for the output of one tilt-wing model to another, Figure 3.2 shows the wing tilt transition at $0°$ constant fuselage pitch attitude for the Vahana flight dynamics model developed by May et al. (2021).

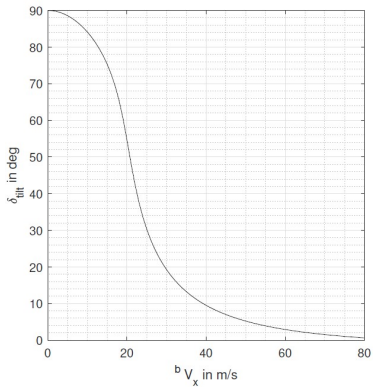

Figure 3.2: Vahana wing tilt angle transition in forward flight May et al. (2021)

In addition, it is known from Taylor (1960) that the CL-84 manual prescribed a wing-tilt angle of $85°$ for hovering flight, with higher tilt angles being reserved for flight with tailwind conditions of negative forward velocities. This is a useful reference point. Finally, the model's output can be compared to flight test data from the CL-84 that was already used for model validation (Nieusma, 1993).

Besides the transition, the control saturation can also be examined to determine whether the model is a reasonable estimate. This includes verifying that the sum of the thrust forces from all rotors does not exceed the twin engines' output capacity of 2800 shp Longhurst (1966), or approximately 2050 kW. Another control saturation indicator is the collective blade pitch angle of the propellers, bound between $-5°$ and $45°$Nieusma (1993).

The stability characteristics of the linearized model of the CL-84 can reasonably be expected to behave similar to a fixed wing aircraft at $0°$ wing tilt angle. This is because there is no difference between the CL-84 in cruise configuration and conventional fixed wing aircraft. However, in hover configuration, the CL-84 cannot be expected to behave similar to a helicopter because it is not equipped with a swash-plate and it produces thrust symmetrically. Additionally, the wing in the vertical configuration can be expected to introduce behaviour specific to the tilt wing. The usual couplings that occur in helicopters between the longitudinal states and lateral-directions states are not expected to be strong owing to the lack of swashplate. Similarly, the propeller blades do not have freedom of movement in flapping. Therefore, in general it is be expected that the longitudinal dynamics are easily separable from the lateral-directional dynamics.

In order to remain focused on the most interesting behaviours, this report places emphasis on trim conditions at unaccelerated and symmetrical flight. As a result, the linearized model will be restricted to the eight states that are most often responsible for dynamic behaviour. Fixed wing dynamics are expected to be dominant, but such models tend to prefer the state α to velocity component w and β to velocity component v, which may not be the preferable way to describe a tilt wing aircraft through the entire envelope. Because the angles of attack and sideslip are expected to vary significantly for each aerodynamics surface, it was decided to use the Cartesian velocity vectors. While the static stability of the aircraft can be examined using the non-linear 6 degree of freedom mode, the natural behaviour of the aircraft is better examine using a linear model. The format for the linear model chosen in this research is the state space representation, limited to the A and B state feedback matrices. This representation is explained in further detail in Chapter 8. The eigenvalues of the A matrix correspond to dynamic interactions between the states of the aircraft. For fixed-wing aircraft, the eigenvalues of the longitudinal A matrix, with states $[u,\ w,\ q,\ \theta]$, are most often two sets of complex conjugates with one pair closer to the imaginary axis. The pair farther away normally represents the interaction between the states q and α, characterised by high frequency, short period oscillations called the Short Period mode. Similarly, the states u and θ typically interact to form low frequency, long period oscillatory dynamics, often referred to as the Phugoid mode. It is believed (Durham, 2013) that this name originates from an etymological mistake by F.W. Lanchester in the 1908 *Aerodonetics*, who may have mistaken the root of the Greek word "to flee" for the root of "to fly". Therefore, the phugoid and short period are expected to be present in the interactions between longitudinal modes, at least when the wings are in cruise configuration. Further, a modal sensitivity analysis is expected

to show that the states w and q interact to cause the short period oscillations while the states u and θ are chiefly responsible for the phugoid dynamics.

The lateral-directional A matrix, comprised of states $[v,\ p,\ r,\ \phi]$, normally exhibits one oscillatory mode (an eigenvalues pair of complex conjugate) and two purely exponential modes, each represented by one real eigenvalue. These are known as the Dutch Roll, orchastrated by v and r, the Roll, caused by p, and the Spiral mode with ϕ at the helm. Once again, these modes are expected to be somewhat recognizable, at least when the wings are close to fixed wing configuration. The dutch roll is normally a slightly stable oscillatory mode, while the other two are non-oscillatory. The Roll mode is normally and very stable one, while the spiral mode is often on the cusp of stability if it stable at all.

3.3. Structure of the Report

The structure of the report is as follows. First, Part II presents an abridged version of the full report in the form of a publishable article. This article encapsulates the chief aspects of the methodology used to reach a six degree of freedom flight dynamics model, as well as the principal points of analysis of these models. Second, Part III provides the detailed procedure used to obtain a longitudinal flight mechanics model with three degrees of freedom, as well as some verification and validation for the output of the model. Third, Part IV details the expansion of the longitudinal model to six degrees of freedom, with lateral-directional considerations. Again, some verification and validation is provided. The fourth part, Part V of this report is dedicated to the linearization of the six degree of freedom model and the analysis of the linearized models. Finally, the report closes with concluding remarks and recommendations in Part VI.

Part II

Scientific Article

Six Degree of Freedom Flight Dynamics Model of a Tilt-Wing Aircraft with Trim and Stability Analysis

Nadav Eldar. *
Control and Simulation Section, Faculty of Aerospace Engineering,
Delft University of Technology, Delft, The Netherlands

One of the biggest trade-offs in aviation is between a vehicle's ability to take-off and land vertically and its efficiency in cruising flight. The recent drive for electric vehicles creates space to consider new solutions to this trade-off. Tilt wing aircraft offer significant advantages in vertical take-off and landing (VTOL) operations due to their versatile design. One of the difficulties in designing configurations with little historical data is that they are difficult to predict. The challenge of formulating a flight dynamics model valid through the transition phase from vertical to horizontal flight is undertaken in this study. This research aims to investigate the tilt wing aircraft behaviour through the wing tilt transition, as well as the stability characteristics. A six degree of freedom model implemented on the Canadair CL-84 Dynavert compares favourably to flight test data, albeit with low-fidelity especially around hovering flight. The likely cause is the simple rotor to wing slipstream interference modelled. The stability characteristics reveal large spikes in positive stability of the longitudinal derivative C_{m_u} and C_{m_w} due to the behaviour of the wings and the slipstream effect on the horizontal tail, with normalized values up to 5.5 and 150 respectively. Some unstable flight configurations are found within the flight envelope at $41°$ and $28°$ due to wing stall.

Nomenclature

α	=	angle of attack $[rad]$
α_c	=	angle of attack of the rotor control plane $[rad]$
$\bar{c}$	=	average wing chord $[m]$
$\bar{q}$	=	dynamic pressure $\frac{1}{2}\rho {V_\infty}^2$ $[\frac{N}{m^2}]$
$\bar{q}_s$	=	slipstream dynamic pressure $\frac{1}{2}\rho {V_s}^2$ $[\frac{N}{m^2}]$
β	=	angle of sideslip $[rad]$
$\boldsymbol{\Omega}$	=	Vector of rotational velocity components $[p, q, r]$ in the body reference frame $[\frac{rad}{s}]$
$\boldsymbol{F}$	=	Vector of force components $[X, Y, Z]$ in the body reference frame $[N]$

*MSc Student, Control and Simulation Section, Faculty of Aerospace Engineering, Delft University of Technology.

$\boldsymbol{I}$ = Matrix of moment inertia in the body reference frame $[kg \cdot m^2]$

$\boldsymbol{M}$ = Vector of force components $[L, M, N]$ in the body axis $[Nm]$

$\boldsymbol{V}$ = Vector of translational velocity components $[u, v, w]$ in the body reference frame $[\frac{m}{s}]$

δ_a = aileron deflection $[rad]$

δ_e = elevator deflection $[deg]$

δ_f = flap deflection $[deg]$

δ_{HS} = Movable horizontal tailplane incidence $[deg]$

δ_r = rudder deflection $[rad]$

ϵ = downwash angle $[rad]$

η = wing tilt angle $[rad]$

γ = flight path angle $[rad]$

λ_c = coefficient of inflow velocity at the control plane $\frac{V_\infty sin\alpha_c}{\Omega R}$

λ_i = coefficient of rotor induced velocity

μ = advance ratio $\frac{V_\infty cos\alpha_c}{\Omega R}$

Ω = rotor angular velocity $[\frac{rad}{s}]$

ϕ = roll angle $[rad]$

ψ = directional angle $[rad]$

θ = fuselage pitch attitude $[rad]$

ζ = slipstream angle $[rad]$

$c_{d_{o_f}}$ = fuselage zero-lift drag coefficient

c_{db} = cylindrical body basic drag coefficient

c_{l_α} = lift coefficient of (propeller) blade element

$c_{l_{W-o}}$ = wing lift coefficient at $\alpha = 0$

C_T = thrust coefficient normalized by $T = C_T \pi \rho (\Omega R)^2 R^2$

M = pitching moment $[Nm]$

p = roll rate $[\frac{rad}{s}]$

q = pitch rate $[\frac{rad}{s}]$

R = rotor radius $[m]$

r = yaw rate $[\frac{rad}{s}]$

S_F = fuselage cross sectional surface area $[m^2]$

S_I = wing planform area inside slipstream $[m^2]$

S_P = rotor surface area $[m^2]$

T = rotor thrust $[N]$

u = velocity component in the body x-axis $[\frac{m}{s}]$

v = velocity component in the body y-axis $[\frac{m}{s}]$

V_∞ = free stream velocity $[\frac{m}{s}]$

V_s = slipstream velocity $[\frac{m}{s}]$

W = aircraft weight $[N]$

w = velocity component in the body z-axis $[\frac{m}{s}]$

X = force in the body x-axis $[N]$

x = distance from the CG along the body x-axis $[m]$

Y = force in the body y-axis $[N]$

y = distance from the CG along the body y-axis $[m]$

Z = force in the body z-axis $[N]$

z = distance from the CG along the body z-axis $[m]$

$\Delta_{cl_{flap,max}}$ = Max increase in lift coefficient by full flap deflection

C_{l_v} = Dihedral stability derivative $C_{l_v} = \frac{\Delta L}{\Delta v} \cdot \frac{V_\infty}{\bar{q}Sl}$

C_{n_v} = Weathercock stability derivative $C_{n_v} = \frac{\Delta N}{\Delta v} \cdot \frac{V_\infty}{\bar{q}Sl}$

C_{m_u} = Speed stability derivative $C_{m_u} = \frac{\Delta M}{\Delta u} \cdot \frac{V_\infty}{\bar{q}S\bar{c}}$

C_{m_w} = Incidence stability derivative $C_{m_w} = \frac{\Delta M}{\Delta w} \cdot \frac{V_\infty}{\bar{q}S\bar{c}}$

ρ = density

Subscripts

AC = aerdynamic center

e = elevator

F = fuselage

HS = horizontal stabilizer

L = left (rotor)

m = main (rotor)

P = propulsive

R = right (rotor)

t = tail (rotor)

W = wing

I. Introduction

Although Totah (1992) was prematurely enthusiastic about the evolution of vertically-abled vehicles, recent developments in urban air mobility and manned vertical take-off and landing (VTOL) have lent credence to the source of his optimism. With recent developments in electric technologies, several companies are racing for certification of a wide variety of imaginative configurations (VFS, 2024). One of the configurations that sparked the imagination of NASA with the GL-10 (Fredericks et al., 2017) and Airbus with the Vahana A^3 (May et al., 2021) is of course the tilt wing. The tilt wing presents advantages both in cruising and hovering flight over other configurations. Chana and Sullivan (1994) compared it favourably to the tilt-rotor, referring to the negative impact of the download induced by the high disk loading of the tilt-rotor. Englar and Kirkpartick (1969) also noted that tilt wing aircraft required low to moderate disk loading to maintain flight at slower transition velocities.

To better understand how this configuration behaves and facilitate the design of future tilt wing solutions, a flight dynamics model is essential. The model proposed in this article is constructed in two research phases. First, a non-linear flight dynamics model of the CL-84 tilt wing aircraft is constructed. To do this, forces on aerodynamic surfaces need to be estimated using methods and information gathered from Englar and Kirkpartick (1969), Gudmundsson (2014), van Holten and Melkert (2002) and more. In the second phase, the model's stability properties are analysed using numerical perturbations.

The main contribution of this paper is the work of Englar and Kirkpartick (1969), with comprehensive wind tunnel data on the airfoil used by the CL-84 and a method for estimating the effect of the rotor slipstream on the wing. Another source worth mentioning is Nieusma's thesis (Nieusma, 1993), which contains most of the geometry of the CL-84 and some flight test data for validation.

This paper is outlined as follows: in section II the proposed methodology is introduced; section III the trimmed procedure is described; section IV more results are discussed; section V the model's strengths and weaknesses are discussed.

II. Six Degree of Freedom Non-Linear Model

In this section, a six degree of freedom flight dynamics model is constructed. The model functions in the body-fixed axis and the north-east-down coordinate system, as defined by Durham (2013). The schematic representation of the CL-84 is shown from three viewpoints to define the direction of all forces, moments, and velocities acting on the aircraft, Figure 1 to Figure 3.

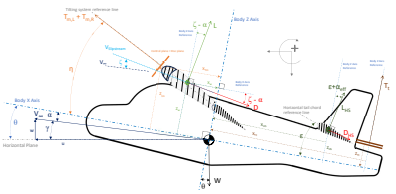

Fig. 1 Forces, moments and velocities acting on the CL-84 in the X - Z plane

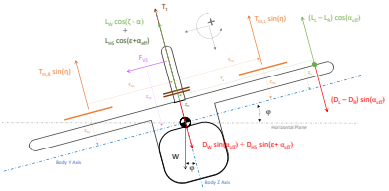

Fig. 2 Forces, moments and velocities acting on the CL-84 in the Y - Z plane

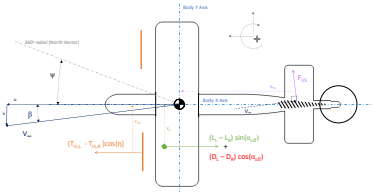

Fig. 3 Forces, moments and velocities acting on the CL-84 in the X - Y plane

Based on this visual, the non-linear six degree of freedom model is built-up using a combination of estimation methods. The model presented in this section rests on several simplifying assumptions:

- **Simple Earth:** Uniform gravitational field on a flat, non-rotating Earth.
- **Simple aircraft:** Rigid body represented by a point mass of constant value with a symmetrical X-Z plane.
- **Simple aerodynamics:** Steady flow, free of wind and turbulence, with a simplified approximation for the rotor slipstream and wing-tail interaction and no interactions between control surfaces. The air is assumed to behave as an ideal fluid.

The effect of tilting the wing on the location of the center of gravity and the resulting moments of inertia, however, could not be ignored. The variations in center of gravity and inertial moments are shown in Figure 4, Figure 5, and Figure 6.

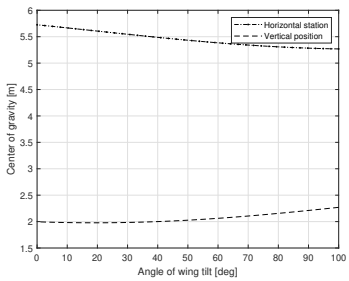

Fig. 4 Center of gravity x and z locations vs. η

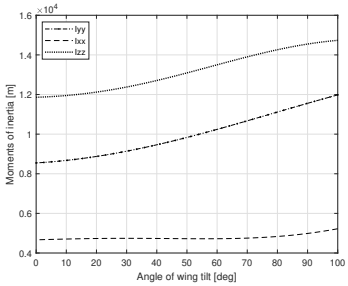

Fig. 5 Moments of inertia I_{yy}, I_{xx}, I_{zz} vs. η

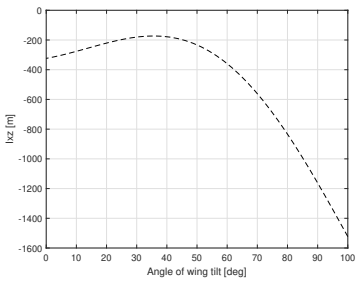

Fig. 6 Coupled moment of inertia I_{xz} vs. η

The maximum variation for each of those parameters is summarized in Table 1 below. Since both the CG locations and the moments of inertia see a shift of 9% or more, these parameters are all considered variable with respect to the wing tilt angle η.

Parameter	CG_x	CG_x	I_{yy}	I_{xx}	I_{zz}	I_{xz}
Max change (%)	9	15	29	19	11	89

Table 1 Percentage difference between maximum and minimum CG locations and moment of inertial values

1. Rotors

The rotor dynamics are examined using helicopter theory from van Holten and Melkert (2002) and Padfield (2007). Some additional assumptions specific to the rotor dynamics are listed below:

- **Uniform Inflow Assumption:** The flow velocity is assumed to the be uniform and linear across the rotor disk.
- **Aerodynamics:** The aerodynamic forces are assumed to be quasi-steady, responding instantaneously to changes in blade motion and flow conditions, and two-dimensional, with each blade treated as an airfoil section with lift and drag characteristics based on two-dimensional airfoil theory.
- **Actuator Disk Theory:** The rotor is modeled as an infinitely thin disk that imparts a uniform velocity increase to the flow passing through it.
- **Induced Velocity:** The rotor wake from the main propellers is assumed to be sufficiently far from the wing to be fully formed and uniform. The wake from the tail rotor is neglected.
- **Propeller Drag:** Rotor drag is not considered separately from the aircraft drag. The tail rotor drag is assumed to be contained within the empennage drag and the main rotor drag within the wing drag.
- **Rotor properties:** c_{l_α}, the average coefficient of lift of the propeller blades, describes the average lift produced along the entire blade, up to the hub. It is assumed to be 0.1 $\frac{1}{rad}$. The propellers are assumed to always rotate such that the blade tip velocity is 98% of local mach speed.
- **No Propeller Flapping:** Hindson et al. (1993) clarify that the CL-84 has "the absence of any propeller flapping or degree of freedom"(p394).

Since the CL-84 was not equipped with a swashplate for lateral cyclic and the flapping motion of its rotors was negligible, the purpose of considering the rotor dynamics is to translate thrust values into pilot command inputs. To this end, the thrust coefficient calculations from van Holten and Melkert (2002) are adapted as Equation 1 for the blade element momentum theory and Equation 2 for the Glauert equation. Given a value of thrust required for trimmed flight at a given flight condition, Equation 2 can be used to determine the induced flow velocity λ_i and Equation 1 can subsequently be solved for the collective blade pitch angle, θ_o.

$$C_{T_{BEM}} = \frac{1}{n_b} c_{l_\alpha} \left[\frac{2}{3} \theta_0 \left(1 + \frac{3\mu^2}{2} \right) - (\lambda_c + \lambda_i) \right] \tag{1}$$

$$C_{T_{Glau}} = \lambda_i \sqrt{\left(\frac{V}{\Omega R} cos(\alpha_c) \right)^2 + \left(\frac{V}{\Omega R} sin(\alpha_c) + \lambda_i \right)^2} \tag{2}$$

2. Aerodynamic estimations

Aerodynamic forces are estimated based on coefficients. Englar and Kirkpartick (1969) provided methods for estimating aerodynamics forces on a tilt wing aircraft, including a method for approximating the effect of rotor slipstream on the wing. They modeled the fuselage-empennage lift and drag using a flat plat approximation, much like Pavel

(1996). The relation used is shown in Equation 3.

$$
\begin{aligned}
C_{L_F} &= C_{d_b} sin^2(\alpha_s) cos(\alpha_s) \\
C_{D_F} &= C_{d_b} sin^3(\alpha_s) + C_{d_{of}} \qquad (3) \\
L_F &= q_s S_N C_{L_F} \\
D_F &= q S_F C_{D_F} + q F_f \qquad (4)
\end{aligned}
$$

The wing's lift and drag estimations are based on wind tunnel tests on NACA$63_3$418 with high lift devices in the same configuration as the CL-84. This data, obtained from Englar and Kirkpartick (1969), is approximated in this model by a polynomial fit for both drag and list for the airfoil equipped with Krüger leading edge devices. The fitted data is shown in Figure 7.

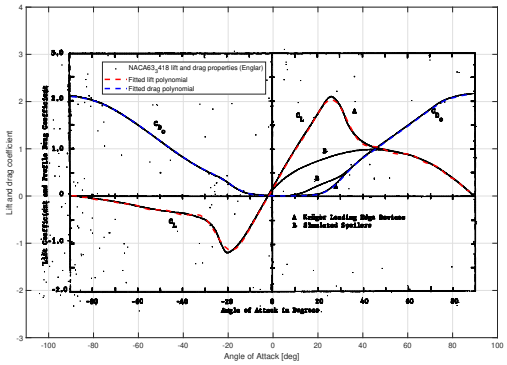

Fig. 7 Lift and profile drag coefficient at angles of attack [-90 90] degrees (Englar and Kirkpartick, 1969)

Englar and Kirkpartick (1969) also formulated a method to approximate the effect of the rotor slipstream over the wings using pressure vectors. Using the dynamic pressure of the free stream and the pressure caused by the thrust over the disk area, trigonometry is used to deduce the slipstream dynamic pressure. Figure 8 shows how this effect can be used to estimate the angle of slipstream, the modified angle of attack, and the dynamic pressure. The equations are:

$$\zeta = \arctan \frac{T_m sin(\eta_{est} + \alpha)}{S_p \bar{q} + T_m * cos(\eta_{est} + \alpha)} \qquad (5)$$

$$\alpha_s = \eta + \alpha - \zeta \qquad (6)$$

$$\bar{q}_s = \sqrt{(\bar{q} + \frac{T_m}{S_p} cos(\eta + \alpha))^2 + \frac{T_m}{S_p} sin(\eta + \alpha)^2} \qquad (7)$$

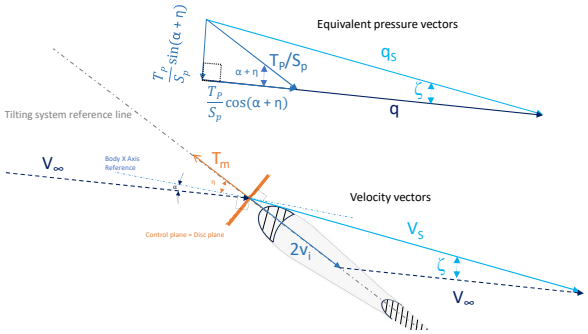

Fig. 8 Rotor slipstream effect on angle of attack

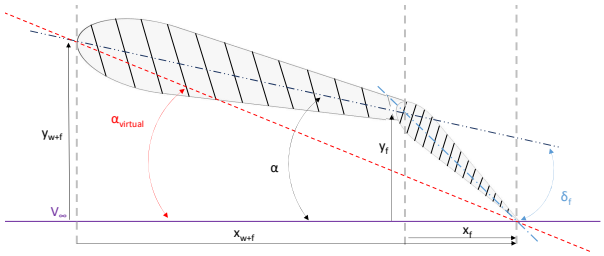

Fig. 9 Effective angle of attack due to flap deflection

Scholz (2017) describes the method developed by the DATCOM manual to estimate the lift and drag contributions of high lift devices such as flaps. The flap deflection leads to an increase in effective angle of attack on the wing, as described by Figure 9. The increase in angle of attack is accompanied by an increase in the lift coefficient of the wing. Equation 8 is used to estimate this increase based on the flap type, size, and deflection.

$$\Delta_{c_{l_{flap}}} = k_{1_f} k_{2_f} k_{3_f} \Delta_{c_{l_{flap,max}}} \tag{8}$$

$$\Delta_{c_{l_{flap,max}}} = 1.72 \tag{9}$$

$$k_1 = 0.81 \tag{10}$$

$$k_2 = 0.2 + \delta_f \cdot 0.024 \tag{11}$$

$$k_3 = \frac{\delta_f}{45} \cdot 1.188 \tag{12}$$

Considering these estimations, the lift and drag on the wings are calculated according to Equation 13. The right and left half wing are estimated separately to account for differential thrust and aileron deflection. The wing's moment is estimated based on the distance between the wing's center of gravity and its aerodynamic center, both of which naturally change with tilt angle.

$$\begin{aligned} L_W &= q_s S_I (C_{L_w} + \Delta_{c_{l_{flap}}}) \\ D_W &= q_s S_I C_{D_w} \end{aligned} \tag{13}$$

The CL-84 flew with the flaps and horizontal stabilizer scheduled to deflect along with the wing tilt, as described by Nieusma (1993). The schedule used for the flaps is shown in Figure 10 for the flaps and Figure 11 for the horizontal stabilizer.

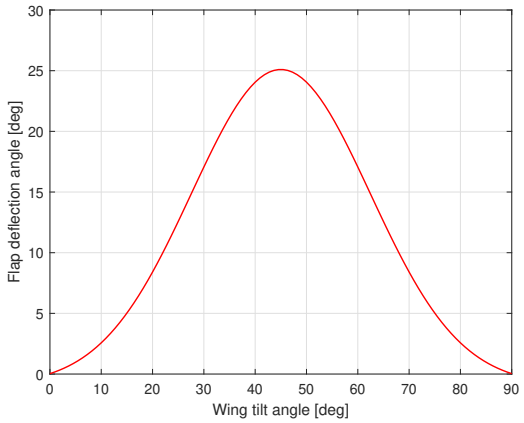

Fig. 10 Flap schedule used in this report

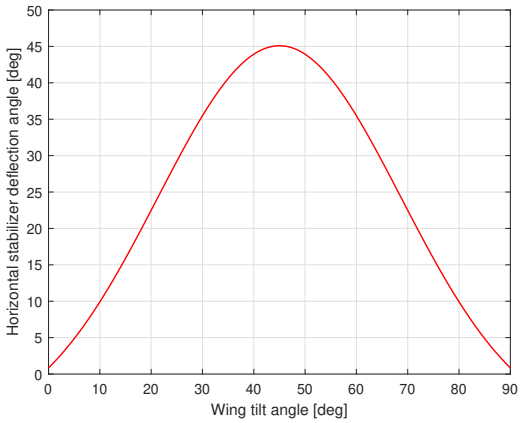

Fig. 11 Horizontal tail schedule used in this report

The mass of air encountered by the horizontal tail is deflected by its passage over the wing, an effect that is estimated according to conceptual design techniques from Gudmundsson (2014). To account for this effect, an epsilon factor is calculated according to Equation 14, with the effective angle of attack on the horizontal stabilizer expressed by Equation 15.

$$\varepsilon = \frac{2 * (c_{l_{W-o}} + c_{l_W})}{\pi AR} \tag{14}$$

$$\alpha_{HS} = \alpha + \delta_{HS} - \zeta - \varepsilon \tag{15}$$

Without a confirmed airfoil for the horizontal and vertical empennage of the CL-84, it is assumed that the symmetrical NACA0012 is a close enough approximation. The lift, drag, and moment coefficient were estimated based on the work of Critzos et al. (1955) to account for a wide range of angles of attack. To spare a thought for the complexity of the trim solver, these coefficients were not espoused with large order polynomials, but estimated with sinusoids. The curve approximations are shown in Figure 12, Figure 13, and Figure 14. The drag coefficient and the lift stall characteristics are approximated by normal distribution functions.

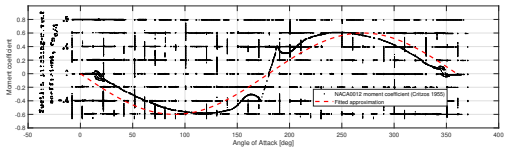

Fig. 12 Approximation of NACA0012 $C_m(\alpha)$ from Critzos et al. (1955)

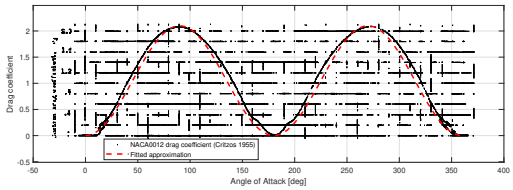

Fig. 13 Approximation of NACA0012 $C_D(\alpha)$ from Critzos et al. (1955)

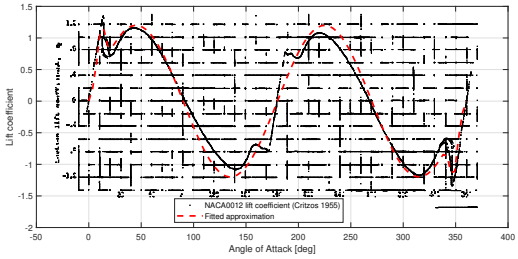

Fig. 14 Approximation of NACA0012 $C_L(\alpha)$ from Critzos et al. (1955)

The equations used to approximate the curves shown in Figure 12, Figure 13, and Figure 14 are provided by Equation 16 below.

$$
\begin{aligned}
C_{M_{NACA0012}} &= \pm\left(-0.3e^{-0.014(\alpha_{eff}-90)^2} - 0.8e^{-0.015(\alpha_{eff}-120)^2} + 0.5e^{-0.011(\alpha_{eff}-120)^2} + 0.29e^{-0.05(\alpha_{eff}-170)^2}\right) \\
C_{D_{NACA0012}} &= \pm\left(1.25e^{-0.014(\alpha_{eff}-90)^2} + 1.75e^{-0.026(\alpha_{eff}-90)^2} - e^{-0.013(\alpha_{eff}-90)^2}\right) \\
C_{L_{NACA0012}} &= 1.2sin(2\alpha_{eff}) \pm \left(0.7e^{\frac{-(\alpha_{eff}-12)^2}{40\cdot 0.8^2}}\right)
\end{aligned} \tag{16}
$$

3. Equations of motion

The equations of motion are broadly described by Equation 17

$$
m\frac{d}{dt}(\boldsymbol{V}) + \boldsymbol{\Omega} \times m\boldsymbol{V} = \boldsymbol{\Sigma F} \tag{17}
$$

$$
\boldsymbol{I}\frac{d}{dt}(\boldsymbol{\Omega}) + \boldsymbol{\Omega} \times \boldsymbol{I\Omega} = \Sigma \boldsymbol{M}
$$

When the general form is applied to the CL-84, and after grouping propulsive and aerodynamic forces separately, Equation 18 thru to Equation 24 are obtained.

$$m\dot{u} = X_P + X_A - Wsin(\theta) - qw + rv \tag{18}$$

$$m\dot{v} = Y_A + Wcos(\theta)sin(\phi) + pw - ru \tag{19}$$

$$m\dot{w} = Z_P + Z_A + Wcos(\theta) + qu - pv \tag{20}$$

$$I_D = I_{xx}I_{zz} - I_{xz}^2 \tag{21}$$

$$\dot{p} = \frac{I_{zz}}{I_D}\left[L_{P,A} + I_{xz}pq - qr(I_{zz} - I_{yy})\right] + \frac{I_{xz}}{I_D}\left[N_{P,A} - I_{xz}qr - pq(I_{yy} - I_{xx})\right] \tag{22}$$

$$\dot{q} = \frac{1}{I_{yy}}\left[M_{P,A} - pr(I_{xx} - I_{zz}) - I_{xz}(p^2 - r^2)\right] \tag{23}$$

$$\dot{r} = \frac{I_{xz}}{I_D}\left[L_{P,A} + I_{xz}pq - qr(I_{zz} - I_{yy})\right] + \frac{I_{xx}}{I_D}\left[N_{P,A} - I_{xz}qr - pq(I_{yy} - I_{xx})\right] \tag{24}$$

$$\dot{phi} = p + (q \cdot sin\phi + r \cdot cos\phi)tan\theta \tag{25}$$

$$\dot{\theta} = q \cdot cos\phi - r \cdot sin\phi \tag{26}$$

$$\dot{\psi} = (q \cdot sin\phi + r \cdot cos\phi)sec\theta \tag{27}$$

III. Trim

In trimmed flight, all linear and rotational accelerations are set to zero. From the equations of motion it is clear that the aircraft is over-actuated: even after assuming an altitude and scheduling the flaps and horizontal stabilizer movement, there are 12 possible control settings [η, u, v, w, $T_{m,L}$, $T_{m,R}$, T_t, δ_e, δ_a, δ_r, θ, ϕ] for only 6 distinct equations. Therefore, some of those free parameters need to be fixed. In view of obtaining a transition corridor, η is prescribed. Also, models are typically trimmed for a range of airspeeds. In this case, a vector of [η u] determines the flight condition, with several parameters [v, w, ϕ] set to zero, resulting in all rotational rates being zero as well. For the rest, it is considered that the elevator has little control effectiveness around hover, so for wing tilt angles between 100° and 20°, the fuselage pitch angle is one of the solved variables. Subsequently, the fuselage pitch attitude is set to zero and the elevator deflection replaces as the solved variable. For wing tilt angles greater than 20°, the elevator deflection is used to offset the highly variable angle of attack on the horizontal tail, with a value of $-\alpha_{HS}$. MATLAB's built-in function vpasolve is used to find a solution to the set of equations. The so-called trim corridor, or the flight envelope during the wing tilt transition, is shown in Figure 15.

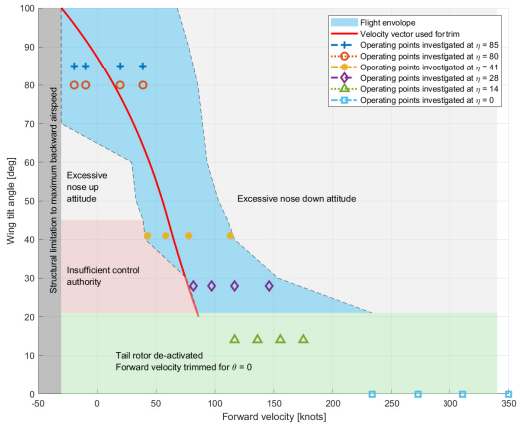

Fig. 15 Transition corridor for the CL-84 model

Several operating points are selected to investigate the behaviour of the tilt wing inside the corridor. The pilot input control, beginning with the elevator deflection, are investigated. The fuselage pitch attitude θ, which was not kept to 0 as a result of the trim logic, is displayed in Figure 16 next to the elevator deflection angle δ_e on Figure 17.

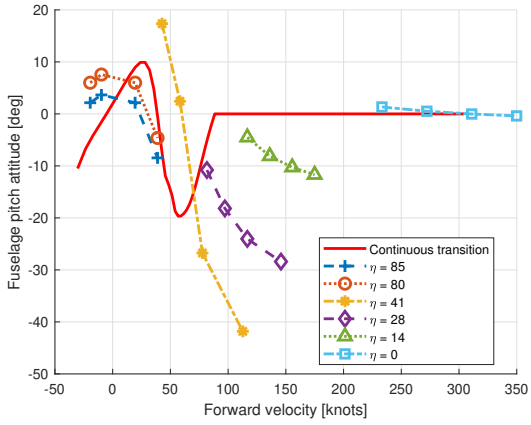

Fig. 16 Fuselage pitch attitude when $\delta_e = -1\alpha_{HS}$

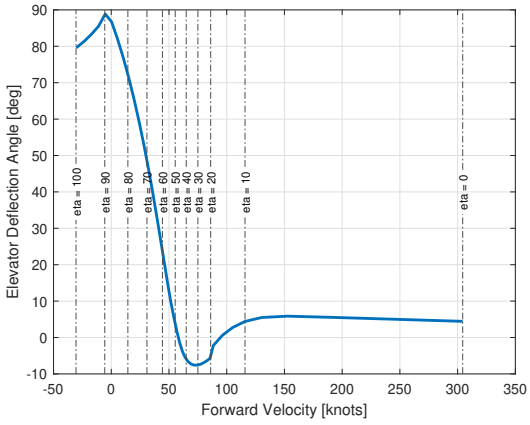

Fig. 17 Elevator deflection δ_e set to $-1\alpha_{HS}$

From these two figures, it can be seen that the slipstream angle in and around hover dominates the angle of attack on the horizontal tail. The angle of the sideslip ζ tends to the wing tilt angle as forward speed u goes to 0. Then it is easy to see how the slipstream angle dominates the aerodynamics on the tail at low speeds and high angles of wing tilt. At 90°, the elevator deflection angle is also 90°. Up to 60°, the difference between the wing tilt angle η and δ_e doubles every decade. Meanwhile, as indicated by the transition corridor in Figure 15, the continuous mission used for verification of continuity in the model skirts the slower limit of the flight envelope that can be achieved with this elevator schedule. Since Figure 16 confirms that the fuselage pitch attitude decreases to achieve trim at faster airspeeds,

the conclusion is that the elevator deflection is insufficient to allow flight at higher pitch attitudes.

The thrust required for trim at the operating points of interest from all rotors combined (two main and one tail) is shown in Figure 18. It is found that the thrust required for trimmed flight does not vary much with the angle of wing tilt η, but much more so with airspeed u.

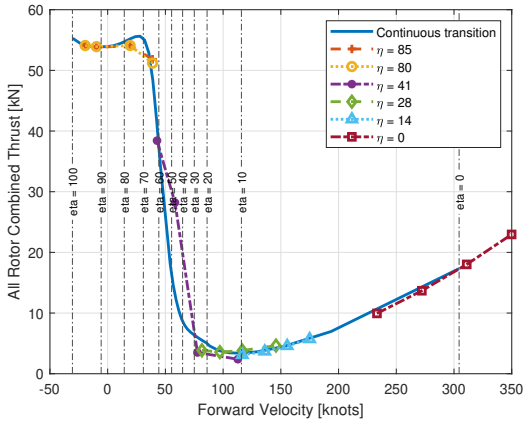

Fig. 18 Thrust at trim for all rotors combined

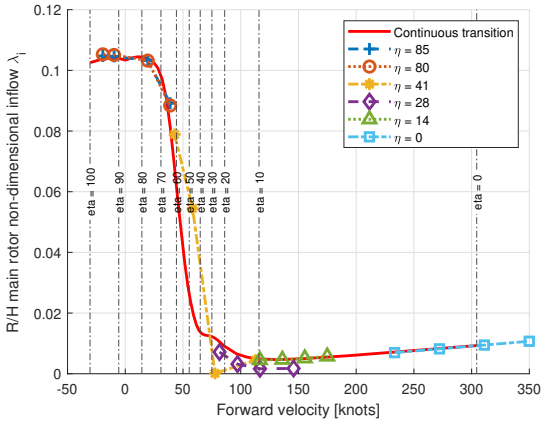

Fig. 19 R/H main rotor induced velocity λ_i

The induced velocity is shown in Figure 19 next to the thrust curve. Without the effects of flapping, the induced velocity is found to be directly proportional to $\frac{T}{u}$. This can also be shown by looking at Equation 2 with the consideration that large values of η result in low values of α_c and vise versa. Therefore, at low values of u, which are accompanied by large η angles, μ approaches 0. Conversely, at low angles of η, λ_c tends to 0. In each case, the induced velocity λ_i reduces to some proportion of $\frac{T}{u}$.

The propeller blade collective pitch angle is shown in Figure 20 for the right hand main rotor. This time, looking at Equation 1 provides insight into the tendency of the collective pitch angle without flapping motion. For large angles of wing tilt, accompanied by low airspeed, θ_o is found to follow $\frac{T\lambda_i}{1+\mu^2}$, whereas at sufficiently low values of η, θ_o is directly proportional to u.

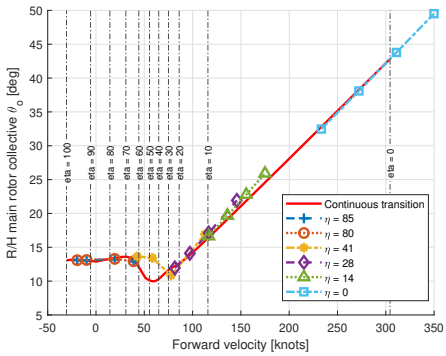

Fig. 20 R/H main rotor collective propeller pitch θ_o

IV. Results

The output of the model is analysed in this section. First, the model is further validated against flight test data in subsection IV.A. Then the stability of the model is examined in subsection IV.B.

A. Validation

The model is further validated against flight test data from Nieusma (1993), as well as the model used in his report. The available data describes the trim control inputs for flight at specified conditions. As much as possible, the flight conditions were reproduced, though there are a number of unknown factors. The most difficult unknown is the size of the elevator used in Nieusma (1993)'s model and on the CL-84. Regardless, the comparisons are presented in Figure 21 to Figure 24. In each case, the flight data provided is the fuselage pitch angle for trimmed flight at a specified angle of wing tilt and airspeed. The variations in elevator deflection is also provided, though in the reproduction it is kept constant. Environmental parameters, the angle of flap, and tailplane deflection are also provided and imitated in the validation runs.

As Nieusma (1993) also discovered, the hover configuration and flight regime is very difficult to predict correctly. Even the flight test data show that the fuselage pitch attitude varied. The most likely culprit for inaccuracy in this flight region is the simplifying assumptions around the rotor slipstream effect on the wings and empennage. The inaccuracy involved in the slipstream estimates are compounded at low velocities where the angle of attack on all aerodynamic surfaces depend most heavily on it. The out-sized impact of the rotor slipstream can also be observed in the other flight conditions, with a steepening of the pitch attitude slope at lower speeds. At $\eta = 28.6°$, this effect is also very prominent because the model's estimate of the pitch attitude is high and the velocity region selected is at the slow end of the flight envelope.

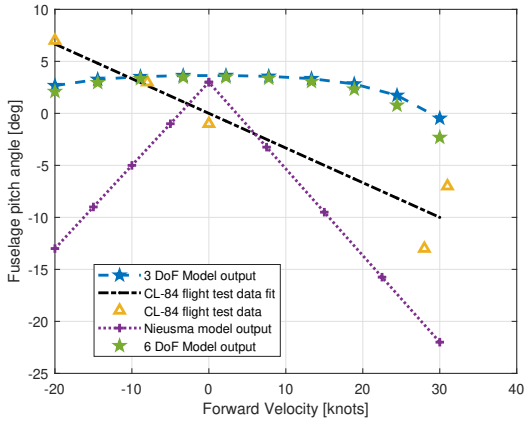

Fig. 21 Comparison to flight test data at 85.1°wing tilt (Nieusma, 1993)

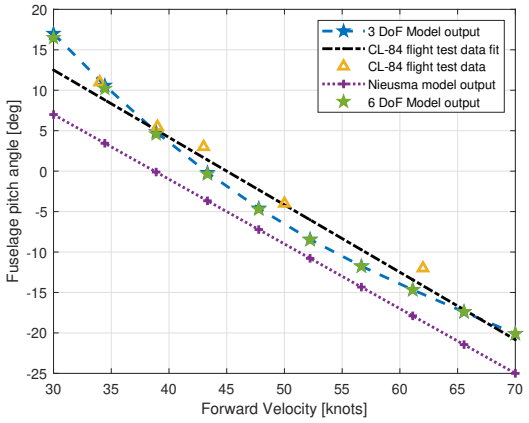

Fig. 22 Comparison to flight test data at 41.5°wing tilt (Nieusma, 1993)

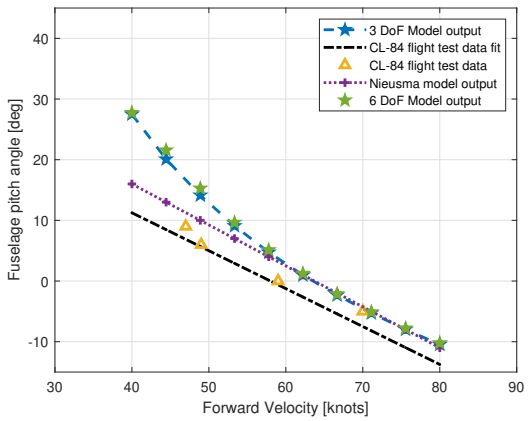

Fig. 23 Comparison to flight test data at 28.6°wing tilt (Nieusma, 1993)

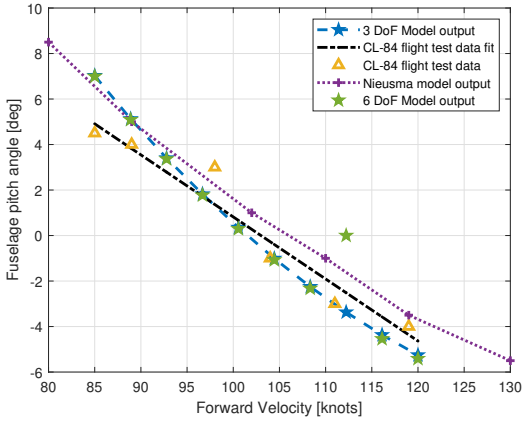

Fig. 24 Comparison to flight test data at 14°wing tilt (Nieusma, 1993)

B. Stability

The stability of the model is investigated in this section by means of numerical perturbations about the trim point. For lateral direction stability, the dihedral stability derivative C_{l_v} and the weathercock derivative C_{n_v} are selected. They are non-dimensionalized by $C_{l_v} = \frac{\frac{\Delta L}{\Delta v} \cdot V_\infty}{\bar{q} \cdot S \cdot b}$ and $C_{n_v} = \frac{\frac{\Delta N}{\Delta v} \cdot V_\infty}{\bar{q} \cdot S \cdot b}$. Those two derivatives are strong indicators of the stability of an aircraft with respect to lateral disturbances (G.Steinbusch, 2021). The dihedral stability derivative C_{l_v}, shown in Figure 25, is the derivative of the rolling moment L with respect to the lateral velocity v. The weathercock derivative C_{n_v} is the derivative of the yawing moment N with respect to the lateral velocity v. For positive stability, the aircraft should manoeuvre to restore the initial trim parameters when disturbed. To examine how the aircraft responds to disturbances from a trim point, a small variation in v is induced and the change in rolling and yawing moment is monitored.

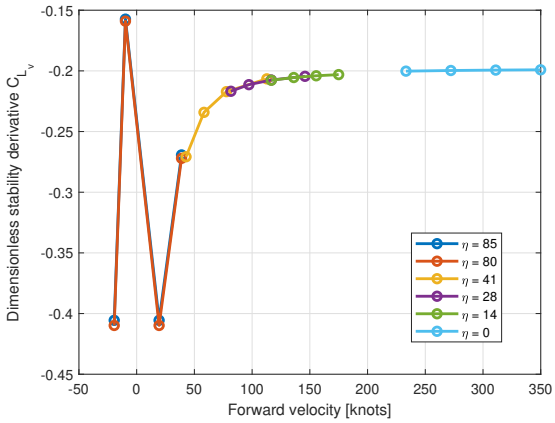

Fig. 25 Dihedral derivative C_{l_v}

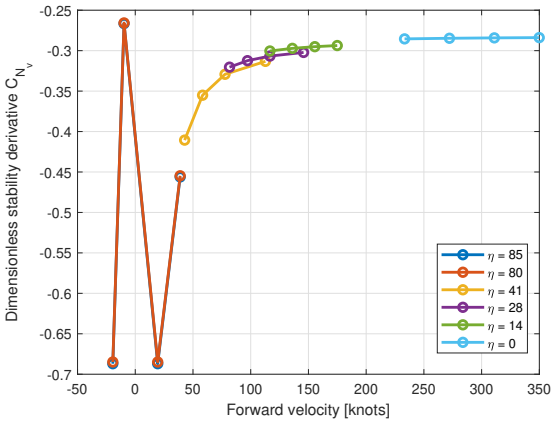

Fig. 26 Weathercock derivative C_{n_v}

For the derivative C_{l_v}, recall that v is defined positive to the right and the roll L is defined positive when the right

wing lowers. However, to recover trim from a positive increment in v, a turn to the left is necessary. This can be achieved by initiating a rolling motion with the right wing raised, meaning that the derivative should have a negative value for positive stability. Indeed, Figure 25 shows that for all flight conditions investigated, the dihedral derivative is negative. Similarly, because a positive yaw N is defined positive with the nose turning to its right, a negative yawing moment is desirable for positive stability. So the weathercock derivative C_{n_v} should also be negative, as shown in Figure 26. Both derivatives show a significant increase in their value around but not at hover. This can be explained by looking at the sidelip angle β. At hover, a change in lateral velocity v induces a β value of 90°, which does not stimulate the vertical tail very effectively. As the aircraft exits hover, β can become very large until the forward speed u reduces the relative important of v on β.

The longitudinal incidence stability derivative C_{m_w} and speed stability derivative C_{m_u} are also examined.

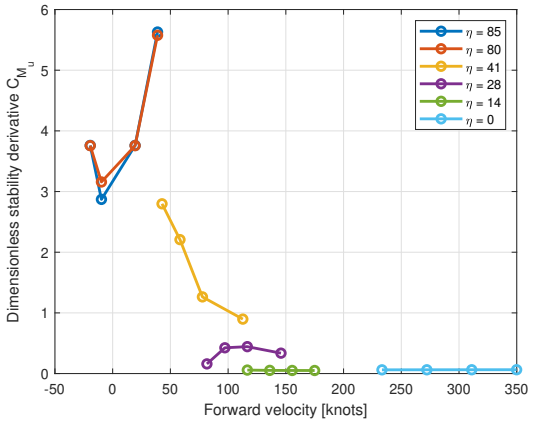

Fig. 27 Speed stability derivative C_{m_u}

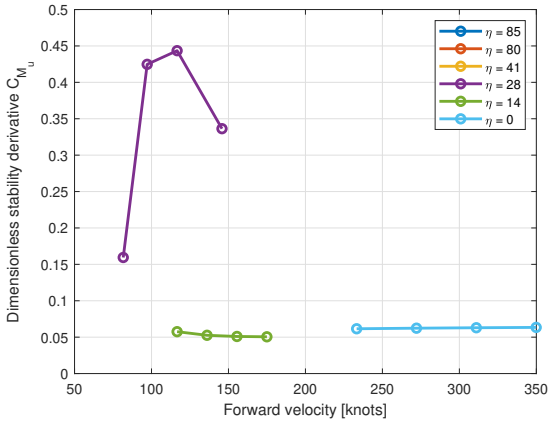

Fig. 28 Close-up of Figure 27

They are non-dimensionalized by $C_{m_u} = \frac{\frac{\Delta M}{\Delta u} \cdot V_\infty}{\bar{q} \cdot S \cdot \bar{c}}$ and $C_{m_w} = \frac{\frac{\Delta M}{\Delta w} \cdot V_\infty}{\bar{q} \cdot S \cdot \bar{c}}$.Figure 27 and Figure 28 present the model's speed stability derivative C_{m_u}. This derivative describes how the pitching moment M reacts to a change in forward velocity u.

The pitching moment M, is defined as positive when the nose lifts and the forward speed u when the aircraft gains velocity toward the nose. So the stable reaction to an increase in airspeed is for the aircraft to pitch up to redirect the kinetic energy. The derivative C_{m_u} is therefore stable for all operating points investigated. Around hover it is much greater than other aircraft such as helicopters (Pavel, 1996) or tilt-rotors (G.Steinbusch, 2021). This can be explained by the orientation of the wings, which are vertical in hover, causing a lot of resistance to increases in forward speed.

The incidence stability derivative, which expresses how M changes with changes in heave velocity w, is shown in Figure 29 and Figure 30. It exhibits some remarkable characteristics with very large values in and around hover, and unstable values at some flight configurations. For positive stability, with the heave w defined positive downward, the derivative should be positive such that the aircraft pitches up in response to an increase in downward velocity. The flight

conditions that yield a negative C_{m_w} are explored in more detail.

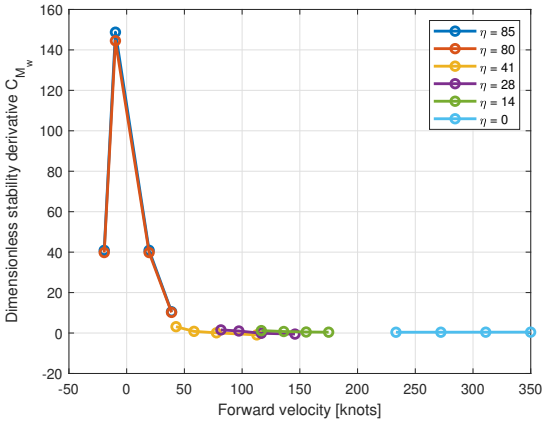

Fig. 29 Incidence stability derivative C_{m_w}

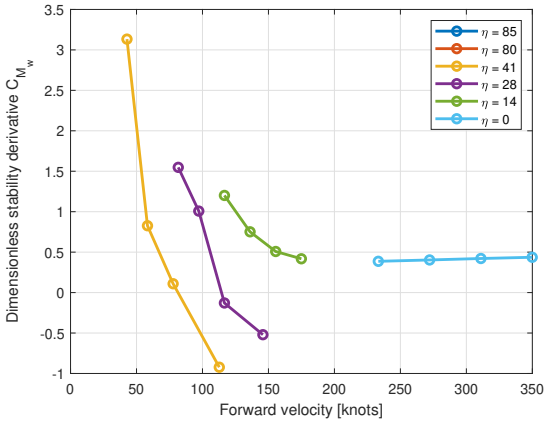

Fig. 30 Close-up of Figure 29

The large value for C_{m_w} around hover can be explained by the horizontal tail, which is responsible for 74% to 93% of the derivative value depending on the airspeed. Due to low forward speed, the angle of attack on the tail originates from the rotor slipstream. When the slipstream is close to $-90°$ and there is no forward speed to soften the angle of attack on the tail, this angle of attack generates no lift and the drag force is downward at the tail. However, when the angle of attack is lowered, such as by increasing w, the tail produces a downward lift force, causing a positive moment.

The unstable flight conditions are investigated by a breakdown of contributing factors. The change in pitching moment generated by each aerodynamic surface when w is perturbed is shown in Figure 32 and Figure 31. In both cases, the change in pitching moment produced by the wing is the cause for the negative stability coefficient, and unstable behaviour. For those flight conditions, the moment produced by the wing decreases when w is increased. The likely explanation is that the wing is experiencing a post stall angle of attack at trim, such that the lift coefficient slope is negative. In that case, an increase in angle of attack, such as brought about by an increase in w, decreases the lifting force on the wing and vice versa. It is important to note that these stability derivatives depend on the elevator deflection, which is set crudely. The initial operating point is trimmed for a specified elevator setting, which is not changed when the perturbation is applied.

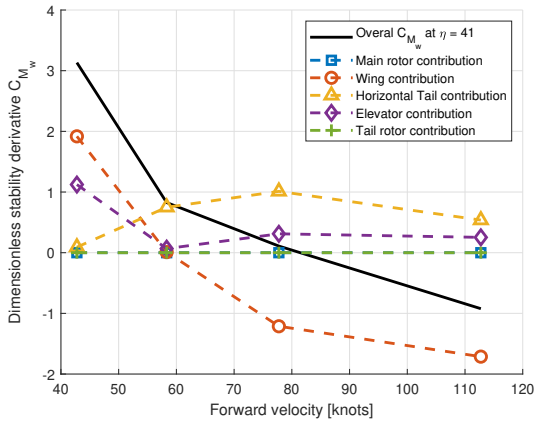

Fig. 31 Breakdown of components of C_{m_w} at $\eta = 41°$

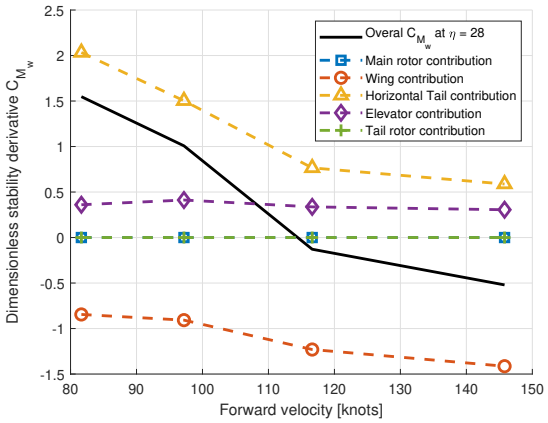

Fig. 32 Breakdown of components of C_{m_w} at $\eta = 28°$

V. Conclusion

A six-degree of freedom model has been presented with some validation and a discussion of the behaviour and stability characteristics of the tilt-wing configuration, as implemented on the Canadair CL-84 Dyanvert. The trimmed flight envelope sheds light on the relationship between the wing tilt angle, the airspeed, and the pilot controls. Namely, the airspeed plays an important role in determining the propeller collective blade angle setting and the induced velocity. The fuselage pitch attitude plays an important role in the trim of the aircraft, with much more sensitivity toward the middle of the transition. Still, the model compared relatively well to flight test data, showing a good degree of fidelity at relatively high airspeeds. Near hover, the simple rotor slipstream assumptions fall apart to som extent. The model established stability in most critical areas, with some unstable longitudinal stability characteristics related to vertical gusts at specific flight configurations.

This research could be extended by widening the flight envelope explored using various elevator settings. The use of an optimization algorithm could solve for δ_e along with the other pilot input variables. Such a trim method would also allow a continuous trim mission at $\theta = 0$ to reduce the impact of the fuselage pitch attitude on the other findings. Finally, the rotor slipstream model could be fine-tuned to improve the model's performance at and around hover.

References

Totah, J. J., "A mathematical model of a tilt-wing aircraft for piloted simulation," *NASA technical memorandum 103864*, 1992.

VFS, T. V. F. S., "V/STOL Aircraft and Propulsion Concepts," , 2024. URL `https://vtol.org/vstol/wheel.htm`.

Fredericks, W., et al., "Greased Lightning (GL-10) Flight Testing Campaign," *NASA/TM-2017-219643*, 2017.

May, M., Milz, D., and Looye, G., "Dynamic Modeling and Analysis of Tilt-Wing Electric Vertical Take-Off and Landing Vehicles," *AIAA 2022-0263. AIAA SCITECH 2022 Forum*, 2021.

Chana, W. F., and Sullivan, T. M., "The Tilt Wing Configuration For High Speed VSTOL Aircraft," *ICAS 1994 Anaheim*, Vol. 1, 1994, pp. 871–889.

Englar, R. J., and Kirkpartick, D. G., "Parametric Trade-off Analysis for Tilting Free Propulsor V/STOL Aircraft in Equilibrium Transition," *Naval Ship Research and Development Center*, 1969.

Gudmundsson, S., *Generatl Aviation Aircraft Design*, 1st ed., Elsevier Inc., Oxford, UK, 2014. ISBN: 978-0-12-809998-8.

van Holten, T., and Melkert, J. A., *Helicopter Performance, Stability and Control*, TU Delft, 2002.

Nieusma, W., "An investigation of twopropeller tilt wing VSTOL aircraft flight characteristics," *Naval Postgraduate School*, 1993.

Durham, W., *Aircraft Flight Dynamics and Control*, 1st ed., John Wiley & Sons, Ltd, West Sussex, UK, 2013. ISBN: 978-1-118-64681-6.

Padfield, G., *Helicopter FLight Dynamics*, 2nd ed., Blackwell Publishing, Oxford, UK, 2007. ISBN: 978-14051-1817-0.

Hindson, W. S., et al., "Piloting Considerations for Terminal Area Operations of Civil Tiltwing and Tiltrotor Aircraft," *Piloting Vertical Flight Aircraft: A Conference on Flying Qualities and Human Factors*, 1993.

Pavel, M. D., ""Six Degree-of-Freedom Linear Model for Helicopter Trim and Stability Calculation", Memorandum M-756," , 1996.

Scholz, D., "High Lift Systems and Maximum Lift Coefficients," *Lecture Notes*, 2017. URL `https://www.fzt.haw-hamburg.de/pers/Scholz/HOOU/AircraftDesign_8_HighLift.pdf`, last updated 13/06/2023.

Critzos, C. C., et al., "Aerodynamic Characterictics of NACA0012 Airfoil Section at Angles of Attack From 0 degrees to 180 degrees," *National Advisory Committee for Aeronautics, Technical Note 3361*, 1955.

G.Steinbusch, "A Theoretical Approach for Analysing the Stability Characteristics of Tiltrotor Aircraft," *Delft Institute of Technologies, MSc Thesis*, 2021.

Part III

Three Degree of Freedom Model

4

Development of a Longitudinal Model

Applying the method outlined in Part I, Section 3.1, this chapter presents the endeavour to establish a longitudinal flight dynamics model of a tilt-wing aircraft using the CL-84's geometry and properties described in Appendix B. This chapter begins with a schematic representation of the CL-84 in Section 4.1 to define the framework of the model. Then, methods for estimating the external forces and moments acting on the aircraft are suggested in Section 4.2. Finally, the equations of motion are presented and solved for trimmed flight in Section 4.3. The output of the model is compared to the expected results and evaluated for validity in Chapter 5. The impact of tilting the wings on the aircraft's center of gravity is explained in Appendix C.

4.1. Schematic Representation

This section lays the foundational framework for developing the longitudinal flight dynamics model. Using the schematic representation Figure 4.1, the direction of each external force as well as the definition for the aerodynamics angles are determined. As an extension of these definitions, the assumptions underlying the model developed in this chapter are also discussed.

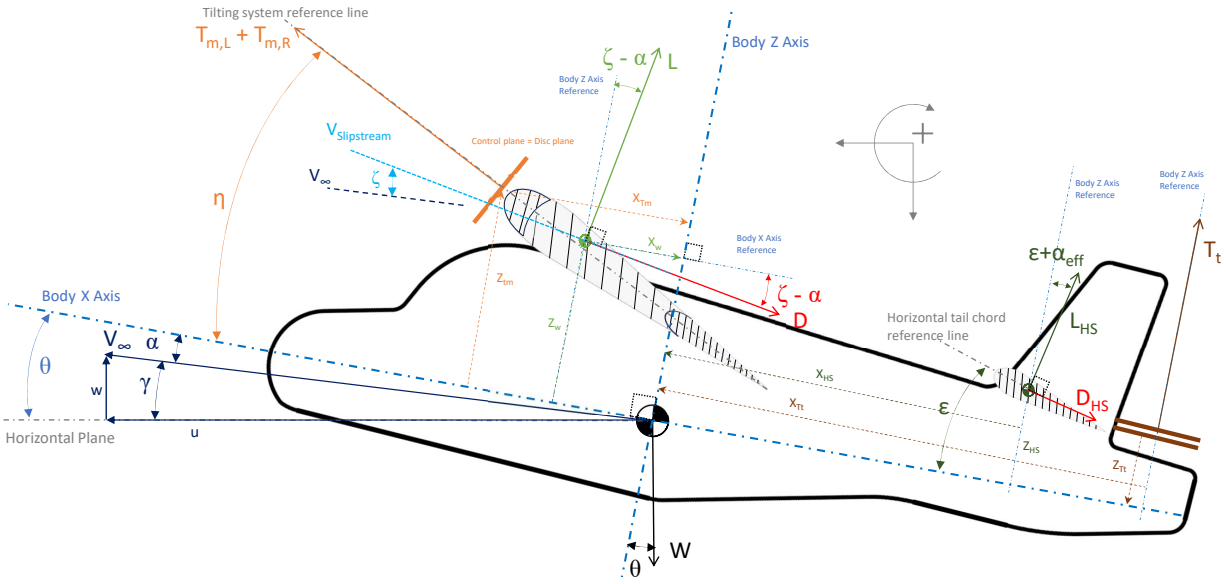

Figure 4.1: Forces, moments and velocities acting on the CL-84 in the XZ-plane

From Figure 4.1 it is clear that the body-fixed x-axis is defined, as per convention, as passing through the center of gravity and the nose of the aircraft. More details on coordinate systems are available in Appendix D. Following this convention, the y-axis is defined perpendicular to the x-z plane of symmetry toward the right wingtip, and the z-axis accordingly extends from the center of gravity downward. Using the right-hand rule, this implies that a positive rotation about the y-axis, defined as rotational vector q,

encourages a nose up attitude. The vectors corresponding to external forces, $T_{m(L,R)}$, $L_{W,HS}$, $D_{W,HS}$, T_t, and W are defined positive in accordance with to the orientation shown. The moment arms to each vector are also shown.

Further, the relevant angles are shown and defined as well. To stay consistent with the pitching rotation q definition, the fuselage pitch attitude is also defined as positive when the nose pitches away from to the ground. The angle of attack is defined positive so as to cause by default positive forces on the aerodynamic surfaces, so that the relative flow of the air mass impact the aerodynamic surfaces from below. Both of those conventions are normal for fixed-wing (Durham, 2013), but they are reverse for helicopters (van Holten and Melkert, 2002). The fixed-wing convention is chosen in this report because the rotors are much simpler than helicopter rotors, and the aerodynamic surfaces are more prominent. The thrust from the wing-mounted rotors also influences the angle of attack. This effect is represented by an angle ζ. As a result, the effective angle of flow on the wing is considered to be $(\zeta - \alpha)$ and the aerodynamic forces are parallel (for drag) or perpendicular (for lift) to that resultant angle. The tilting angles of both the wing, η and the horizontal stabilizer, ε, are considered positive when they increase the effective angle of attack.

The assumptions underlying the model are as follows. The assumption specifically related to the thrust systems are discussed in Section 4.2.1.

- **Uniform Gravity Field:** The gravitational field is assumed to be uniform and constant in direction and magnitude.
- **Flat Earth Assumption:** The Earth is considered flat and non-rotating.
- **Rigid Body Assumption:** The aircraft is considered a rigid body, meaning that its shape and structure do not deform under the forces acting on it.
- **Point Mass Representation:** The aircraft is modeled as a point mass located at its center of gravity, with forces and moments applied at this point.
- **Constant Mass:** The mass of the aircraft is assumed to be constant, neglecting fuel consumption and payload changes during the flight.
- **Neglected Dynamics:** Only three degrees of freedom are considered. This includes pitch, and translational motion along two axes, X and Z, only.
- **Symmetric Flight:** The model assumes symmetric flight conditions, meaning there is no side-slip angle or asymmetric forces acting on the aircraft.
- **Steady Aerodynamic Forces:** Aerodynamic forces and moments are assumed to be steady and functions of the current state variables (e.g., velocity, angle of attack).
- **No Wind or Turbulence:** Environmental effects such as wind and turbulence are neglected for simplicity. This includes ground effect as well.
- **Ideal Fluid Behaviour:** The air is considered to be incompressible, irrotational, non-viscouse, and continuous with uniform properties such as density and temperature.
- **Simplified Slipstream Models:** The thrust induced velocity flow on the wing and horizontal tail is assumed to be constant and uniform. It is also therefore assumed to be fully developed over the wing. Also, the wing planform is assumed to be fully immersed in the slipstream, with no wing segment in free stream and no turbulent transition.
- **Non-interacting Control Surfaces:** The effects of control surface deflections (in this case the flaps and the elevator) are assumed to be independent of each other, simplifying the control force and moment calculations.
- **Simplified Wing-Tail Interaction:** The distortion of the air mass from the interaction with the wing is assumed to be uniform and constant.
- **Independent Rotation and Airflow:** Pitching moments are considered to have no impact on the angle of attack of the nose tip and tail. This assumption is design to reduce the complexity of the trimming algorithm, for which rotations are assumed to be zero anyway.

4.2. Estimating Forces

In this section, the methods used to estimate the external forces are examined. The aerodynamics forces are estimated, while the propulsive forces are solved for through trimming. In Section 4.2.1, the propulsive forces are used to determine the necessary control surface deflection (collective rotor blade pitch angle) and throttle input (engine rpm), as well as the magnitude of the induced velocity. Then, Section 4.2.2 thru to Section 4.2.4 describe methods used for estimating the various aerodynamics forces.

4.2.1. Thrust

While the thrust forces are obtained for trimmed flight condition by solving the equations of motion, they can be further broken down to obtain the necessary pilot inputs. Using helicopter theory, the thrust forces are used to solve for the pilot control inputs, namely the collective blade pitch angle and rotor rotational rate, and the induced flow. The assumptions involved in this are listed below.

- **Uniform Inflow Assumption:** The flow velocity is assumed to the be uniform and linear across the rotor disk.
- **Quasi-Steady Aerodynamics:** The aerodynamic forces are assumed to respond instantaneously to changes in blade motion and flow conditions.
- **Two-Dimensional Aerodynamics:** Each blade element is treated as an airfoil section with lift and drag characteristics based on two-dimensional airfoil theory.
- **Actuator Disk Theory:** The rotor is modeled as an infinitely thin disk that imparts a uniform velocity increase to the flow passing through it.
- **Induced Velocity:** The rotor wake from the main propellers is assumed to be sufficiently far from the wing to be fully formed and uniform.
- **No Propeller Flapping:** Hindson et al. (1993) clarify that the CL-84 has “the absence of any propeller flapping or degree of freedom”(p394).
- **Rotational Speed:** The propellers are assumed to rotate such that the blade tip velocity is 98% of local mach speed.
- **Average Lift Coefficient:** c_{l_α}, the average coefficient of lift of the propeller blades, describes the average lift produced along the entire blade, up to the hub. It is assumed to be 0.1 $\frac{1}{rad}$.
- **No Tail Rotor Downwash:** The tail rotor’s downwash is assumed to have no incidence at all on any other surface, including the horizontal stabilizer.
- **Propeller Drag:** The tail rotor drag is assumed to be contained within the empennage estimated drag and the main rotors drag by the wing drag force.

The thrust coefficient can be obtained from blade element momentum (BEM) theory and Glauert’s method as described by van Holten and Melkert (2002) (p93). The thrust is converted to a non-dimensional coefficient using $T = C_T \pi \rho (\Omega R)^2 R^2$. Without any flapping considerations, both BEM theory and Glauert’s methods for the thrust coefficient simplify greatly. Glauert’s formula, Equation 4.2 can be directly used to determine the induced velocity λ_i, and blade element momentum theory can be used to determine the blade collective pitch θ_o required.

$$C_{T_{BEM}} = \frac{1}{n_b} c_{l_\alpha} \left[\frac{2}{3} \theta_0 \left(1 + \frac{3\mu^2}{2} \right) - (\lambda_c + \lambda_i) \right] \tag{4.1}$$

$$C_{T_{Glau}} = \lambda_i \sqrt{\left(\frac{V}{\Omega R} cos(\alpha_c) \right)^2 + \left(\frac{V}{\Omega R} sin(\alpha_c) + \lambda_i \right)^2} \tag{4.2}$$

In this report, the approach taken by helicopter flight dynamics of assuming a constant propeller rotation, Ω, is adopted. This assumption can be found in van Holten and Melkert (2002) or Pavel (1996)’s work as well. In fact, the CL-84 scheduled the pilot throttle inputs to control the propeller rates per minute (rpm) and propeller collective blade pitch angle, θ_o according to a schedule based on wing tilt angle. However, the specifics of the schedule could not be retrieved, and designing such a schedule is outside the scope of this work. Therefore, the rpm of the rotors are assumed to be fixed with respect to the airspeed so as to maintain the propeller tip velocity to 98% of mach speed. Consequently, the advance ration, μ, is also

invariable for a given airspeed V at a given angle of attack on the rotor disk plane. It should be noted that both the wing tilt angle η and the fuselage pitch attitude θ influence the angle α_c.

The angle of attack on the rotor disk naturally varies between the main rotors and the tail rotor, as described by Equation 4.3 and Equation 4.4. These equations are taken from van Holten and Melkert (2002) and adapted for a rotor without cyclic control input. From there, μ and λ_c are calculated in equivalent ways for the tail and main rotors. According to van Holten and Melkert (2002), α_c is defined as the angle between the control plane and the free stream velocity, positive when the rotor is tilted downward compared to free stream velocity. In this case without flapping, the control plane is identical to the disk plane. For the tail rotor, this implies Equation 4.4. For the main rotors, Equation 4.3 corrects for the convention for the wing tilt angles, which is $90°$ in the hover configuration.

$$\alpha_{c_{main}} = \frac{\pi}{2} - \eta - \alpha_{fuselage} \tag{4.3}$$

$$\alpha_{c_{tail}} = -\alpha_{fuselage} \tag{4.4}$$

$$\mu = \frac{V cos\alpha_c}{\Omega R} \tag{4.5}$$

$$\lambda_c = \frac{V sin\alpha_c}{\Omega R} \tag{4.6}$$

4.2.2. Wing

The forces and moments produced by the wings are of primordial importance to model the behaviour of a tilt wing aircraft. There are several complications that need to be addressed: the angle of attack can reach very high values, well into non-linear post-stall behaviour; the slipstream created by the main engines becomes very important because it affects the angle of attack on the wings; the flap movement affects both maximum lift coefficient and the effective angle of attack.

The CI-84 made use of NACA63_3418 airfoils on the wings, and Englar and Kirkpartick (1969) took the time to experimentally determine the lift and drag coefficients of the airfoil with the leading edge devices used on the CL-84. They produced the lift and drag coefficients curves with respect to angle of attack ranging from $\alpha = [-90 \quad 90]$, included a consideration for Krüger leading edge devices. The graph they produced in Figure 4.2 is overlayed with the polynomial fitted curves for both the lift and drag coefficients. Using a polynomial fit facilitates the use of numerical solver algorithms compared to look-up tables. For both the lift and drag coefficients, a curve using 30 polynomial terms were used to approximate their values continuously.

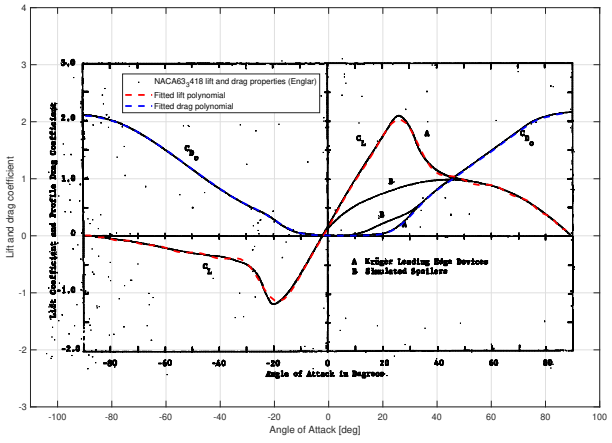

Figure 4.2: Lift and profile drag coefficient at angles of attack [-90 90] degrees (Englar and Kirkpartick, 1969) with polynomial fitted overlap

Next, the slipstream caused by the propeller blades accelerating the flow of air around the wings and horizontal stabilizer must be considered. This is a crucial consideration because the effectiveness of the

wings depend enormously on the slipstream during low-speed flight and with the wing tilt causes extremely high free stream angles of attack that would ordinarily stall the wing. Thanks to the accelerated airflow from the propellers, assumed to be exactly parallel with the wing chord direction, the angle of attack over the wing is greatly reduced.

Although the variable β is used by Englar and Kirkpartick (1969) to identify the angle of attack change due to slipstream, this report will refer to this angle as ζ to avoid confusion with the angle of sideslip relevant to lateral-directional considerations. To determine the slipstream angle ζ, the velocity vectors can be converted to pressure vectors (Englar et al, 1969). This is shown visually in Figure 4.3, with the propeller induced velocity corresponding to the propeller thrust per propeller disk area, and the free stream velocity relating to the dynamic pressure. Then, the slipstream velocity can be deduced from the slipstream dynamic pressure. In other words, $\bar{q} = 0.5\rho V^2$, $\bar{q}_s = 0.5\rho {V_s}^2$, and $2v_i = T_p S_p$.

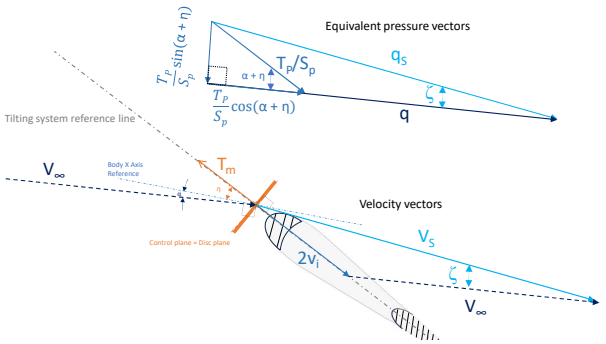

Figure 4.3: Geometrical representation of rotor slipstream effect on angle of attack

From Figure 4.3, it follows that the slipstream angle can be approximated as in Equation 4.7 (Englar and Kirkpartick, 1969). Using the slipstream angle, both the slipstream angle of attack and slipstream dynamic pressure can be determined as Equation 4.8 (Englar and Kirkpartick, 1969) and Equation 4.9. Although Englar and Kirkpartick (1969) solve for the slipstream dynamic pressure implicitly with Equation 4.10, this report prefers the explicit Equation 4.9 based on the schematic of the equivalent pressure vectors in Figure 4.3.

$$\zeta = \arctan\left[\frac{T_m sin(\eta+\alpha)}{S_p\bar{q} + T_m * cos(\eta+\alpha)}\right] \tag{4.7}$$

$$\alpha_s = \eta + \alpha - \zeta \tag{4.8}$$

$$\bar{q}_s = \sqrt{(\bar{q} + \frac{T_m}{S_p}cos(\eta+\alpha))^2 + \frac{T_m}{S_p}sin(\eta+\alpha)^2} \tag{4.9}$$

$$\bar{q} = \bar{q}_s cos(\zeta) - \frac{T_m}{S_P}cos(\eta+\alpha) \tag{4.10}$$

To account for the added lift and drag from the flap deflection, there are two key components to consider. First, the effective angle of attack on the entire wing is altered, as shown in Figure 4.4 (Anderson, 2012). Second, the lift coefficient curve is incremented by some factor depending on the type of flap.

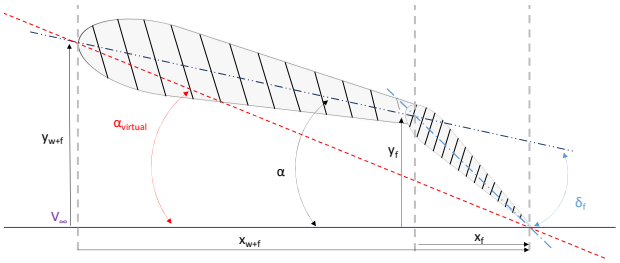

Figure 4.4: Change in effective angle of attack on wing with flap deflection

To determine the effective angle of attack on the wing using the geometry in Figure 4.4, the wing and flap chord geometry is considered. Equation 4.11 thru to Equation 4.15 step through the calculations to obtain the effective angle of attack on the wing.

$$x_f = \bar{c}_f cos(\alpha_s + \delta_f) \tag{4.11}$$
$$x_{w+f} = x_f + (\bar{c}_w - \bar{c}_f) cos(\alpha_s) \tag{4.12}$$
$$y_f = \bar{c}_f sin(\alpha_s + \delta_f) \tag{4.13}$$
$$y_{w+f} = y_f + (\bar{c}_w - \bar{c}_f) sin(\alpha_s) \tag{4.14}$$
$$\alpha_w = arctan(\frac{y_{w+f}}{x_{w+f}}) \tag{4.15}$$

This report attributes the additional drag provided by flap deflection entirely to the increase in angle of attack. However, the addition to lift also depends on the type of flaps used. In the case of the CL-84, the flaps are single slotted. To determine the increment, the DATCOM method is used as described by Scholz (2017). According to this method, the additional lift provided is expressed by Equation 4.16

$$\Delta_{c_{l_{flap}}} = k_{1_f} k_{2_f} k_{3_f} \Delta_{c_{l_{flap,max}}} \tag{4.16}$$

Each component in Equation 4.16 can be determined from statistical data available in DATCOM documentation. Figure 4.5 thru to Figure 4.8 below were used to determine the appropriate parameters to complete Equation 4.16.

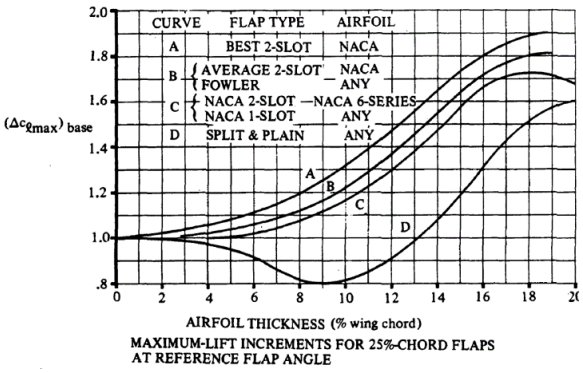

Figure 4.5: $\Delta_{c_{l_{flap,max}}}$ for 25%-chord flaps at a reference flap angle (Scholz, 2017)

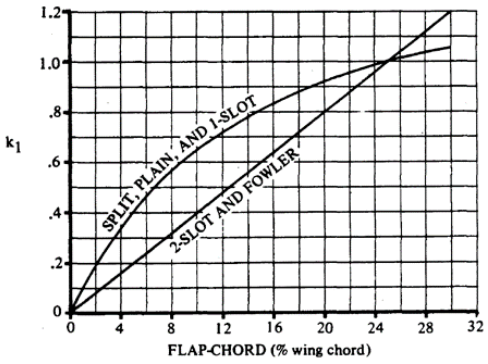

Figure 4.6: Factor for the relative flap chord with reference 25% (Scholz, 2017)

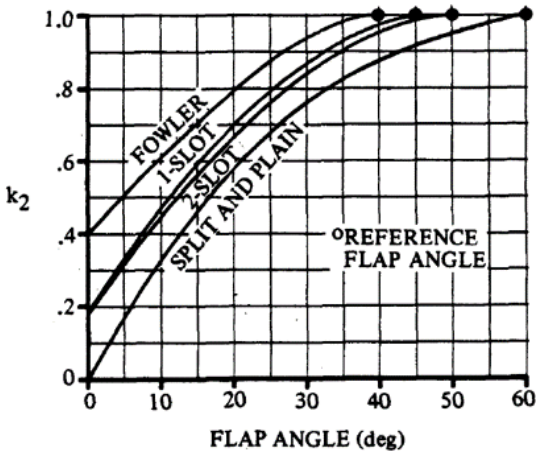

Figure 4.7: Factor for the flap deflection angle past the reference value (Scholz, 2017)

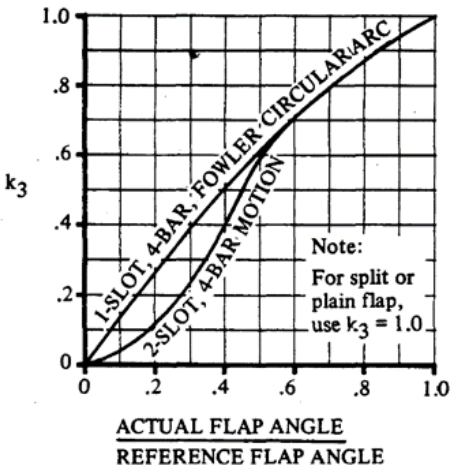

Figure 4.8: Factor for the flap kinematics based on flap shape (Scholz, 2017)

From Figure 4.5, single slotted flaps of NACA 6-series can be obtained from curve C, and for the NACA6_6418 airfoil with 18% thickness, this value lands at 1.72. Then, because the CL-84's flaps represent roughly 15%,rather than 25%, of the wing chord, a value of 0.81 was used for k_1. For k_2 and k_3, linear approximations were used because these values changed with flap deflections angles. For single slotted flaps, the reference angle on Figure 4.7 by a filled dot indicates 45°, so this value was used to make the linear approximation described in Equation 4.17 and Equation 4.18. In both those equation, the flap deflection angle is expressed in degrees, not radians.

$$k_2 = 0.2 + \delta_f \cdot 0.024 \tag{4.17}$$

$$k_3 = \frac{\delta_f}{45} \cdot 1.188 \tag{4.18}$$

Finally, the CL-84 had a scheduled flap deflection program associated with the pilot's angle of wing tilt (Nieusma, 1993). This schedule was replicated using a bell curve function, and the schedule used by Nieusma (1993) can be seen side by side with the one used in this report in Figure 4.9.

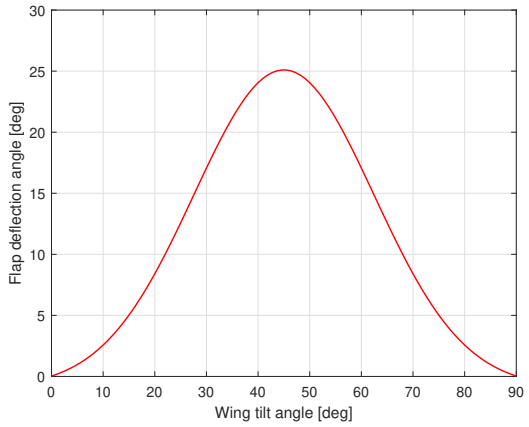

Figure 4.9: Flap schedule used in this report

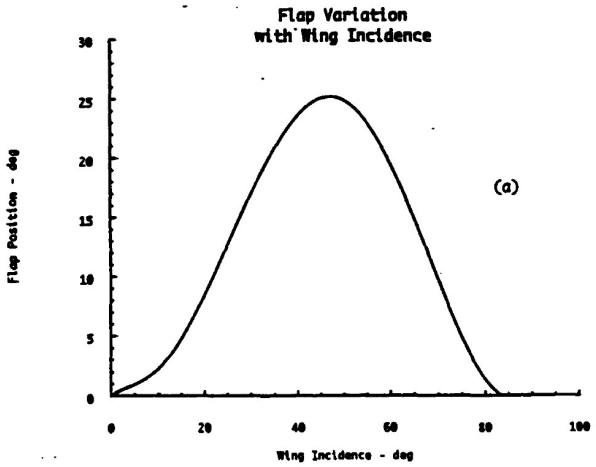

Figure 4.10: CL-84 flaps schedule (Nieusma, 1993)

The relationship used to create Figure 4.9 is shown in Equation 4.19 below. The flap schedule is set to a nominal value of 0° for $\eta > 90°$ and $\eta < 0°$.

$$\delta_f(deg) = 26e^{\frac{-(\eta-45)^2}{0.9 \cdot 26^2}} - 0.9 \tag{4.19}$$

To determine the resultant lift force acting on the wings, the lift coefficient is obtained by evaluating the polynomial fit shown in Figure 4.2 and the contribution of lift from the flap deflection at the effective angle of attack, considering slipstream and flap deflection contribution to the angle of attack. The resulting lift force is expressed by Equation 4.20. As a reminder, the lift force is always perpendicular to the direction of incoming flow velocity, which in this case is the resultant slipstream and not the effective angle of attack due to flap deflection. This also means that the induced drag from the afterward component of the lift vector is taken into consideration.

$$L_W = q_s S_I (C_{L_w} + \Delta_{c_{l_{flap}}}) \tag{4.20}$$

The drag coefficient is similarly obtained from evaluating Figure 4.2 at the effective angle of attack. Then, the drag force is calculated using Equation 4.21. The drag force is always parallel to the direction of incoming flow velocity.

$$D_W = q_s S_I C_{D_w} \tag{4.21}$$

To estimate the moment generated by the wing, the locations of the aerodynamic center and center of gravity from Appendix B are used. Because the wing tilt may significantly affect the arms in the X and Z body axis, these are corrected for the wing tilt angle as shown in Appendix C. The resultant lift vector is separated into X and Z components. The result is shown in Equation 4.22.

$$M_{AC_W} = L_W z_{(Wac-Wgc)} sin(\alpha_w) + L_W x_{(Wac-Wgc)} cos(\alpha_w) \tag{4.22}$$

4.2.3. Tail

The horizontal tail is modeled in two separate components, an all-moving horizontal stabilizer and an elevator. The pilot command controls the deflection on the elevator surface only, while the horizontal stabilizer is scheduled to deflect up to $45°$based on the tilt angle of the wing. This schedule of the CL-84 is shown in Figure 4.12 and the implementation to this report's model is shown in Figure 4.11.

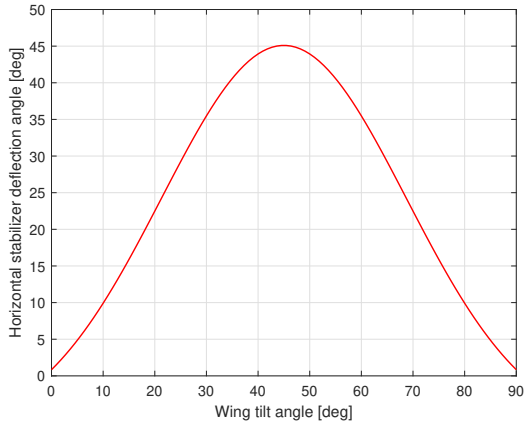

Figure 4.11: Horizontal stabilizer schedule used in this report

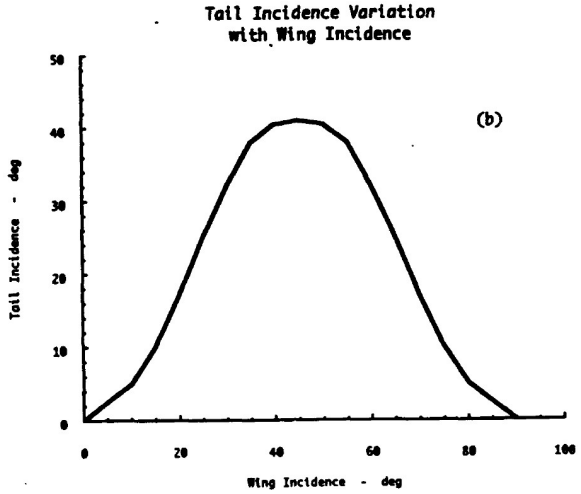

Figure 4.12: CL-84 Horizontal stabilizer schedule (Nieusma, 1993)

The curve displayed in Figure 4.11 is obtained using Equation 4.23 below. The horizontal stabilizer schedule is set to a nominal value of 0° for $\eta > 90°$ and $\eta < 0°$.

$$\delta_{HS}(deg) = 53e^{\frac{-(\eta-45)^2}{0.4 \cdot 53^2}} - 7.9 \tag{4.23}$$

Although the same slipstream angle of attack used on the wing is assumed to be applicable to the horizontal stabilizer, an additional effect caused by the wing's downwash needs to be considered as well (Gudmundsson, 2014). This effect can be estimated using the lift coefficient at the wing as shown in Equation 4.24, with $c_{l_{W-o}}$ being the constant value of the wing's lift coefficient at $\alpha = 0$.

$$\varepsilon = \frac{2 * (c_{l_{W-o}} + c_{l_W})}{\pi AR} \tag{4.24}$$

Hence, the effective angle of attack on the horizontal stabilizer depends on the angle of attack on the fuselage corrected for the rotor slipstream, wing downwash, and horizontal tail schedule, as shown in Equation 4.25:

$$\alpha_{HS} = \alpha + \delta_{HS} - \zeta - \varepsilon \tag{4.25}$$

The elevator is not modelled in the same way at the flaps to avoid over-complication based on arbitrary assumptions. Instead, the elevator is modeled as a lifting surface behind the horizontal stabilizer and its deflection increment on the effective angle of attack of the horizontal stabilizer, $\alpha_e = \alpha_{HS} + \delta_e$.

Further, the airfoil used for the horizontal tail cannot be assumed to be the same NACA-6 series airfoil as the wing because the horizontal stabilizer needs to be equally capable of positive and negative forces. A more reasonable assumption is to considered a symmetrical airfoil, such as NACA0012. Fortunately, information about how this airfoil behaves at large angles of attack, from 0°to 360°, can be found (Critzos et al., 1955). The moment, drag, and lift coefficient curves are approximated using symbolic approximation (as opposed to look-up tables) so that any embedded variable could still be solved for in the trim process. The approximations of the curves are shown in Figure 4.13, Figure 4.14, and Figure 4.15. The estimates are a bit more faithful to the experimental curves close to 0°and allowed to stray at very high angles of attack because it was observed that for normal flight conditions the effective angle of attack on the tail

didn't far exceed the stall dynamics. This effect is attributable to the slipstream and wing-tail interference assumptions.

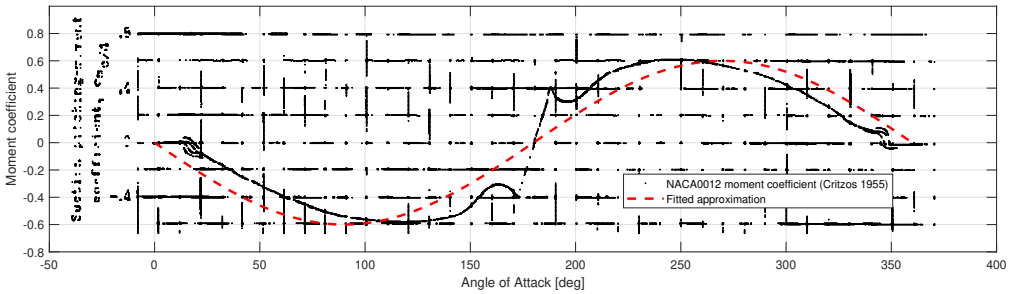

Figure 4.13: Approximation of NACA0012 $C_m(\alpha)$ from Critzos et al. (1955)

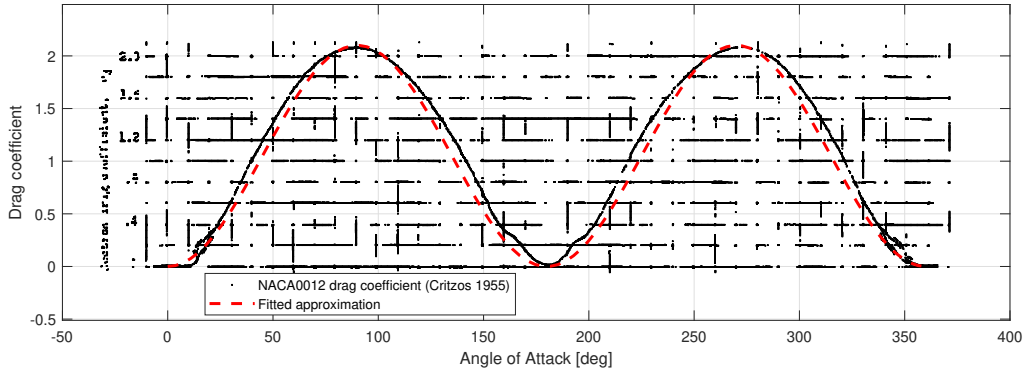

Figure 4.14: Approximation of NACA0012 $C_D(\alpha)$ from Critzos et al. (1955)

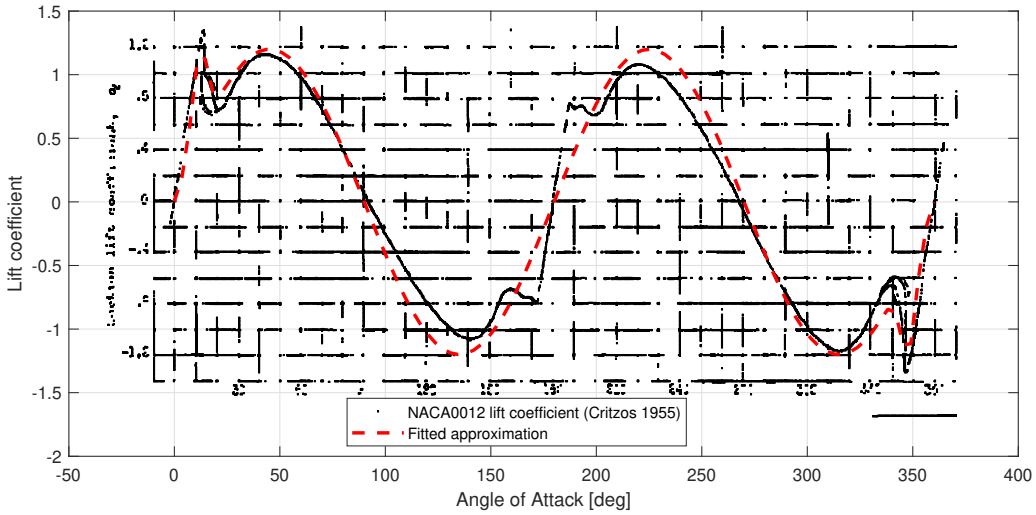

Figure 4.15: Approximation of NACA0012 $C_L(\alpha)$ from Critzos et al. (1955)

The coefficients are approximated analytically by Equation 4.26, a combination of sinusoidal and bell curves. The forces and moments on the horizontal stabilizer and elevator are estimated by Equation 4.27

and Equation 4.28 using the coefficients obtained with the relevant angle of attack.

$$C_{M_{NACA0012}} = \pm\left(-0.3e^{-0.014(\alpha_{eff}-90)^2} - 0.8e^{-0.015(\alpha_{eff}-120)^2} + 0.5e^{-0.011(\alpha_{eff}-120)^2} + 0.29e^{-0.05(\alpha_{eff}-170)^2}\right)$$
$$C_{D_{NACA0012}} = \pm\left(1.25e^{-0.014(\alpha_{eff}-90)^2} + 1.75e^{-0.026(\alpha_{eff}-90)^2} - e^{-0.013(\alpha_{eff}-90)^2}\right)$$
$$C_{L_{NACA0012}} = 1.2sin(2\alpha_{eff}) \pm \left(0.7e^{\frac{-(\alpha_{eff}-12)^2}{40\cdot 0.8^2}}\right) \tag{4.26}$$

$$L_{HS} = C_{L_{HS}} q_s S_{HS} \tag{4.27}$$
$$D_{HS} = C_{D_{HS}} q_s S_{HS}$$
$$M_{AC_{HS}} = C_{M_{HS}} q_s \bar{c}_{HS} S_{HS}$$
$$L_e = C_{L_e} q_s S_e \tag{4.28}$$
$$D_e = C_{D_e} q_s S_e$$
$$M_{AC_e} = C_{M_e} q_s \bar{c}_e S_e$$

4.2.4. Miscellaneous forces

This model is also equipped to consider the forces and moments originating from two other sources, the fuselage and the nacelles. However, in order to maintain as much simplicity in the model as possible, the effect of the nacelles were ignored in this report except to consider the location of the center of gravity. Both of these aerodynamic surfaces are estimated in keeping with previous research from Englar and Kirkpartick (1969). For the nacelle, the angle of attack used was the same as the effective angle of attack on the wing sections immersed in slipstream. Then, the lift and drag coefficients are estimated using Equation 4.29.

$$C_{L_N} = C_{d_b} sin^2(\alpha_s) cos(\alpha_s) \tag{4.29}$$
$$C_{D_N} = C_{d_b} sin^3(\alpha_s) + C_{d_{on}} \tag{4.30}$$

In Equation 4.29, C_{d_b} is the basic cylindrical drag coefficient, assumed to be 1 and $C_{d_{on}}$ is the nacelle profile drag coefficient, assumed to be 0.045 (Englar and Kirkpartick, 1969). Those coefficients become forces using Equation 4.31. A factor of two needs to be used to consider that there are two nacelles.

$$L_N = 2q_s S_N C_{L_N} \tag{4.31}$$
$$D_N = 2q_s S_N C_{D_N} \tag{4.32}$$

Similarly, the fuselage-empennage combination is estimated using Equation 4.33, using the same basic cylindrical drag coefficient.

$$C_{L_F} = C_{d_b} sin^2(\alpha) cos(\alpha) \tag{4.33}$$
$$C_{D_F} = C_{d_b} sin^3(\alpha) + C_{d_{of}} \tag{4.34}$$

The fuselage is approached using a combination of methods from Pavel (1996) and Englar and Kirkpartick (1969). The fuselage profile drag coefficient at $\alpha = 0$ could be determined to be $C_{d_{of}} = 0.0167$ (Nieusma, 1993). Then Equation 4.35 can be used to obtain the forces.

$$L_F = q_s S_N C_{L_F} \tag{4.35}$$
$$D_F = qS_F C_{D_F} + qF_f \tag{4.36}$$

The fuselage equivalent area S_F is determined using the geometry of the CL-84 (see Appendix B for more details. A plane plate is used to estimate the equivalent parasite area to be 40% of the fuselage equivalent area (Pavel, 1996). The drag force equation from Englar and Kirkpartick (1969) can then be completed using that information.

4.3. Equations of Motion

In this Section, the equations of motion are derived from the schematic representation, Figure 4.1, shown in Section 4.1.These equations can be written in their general form as shown in Equation 4.37, taken from Durham (2013) with adapted notation. To avoid complicated notation, all forces and moments are assumed to be in the body-fixed reference frame defined in Appendix D unless stated otherwise.

$$m\frac{d}{dt}(\boldsymbol{V}) + \boldsymbol{\Omega} \times m\boldsymbol{V} = \boldsymbol{\Sigma F} \tag{4.37}$$
$$\boldsymbol{I}\frac{d}{dt}(\boldsymbol{\Omega}) + \boldsymbol{\Omega} \times \boldsymbol{I\Omega} = \Sigma \boldsymbol{M}$$

For convenience, the forces and moments are separated for each axis by their origin: propulsive, aerodynamic, or control surface deflection. This distinction is indicated in the under-script, with a P for propulsion, W for the for aerodynamic forces on the wing, f for the fuselage, HT for the horizontal tail, and δ_e for the elevator. The weight is represented by a W. The notation echoes the one shown in Figure 4.1. The addition of the relation $\dot{\theta} = q$ is superfluous in this case because the equations are evaluated at trim when both $\dot{\theta} = 0$ and $q = 0$.

$$m\dot{u} + qw = X_P + X_W + X_f + X_{HT} + X_{\delta_e} - Wsin(\theta) \tag{4.38}$$
$$m\dot{w} - qu = Z_P + Z_W + Z_f + Z_{HT} + Z_{\delta_e} + Wcos(\theta) \tag{4.39}$$
$$\dot{q}I_{yy} = M_P + M_W + M_{HT} \tag{4.40}$$

$$\begin{aligned} X_P &= T_m cos(\eta) \\ X_W &= -L_W sin(\zeta - \alpha) - D_W cos(\zeta - \alpha) \\ X_f &= -D_f cos(\alpha) + L_f sin(\alpha) \\ X_{HT} &= -L_{HT} sin(\varepsilon - \alpha_{HT}) - D_{HT} cos(\varepsilon - \alpha_{HT}) \\ X_{\delta_e} &= -L_{\delta_e} sin(\varepsilon - \alpha_{HT}) - D_{\delta_e} cos(\varepsilon - \alpha_{HT}) \end{aligned} \tag{4.41}$$

$$\begin{aligned} Z_P &= -T_m sin(\eta) - T_t \\ Z_W &= -L_W cos(\zeta - \alpha) + D_W sin(\zeta - \alpha) \\ Z_f &= -D_f sin(\alpha) - L_f cos(\alpha) \\ Z_{HT} &= D_{HT} sin(\varepsilon - \alpha_{HT}) - L_{HT} cos(\varepsilon - \alpha_{HT}) \\ Z_{\delta_e} &= D_{\delta_e} sin(\varepsilon - \alpha_{HT}) - L_{\delta_e} cos(\varepsilon - \alpha_{HT}) \end{aligned} \tag{4.42}$$

$$\begin{aligned} M_P &= T_m sin(\eta) x_{prop} - T_m cos(\eta) z_{prop} - T_t x_{T-prop} \\ M_W &= -Z_W x_W - X_W z_W + M_{AC_W} \\ M_{HT} &= -X_{HT} z_{HT} + Z_{HT} x_{HT} + M_{AC_{HT}} - X_{\delta_e} z_{\delta_e} + Z_{\delta_e} x_{\delta_e} + M_{AC_{\delta_e}} \end{aligned} \tag{4.43}$$

4.3.1. Trim

The full sequence used to solved the equations for trim control inputs is provided in Appendix A. Nevertheless, several noteworthy decisions were necessary. The first observation is that the aircraft is over-actuated: even after assuming an altitude and scheduling the flaps and horizontal stabilizer movement there are 7 possible control settings (η, u, w, T_m, T_t, δ_e, θ) for only 3 distinct equations. It is therefore necessary to assign a value to some of the trim settings and determine for which flight condition the trim is requested. In view of obtaining a transition corridor, η is selected. Also, the usual flight dynamics trick of setting some of the trim settings can reduce this problem. In this report, the trim sequence assumes level flight, so w is set to zero. Since the forward speed u is also typically chosen to determine the flight condition, this choice is also made here. Then, recalling that the tail rotor for the CL-84 phases out as the wings reach a horizontal attitude, the approach adopted toward the elevator δ_e and tail rotor T_t was adjusted accordingly. According to Longhurst (1966), the tail rotor effectiveness was phased out as the wing tilt angle lowered, but exact mechanism is left out. It was determined experimentally that the model presented in this report no longer needs the tail rotor for trimmed flight, so it is phased out around in that region. Beyond that region, the trim

algorithm sets the fuselage pitch attitude θ to 0 and solves for the required elevator deflection angle δ_e. While the tail rotor is still active, the trim algorithm struggles to solve for a level fuselage attitude when the forward speed is prescribed, because the elevator loses effectiveness near the hover configuration. The angle of attack on the horizontal tail naturally fluctuates with the wing tilt angle due to the slipstream and wing-tail interference effects, so the elevator deflection angle is set to counteract those changes. Since the three degree of freedom model is used a proof of concept, the elevator deflection angle was simply set to $-2\alpha_{HS}$. This parameter is explore a little more on the six degree of freedom model. The algorithm used to solve the equations of motion and trim the aircraft is MATLAB's vpasolve function, a variable point algorithm. It is selected because a numerical solver is desirable to resolve the combination of sinusoidal, exponential, and polynomial unknown parameters.

The over-actuated nature of the aircraft is addressed in this report by choosing values for the excess control variables. An optimization approach was considered to be outside the scope of this report to prioritize obtaining insight into the natural behaviour of the tilt wing.

The output of the trimming process is shown in Figure 4.16.

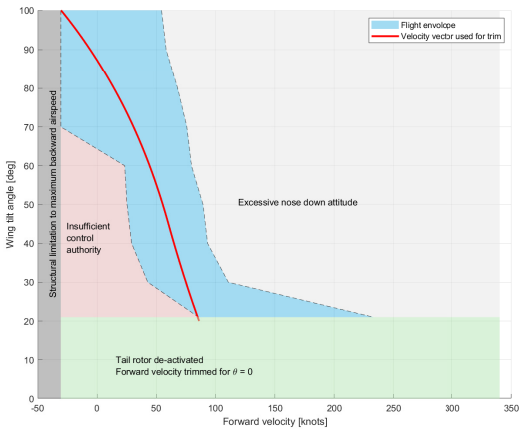

Figure 4.16: Wing tilt vs. forward velocity during transition

The red line shows an initial verification, with a continuous transition from hover to cruise configuration. The blue shaded area represents the space of flight conditions for which the model has a trim solution. To the left of it, the model indicates insufficient control authority. To the right of the blue area, the trim solution was deemed to require excessive fuselage pitch attitudes for practical flight applications. The green area represents the region for which the fuselage pitch attitude is set to 0, and the corridor is expected to be very large.

The transition corridor is reminiscent of transition data from other tilt-wing, such as May et al. (2021) found for the Vahana, and tilt wing drones, such as the configuration explored by Sanchez-Rivera et al. (2020).

5

Verification & Validation

The many simplifications and approximations of this model are such that the output is unlikely to exactly match the flight test data from the CL-84. Still, it is useful to compare the model output to the behaviour of the CL-84 shown in flight test data. In this section, two approaches will be used for partial validation of the model. First in Section 5.1, the general shape of the output is verified qualitatively to see how the wing angle transition compares to other tilt-wing models. These results are compared to the expected results discussed in Section 3.2. Then, in Section 5.2, the model output is compared to available flight test data from the CL-84 and the a previous CL-84 model (Nieusma, 1993).

5.1. Transition Corridor

This section discusses the transition corridor present in Figure 4.16. In particular, the red line is used as a verification means because it demonstrates a full continuous transition from backward flight all the way to wings-level cruise. The red line shown in Figure 4.16 is an input to the trim algorithm, then Figure 5.1 shows how the solution for the forward speed below $20°$ of wing tilt to maintain a level fuselage pitch attitude.

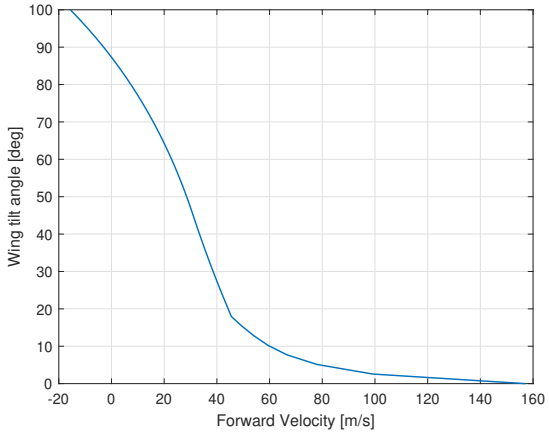

Figure 5.1: Wing tilt vs. forward velocity during transition

The elevator deflection angle is also an important indicator. As a reminder, it is set in this chapter to $-2\alpha_{HS}$. The result is shown in Figure 5.2. It is shown next to the fuselage pitch attitude in Figure 5.3 to better understand the elevator movement. At low speeds and with very little control authority, a large elevator deflection spike is required. At the same time, the fuselage pitch attitude is a little high. The elevator deflection in the positive increases the angle of attack, and works to stabilize the pitch attitude. Similarly, the reverse effect can be observed when the nose of the aircraft dips around 50 knots.

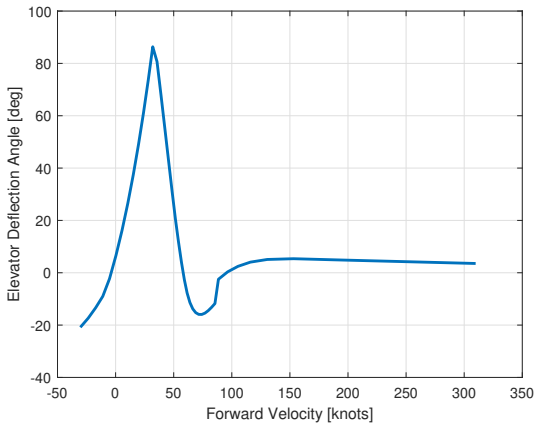

Figure 5.2: Elevator deflections angle δ_e vs. forward velocity u during transition

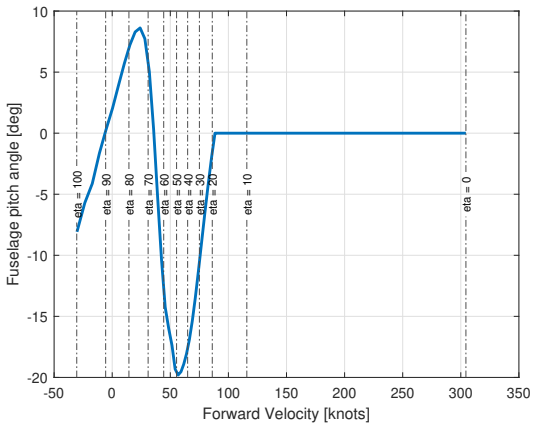

Figure 5.3: Fuselage attitude θ vs. forward velocity u during transition

The thrust parameters are also important examine because they determine the pilot control. Once again, the continuous mission is used for verification purposes. The trim thrust for the main and tail rotors combined is shown in Figure 5.4. The tendency follows a smooth bucket shape.

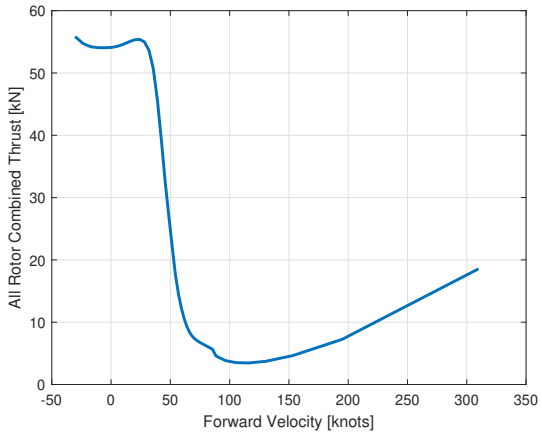

Figure 5.4: Transition combined thrust from main and tail rotor vs. forward velocity

The thrust is converted to pilot inputs using a rotational velocity Ω such that the rotor tip velocity remains at 98% of mach speed. The induced velocity, obtained by solving Glauert's equation from Equation 4.2, follows closely the coefficient of thrust and looks to be directly proportional to the thrust from Figure 5.4. This is an expected result because without flapping, the induced velocity and the thrust output are closely related. The main rotor induced velocity curve demonstrates a clear pattern. Without flapping, the Glauert equation for the thrust coefficient from Equation 4.2 takes on the simpler form of Equation 5.5, recalling that $\mu = \frac{V\cos(\alpha_c)}{\Omega R}$, $\lambda_c = \frac{V\sin(\alpha_c)}{\Omega R}$, and α_c is defined as $\frac{\pi}{2} - \eta - \alpha_{fus}$.

$$C_{T,Gla}{}^2 = \lambda_i{}^2 \left[\mu + (\lambda_c + \lambda_i)^2\right] \tag{5.1}$$

Therefore, when η is close to 90°, $\cos(\alpha_c)$ is close to 0, and μ also approaches 0. Near hovering configuration, Equation 5.5 approaches Equation 5.2. Considering $\lambda_c \ggg \lambda_i$, higher order forms of λ_i can be ignored to estimate the tendency, resulting in Equation 5.3.

$$0 = \lambda_i{}^4 + 2\lambda_i{}^3\lambda_c{}^2 + \lambda_i{}^2\lambda_c{}^2 - C_{T,Gla}{}^2 \tag{5.2}$$

$$0 = \lambda_i{}^2\lambda_c{}^2 - C_{T,Gla}{}^2 \tag{5.3}$$

Thus at high angles of wing tilt, λ_i is almost proportional to $\frac{C_T}{\lambda_c}$, which is in turn proportional to $\frac{T}{u}$ close to hover. Similarly, at low angles of wing tilt, $sin\alpha_c$ approaches 0, meaning that Equation 5.5 approaches Equation 5.4.

$$0 = {\lambda_i}^4 + {\lambda_i}^2\mu^2 - {C_{T,Gla}}^2 \tag{5.4}$$

Once again, higher order terms of λ_i can be ignored, resulting in λ_i proportional to $\frac{C_T}{\mu}$. Interestingly, for angles of wing tilt close to 0, this also tends toward proportionality with $\frac{T}{u}$.

The collective propeller pitch angle for the main rotors (left and right side are symmetrical) and the tail rotor are displayed in Figure 7.10 and Figure 7.11 respectively. In this case, the blade element momentum theory equation for the thrust coefficient, Equation 4.1 can also be simplified to examine the tendency of the collective propeller pitch.

$$\theta_o \propto C_{T,Gla}\frac{\lambda_c + \lambda_i}{1+\mu^2} \tag{5.5}$$

Once again, it can be considered that for large angles wing tilt, λ_c tends to 0 and for small angles wing tilt, μ tends to 0. Hence, close to hover configuration and with η close to $90°$, λ_c tends to 0, meaning that Equation 5.5 can be written as $\theta_o \propto \frac{T\lambda_i}{1+\mu^2}$. This explains the behaviour of Figure 7.10 around hover, with low angles of collective pitch. Then at small angles of wing tilt, the collective $\theta_o \propto \lambda_c + \lambda_i$. This can be further simplified by considering that λ_c is proportional to u at small angles of η and λ_i is very small compared to u. As a result, the collective pitch θ_o is proportional to u in the transition stages close to cruise configuration, as shown by the straight line extending linearly past 75 knots.

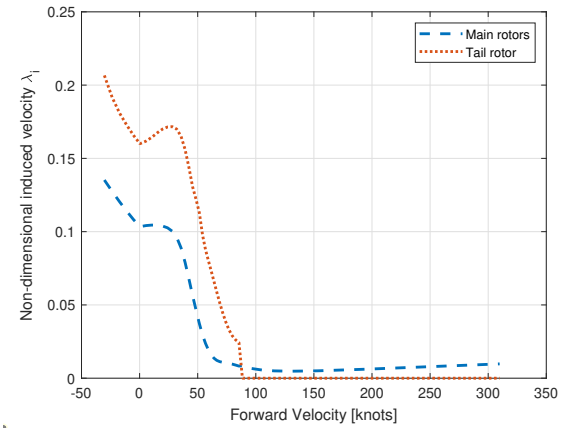

Figure 5.5: Induced velocity λ_i on the main and tail rotors vs. forward velocity

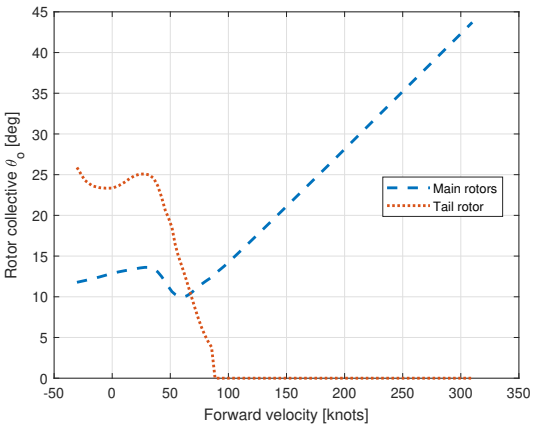

Figure 5.6: Collective propeller blade pitch θ_o on the main and tail rotors vs. forward velocity

Finally, the propeller blade pitch angle remains within the control limits of $[-5, 45]$ described by Nieusma (1993). Based on the trim results presented in this section, the most obvious improvement that can be made is the use of optimization. That would provide the user more control over the trim flight conditions, for example trimming a continuous transition with the fuselage as close as possible to level.

5.2. Validation

This section focuses on comparing the model output to available flight data of the CL-84 using graphs from Nieusma (1993). The flight test data available show the behaviour of the CL-84 are various angles of wing tilt, 85.1, 41.5, 28.6, 14, and 0. The wing level cruise condition test data depend largely on the power settings, which are not readily available, and therefore are trivial to replicate. Besides the hover flight condition at wing tilt andlge $\eta = 85.1$, the remaining flight conditions depend significantly on the elevator setting. Although the elevator position is provided by Nieusma (1993), the dimensions of the elevator are not. Unfortunately, reliable information on this topic was not readily available; the elevator is depicted in

Taylor (1960) but not sized. For this model, the elevator is assumed to be 30% of the size of the movable horizontal tail. Another complicating factor for comparison is that the horizontal tail is movable. In this model, the elevator deflection is considered to be a deviation from the horizontal stabilizer, but Nieusma (1993) does not specify if this is his interpretation as well. Due to the difficulty in comparing the pitch control inputs with the flight test data, the parameters used for the validation simulations are listed in tables next to the graphs. The four datasets used for validation are shown below. The model outputs in Figure 5.7 thru to Figure 5.10 were obtained by solving the trim routine for the thrust forces and fuselage pitch attitude at the relevant wing tilt angle in the prescribed velocity range used by Nieusma (1993). For simplicity, and since the elevator cannot be directly compared between the model, the flight tests, and Nieusma's simulation, it was kept to a single value during these validation runs.

The first configuration compared in Figure 5.7 is the hover configuration. The flaps deflection angle, δ_{flaps} and the horizontal stabilizer incidence angle, δ_{HS}, were specified for the flight tests and replicated by Nieusma (1993).

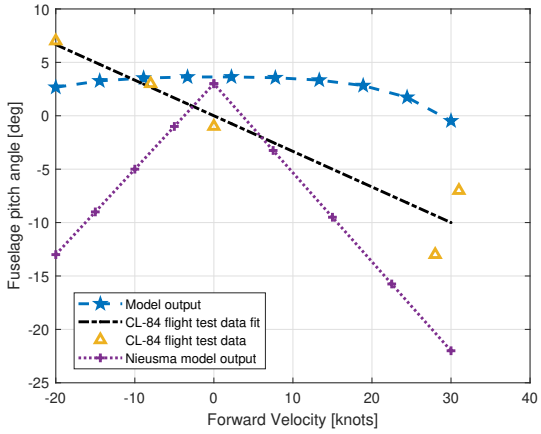

Figure 5.7: Variations in velocity at $85.1°$wing tilt compared to flight test data (Nieusma, 1993)

Parameter	Model Value	Flight test value	Nieusma value
δ_{flaps} [deg]	1	-	-
δ_{HS} [deg]	1	-1	-1
δ_e [deg]	0	-2 to 2	-1 to 8

Table 5.1: Comparison of accompanying parameters during flight test at $85.1°$wing tilt

Since the elevator control surface has fairly little control authority in hover, it is kept flush with the stabilizer. During the flight test and even in Nieusma's simulation, the elevator deflection angle increased linearly from one value to the other. The hover scenario is notoriously difficult to model correctly. The main reasons for this difficulty are the complexity of the aerodynamic interactions between the main and tail rotors slipstream and wing downwash effect on the horizontal tail (Nieusma, 1993). Nieusma (1993) also cites the lack of tail rotor to control surface interaction as a factor of difficulty in modeling the hover condition and backward flight in particular. Indeed, in forward flight it is easy to imagine the tail rotor wake inertly behind the flight path, but in hover and backward flight, this wake would sure have an impact on the control of the aircraft. Although the model's output pitch attitude doesn't match very closely the flight test data, the error is not staggering, especially when compared to the results obtained by the model offered by Nieusma (1993) for this flight condition.

The next flight condition, at wing tilt angle $\eta = 41.5°$ is shown in Figure 5.8 below. In this flight condition, there is already sufficient airspeed to assume the tail rotor wake does not interact with the control surfaces. The model's prediction of the aircraft pitch attitude closely matches the CL84's flight test data, suggesting a good level of reliability.

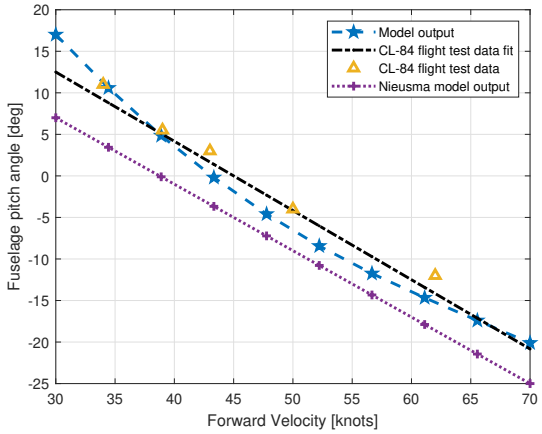

Figure 5.8: Variations in velocity at 41.5°wing tilt compared to flight test data (Nieusma, 1993)

Parameter	Model Value	Flight test value	Nieusma value
δ_{flaps} [deg]	24	-	-
δ_{HS} [deg]	35.5	35.5	40.5
δ_e [deg]	-3	-2 to -7	-2 to -3

Table 5.2: Comparison of accompanying parameters during flight test at 41.5°wing tilt

Then, the model's performance compared to flight test data at wing tilt angle $\eta = 28.6$° is shown in Figure 5.9. In this case, this model's estimates are not reliable at low speeds, but become indistinguishable from Nieusma's model around 55 knots. One possible determining explanation for the discrepancy at low speeds is that the model's simplifying assumptions regarding the rotor slipstream become much more important at low speeds. At higher airspeeds, the free stream component of the effective velocity on the wing and horizontal tail is dominant. But at low airspeeds, the dynamic pressure induced by the rotor slipstream is the dominant factor. Another point worth mentioning is that the line of best fit through the flight test data, transcribed from Nieusma (1993), extrapolates quite a bit from the flight test data and skirts the lower bound much more closely.

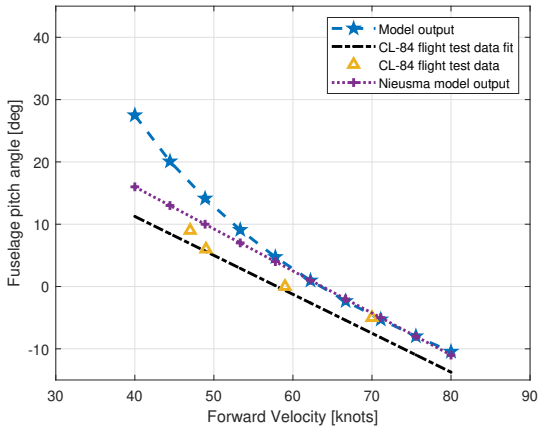

Figure 5.9: Variations in velocity at 28.6°wing tilt compared to flight test data (Nieusma, 1993)

Parameter	Model Value	Flight test value	Nieusma value
δ_{flaps} [deg]	15	-	-
δ_{HS} [deg]	30.0	23.5	30.0
δ_e [deg]	-1	-2 to -7	-1 to 2

Table 5.3: Comparison of accompanying parameters during flight test at 28.6°wing tilt

Finally, the model is validated at with wing tilt angle $\eta = 14°$, as shown in Figure 5.10. For this validation, the model remains within $2°$ of the flight test data, providing a very close estimate of the CL-84's behaviour. This validation, besides showing that the model developed is a fairly good predictor of the trim fuselage pitch attitude for the given flight conditions, also reveals something about the assumptions behind the elevator part of the model. Indeed, the elevator deflection is consistently approximately $7°$ higher than during the flight tests. This confirms that there are discrepancies between the way the elevator is modelled and the CL-84 elevator's true geometry.

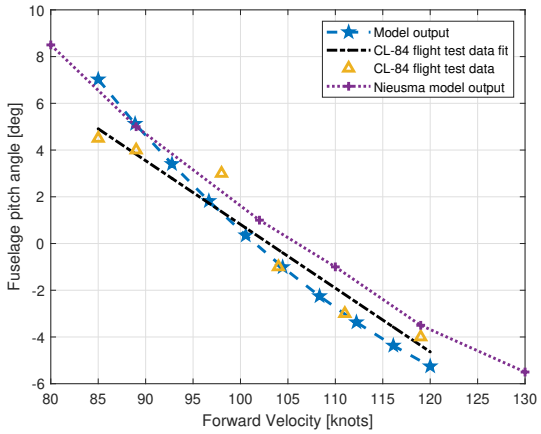

Figure 5.10: Variations in velocity at 14°wing tilt compared to flight test data (Nieusma, 1993)

Parameter	Model Value	Flight test value	Nieusma value
δ_{flaps} [deg]	4.5	-	-
δ_{HS} [deg]	10.1	10.1	9.0
δ_e [deg]	6 to 12	-1 to 4	2 to 7

Table 5.4: Comparison of accompanying parameters during flight test at 14°wing tilt

From the validation tests discussed in this sections, two conclusions are drawn. The first conclusion is that the rotor slipstream model and the aerodynamic effects on the tail in particular are over-simplified. This can be observed most clearly in the hover configuration, but also in flight conditions with relatively low forward speeds. The low forward speed amplifies the importance of the rotor slipstream's impact on the angle of attack, which highlights the fidelity gap. The second conclusion concerns the assumptions around the elevator. In particular, the validation test at $14°$ of wing tilt shows that the elevator is sized incorrectly. However, the discrepancy could lie in the moment arm, the chord, the span, or the airfoil selection. All those parameters were assigned with some uncertainty.

Part IV

Six Degree of Freedom Model

6

Development of a Lateral-Directional Extension

This chapter describes the extensions made to the previous chapter's longitudinal three degree of freedom model to obtain a six degree of freedom model that includes lateral-directional mechanics. First the schematic representation is extended with a front view and a top view in Section 6.1. Then, the lateral-directional forces and moments are estimated in Section 6.2. The equations of motion are presented in Section 6.3 and the output of the model is discussed in Chapter 7.

6.1. Schematic Representation

This section presents the schematic representation use to develop the six degree of freedmon model. The side-view, Figure 6.1 is repeated to provide a holistic representation, even though it is the same as Figure 4.1.

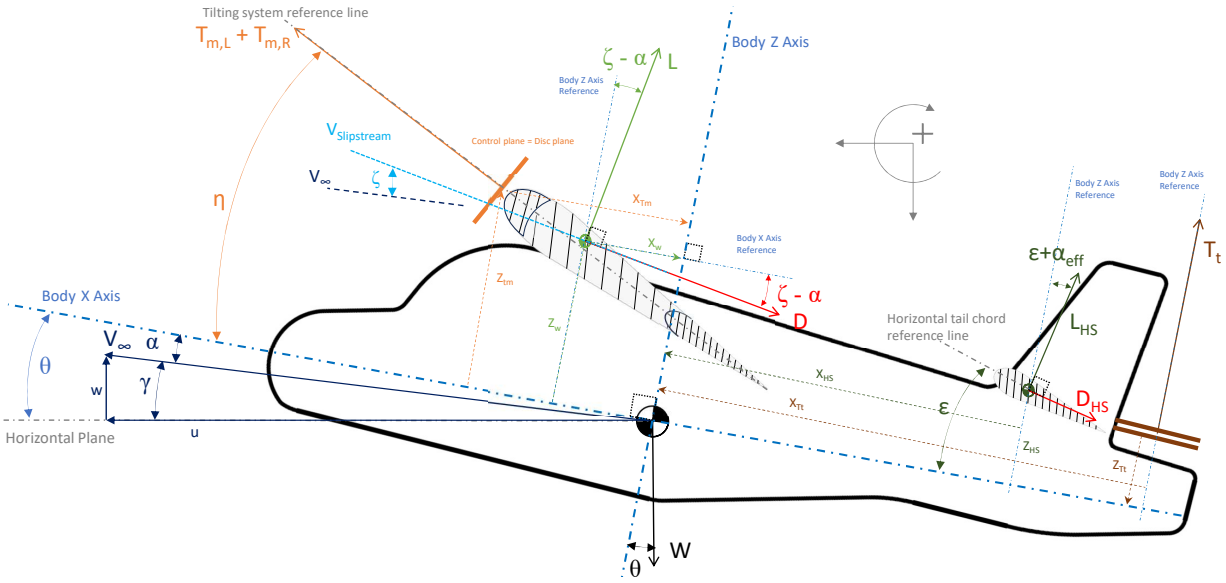

Figure 6.1: Forces, moments and velocities acting on the CL-84 in the XZ-plane

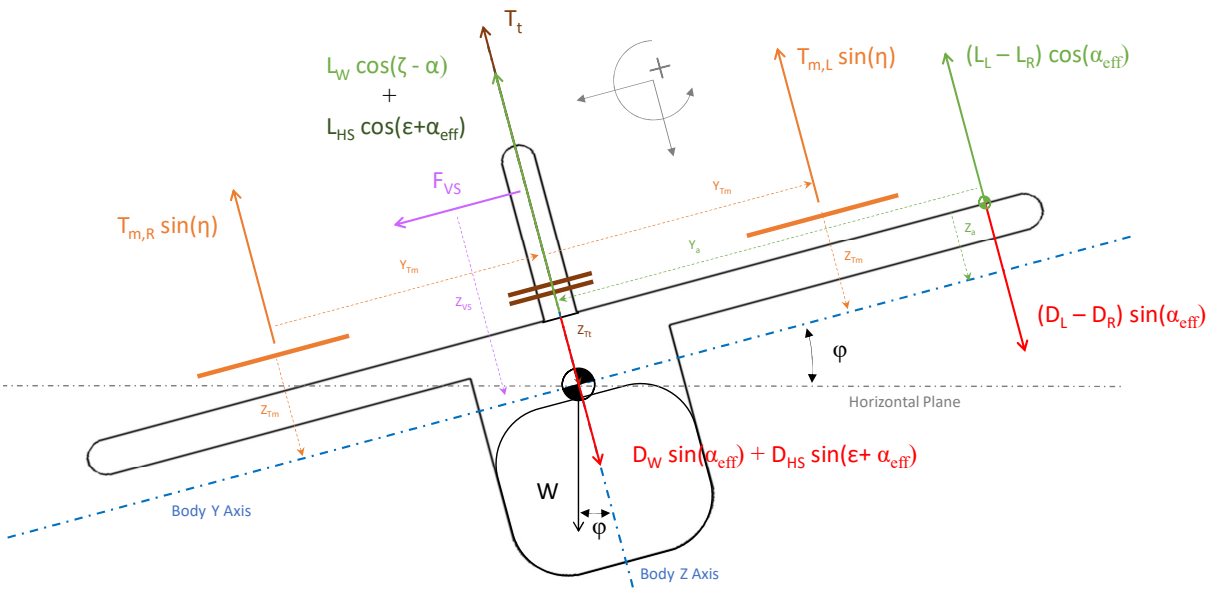

Figure 6.2: Forces, moments and velocities acting on the CL-84 in the YZ-plane

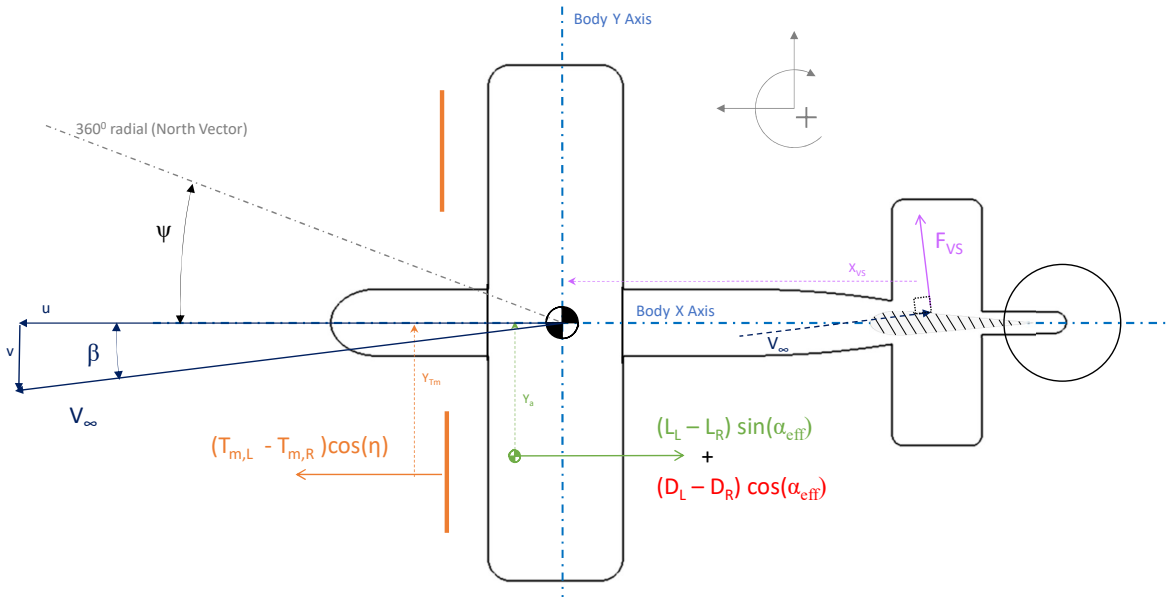

Figure 6.3: Forces, moments and velocities acting on the CL-84 in the XY-plane

The front view, Figure 6.2 and the top view, Figure 6.3 graphically indicate the use of the body-fixed coordinate system as described in Appendix D. The sign conventions for the rotational vectors p and r are consistent with the right-hand rule, with a positive roll p defined by lowering the right wing and a positive yaw r by pointing the nose to the right. Also, the angle of sideslip, β is defined by the aircraft's movement in the positive direction. As a departure from the three degree of freedom model developed in Chapter 4, the right and left thrust, wing lift, and wing drag values are separated to account for the possibility of differential thrust. The overall assumptions underlying the model are largely similar to the ones made in the development of the longitudinal model. The notable differences are detailed below:

- **Neglected Dynamics:** Only six degrees of freedom are considered, including the translational along and rotational motions about the X, Y, and Z axes.

- **Symmetrical, unaccelerated flight:** This model is only trimmed for symmetrical unaccelerated flight. As a result, the rotational velocities do not increment the angles of attack and sideslip. Without this assumption, for example, the pitching moment increases the angle of attack at the nose and decreases it at the tail Durham (2013).
- **Non-interacting Control Surfaces:** This assumptions now extends to the interaction with the rudder and ailerons.
- **Simplified Wing-Tail Interaction:** The distortion of the air mass at the vertical tail (rudder and vertical stabilizer) is neglected entirely.

6.2. Estimating Forces

The resultant forces from the wing and the thrust forces from the main rotors are separated into left and right to account for the possibility of differential thrust and aileron deflection. This differential also affects the wings through the slipstream effect. The slipstream from the main rotors and the downwash from both sides of the wing are averaged when considering the effective angle of attack and dynamic pressure on the horizontal stabilizer.

6.2.1. Thrust

The thrust terms are separated between the left and right main rotor thrust outputs to allow for differential thrust capability. The assumptions discussed in Section 4.2.1 still hold for the methods used in this Chapter. Some additional assumptions are made:

- **Simplified Slipstream Models:** The induced flow from the right and left main rotor is assumed to be combined and average at the horizontal tail and negligible at the vertical tail.
- **Symmetrical Rotor Torques and Rates:** The main rotors are assumed to have similar and opposing torques and rotational rates.
- **Propeller Drag:** The tail rotor drag is assumed to be contained within the empennage estimated drag and the main rotors drag by the wing drag force.

One of the consequences of the way the main rotors are modeled is that there is no possibility of a single engine failure in this model. In fact, the CL-84 rotors were both connected to both engines to avoid the case of a single engine failure, as explained by Michaelsen (1971). The case of partial engine failure was thus avoided in the design of the CL-84.

6.2.2. Aileron

The aileron control input is modelled as a difference in flap deflection between the right and left flaperons. This differential aileron control input deviates both left and right flap movements from the schedule set to the wing tilt angle, incrementing the flap deflection angle by $\pm\delta_a$.

6.2.3. Vertical Tail

In a similar fashion to Section 4.2.3, the vertical tail was assumed to be equipped with a NACA0012 airfoil, with the same approximation for its lift, drag, and moments coefficients described by Equation 4.26.

6.3. Equations of Motion

To avoid complicated notation, all forces and moments are assumed to be in the body-fixed reference frame defined in Appendix D unless stated otherwise. The equations of motion are once again unpacked from the general form presented in Equation 6.1, which are the same as Durham (2013)'s equations with adapted notation.

$$\begin{aligned} m\frac{d}{dt}(\boldsymbol{V}) + \boldsymbol{\Omega} \times m\boldsymbol{V} &= \boldsymbol{\Sigma F} \\ \boldsymbol{I}\frac{d}{dt}(\boldsymbol{\Omega}) + \boldsymbol{\Omega} \times \boldsymbol{I\Omega} &= \Sigma \boldsymbol{M} \end{aligned} \tag{6.1}$$

For convenience, the forces and moments are separated for each axis by their origin: propulsive, aerodynamic, or control surface deflection. To determine the sign of each term, and the composition of the moments and forces in each summation, Figure 6.1, Figure 6.2, and Figure 6.3 are used extensively.

$$\begin{aligned} m\dot{u} &= X_P + X_W + X_f + X_{HT} + X_{\delta_e} - Wsin(\theta) - qw + rv \\ m\dot{v} &= Y_f + Y_{VT} + Wcos(\theta)sin(\phi) + pw - ru \\ m\dot{w} &= Z_P + Z_W + Z_f + Z_{HT} + Z_{\delta_e} + Wcos(\theta) + qu - pv \end{aligned} \tag{6.2}$$

$$\begin{aligned} I_D &= I_{xx}I_{zz} - I_{xz}^2 \\ \dot{p} &= \frac{I_{zz}}{I_D}\left[L_{P,W,VT} + I_{xz}pq - qr(I_{zz} - I_{yy})\right] + \frac{I_{xz}}{I_D}\left[N_{P,W,VT} - I_{xz}qr - pq(I_{yy} - I_{xx})\right] \\ \dot{q} &= \frac{1}{I_{yy}}\left[M_{P,W,HT} - pr(I_{xx} - I_{zz}) - I_{xz}(p^2 - r^2)\right] \\ \dot{r} &= \frac{I_{xz}}{I_D}\left[L_{P,W,VT} + I_{xz}pq - qr(I_{zz} - I_{yy})\right] + \frac{I_{xx}}{I_D}\left[N_{P,W,VT} - I_{xz}qr - pq(I_{yy} - I_{xx})\right] \end{aligned} \tag{6.3}$$

$$\begin{aligned} X_P &= (T_{m,L} + T_{m,R})cos(\eta) \\ X_W &= -L_{W,L}sin(\zeta_L - \alpha) - L_{W,R}sin(\zeta_R - \alpha) - D_{W,L}cos(\zeta_L - \alpha) - D_{W,R}cos(\zeta_R - \alpha) \\ X_f &= -D_f cos(\alpha) + L_f sin(\alpha) \\ X_{HT} &= -(L_{HT} + L_{\delta_e})sin(\bar{\varepsilon} - \alpha_{HT}) - (D_{HT} + D_{\delta_e})cos(\bar{\varepsilon} - \alpha_{HT}) \\ X_{\delta_e} &= -L_{\delta_e}sin(\bar{\varepsilon} - \alpha_{HT}) - D_{\delta_e}cos(\bar{\varepsilon} - \alpha_{HT}) \end{aligned} \tag{6.4}$$

$$\begin{aligned} Y_f &= L_f cos(\beta) \\ Y_{VT} &= (F_{VS} + F_{\delta_r})cos(\beta) \end{aligned} \tag{6.5}$$

$$\begin{aligned} Z_P &= -(T_{m,L} + T_{m,R})sin(\eta) - T_t \\ Z_W &= -L_{W,L}cos(\zeta_L - \alpha) - L_{W,R}cos(\zeta_R - \alpha) + D_{W,L}sin(\zeta_L - \alpha) + D_{W,R}sin(\zeta_R - \alpha) \\ Z_f &= -D_f sin(\alpha) - L_f cos(\alpha) \\ Z_{HT} &= D_{HT}sin(\bar{\varepsilon} - \alpha_{HT}) - L_{HT}cos(\bar{\varepsilon} - \alpha_{HT}) \\ Z_{\delta_e} &= D_{\delta_e}sin(\bar{\varepsilon} - \alpha_{HT}) - L_{\delta_e}cos(\bar{\varepsilon} - \alpha_{HT}) \end{aligned} \tag{6.6}$$

$$\begin{aligned} L_P &= (T_{m,L} - T_{m,R})sin(\eta)y_{prop} \\ L_W &= \left(-L_{W,L}cos(\zeta_L - \alpha) + L_{W,R}cos(\zeta_R - \alpha) - D_{W,L}sin(\zeta_L - \alpha) + D_{W,R}sin(\zeta_R - \alpha)\right)y_W \\ L_{VT} &= \left(L_{VS} + L_r\right)cos(\beta)z_{VT} \end{aligned} \tag{6.7}$$

$$\begin{aligned} M_P &= (T_{m,L} + T_{m,R})sin(\eta)x_{prop} - (T_{m,L} + T_{m,R})cos(\eta)z_{prop} - T_t x_{T-prop} \\ M_W &= -Z_W x_W - X_W z_W + M_{AC_{W,L}} + M_{AC_{W,R}} \\ M_{HT} &= -X_{HT}z_{HT} + Z_{HT}x_{HT} + M_{AC_{HT}} - X_{\delta_e}z_{\delta_e} + Z_{\delta_e}x_{\delta_e} + M_{AC_{\delta_e}} \end{aligned} \tag{6.8}$$

$$\begin{aligned} N_P &= (T_{m,L} - T_{m,R})cos(\eta)y_{prop} \\ N_W &= \left(-L_{W,L}sin(\zeta_L - \alpha) + L_{W,R}sin(\zeta_R - \alpha) - D_{W,L}cos(\zeta_L - \alpha) + D_{W,R}cos(\zeta_R - \alpha)\right)y_W \\ N_{VT} &= \left(L_{VS} + L_r\right)cos(\beta)x_{VT} \end{aligned} \tag{6.9}$$

6.3.1. Trim

For the purpose of trimming the model, the aircraft is assumed to be in equilibrium flight, meaning that all accelerations and rotations are set to zero. As a result, the moments of inertia have no bearing on the trimming output of the model. Also, since the model is only trimmed in symmetrical flight, the kinematic equations are made trivial by $\phi = 0$ and $\psi = 0$.

To allow verification and validation, the trim flight conditions presented are identical to the ones fed to the three degree of freedom model. In this case, there are three additional equations and three additional control variable. The input vector remains [η, u], with a specified continuous mission. The vertical and lateral velocity components, w and v, as well as the roll angle ϕ and heading angle ψ are set to zero. The solved parameters are therefore [$T_{m,L}$, $T_{m,R}$, T_t, δ_e, δ_a, δ_r, θ]. The trim problem of this over-actuated system becomes identical to the problem solved in Section 4.3.1. The trim corridor found for the extended model is shown in Figure 6.4, with the blue shaded area representing the flight envelope for which the model finds a possible and plausible trim solution. The red line is the continuous mission profile used to verify that the model can be resolved for a smooth transition. Several points of interest were also trimmed for to explore the behaviour of the model. These are indicated at $\eta = 85$, $\eta = 80$, $\eta = 41$, $\eta = 28$, $\eta = 14$, and $\eta = 0$.

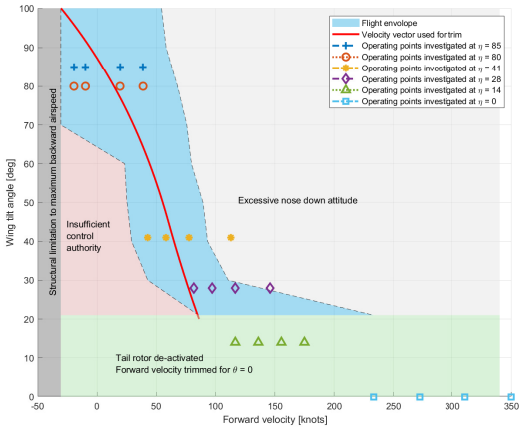

Figure 6.4: Transition corridor for the CL-84 longitudinal model

All trim solutions shown in Figure 6.4 were trimmed with the elevator deflection angle set to $-1\alpha_{HS}$. After comparison with $\delta_e = -2\alpha_{HS}$, it is found that $\delta_e = -1\alpha_{HS}$ provides reduced control actuation for a similar trim corridor. Indeed, a comparison between Figure 6.4 and Figure 4.16 shows that below 40° of wing tilt, the blue region shifts to the right a little bit. This outcome also suggests that an optimisation algorithm that allows for more variable elevator deflection could produced a wider transition corridor. As such, the detailed logic used for trimming the six degree of freedom model can be found in Appendix A.

7

Verification & Validation

This section presents the output of the model with lateral-directional extension for the same trim conditions as in Chapter 5. First, the behaviour of the model during the transition is examined in Section 7.1. Then, Section 7.2 shows the results of the same validation tests as performed with the longitudinal model.

7.1. Transition Corridor

Once again the continuous mission profile provided as input to the trimming algorithm is shown in Figure 5.1. For this input vector, two elevator settings were tests to provide insight into the impact of the elevator setting on the trim output. The resulting elevator deflection are shown in Figure 7.2 and Figure 7.1. The wing tilt angle is indicated on these figures to ease comparison.

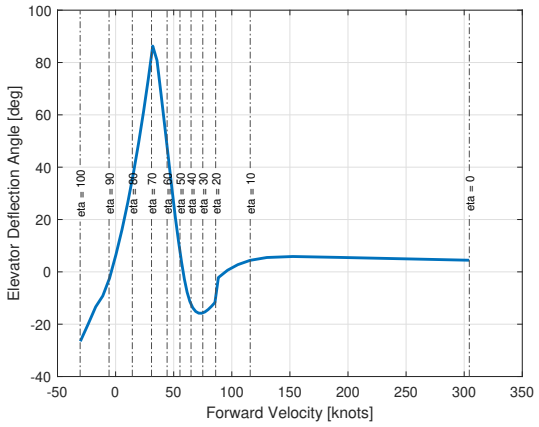

Figure 7.1: Elevator deflection set to $-2\alpha_{HS}$

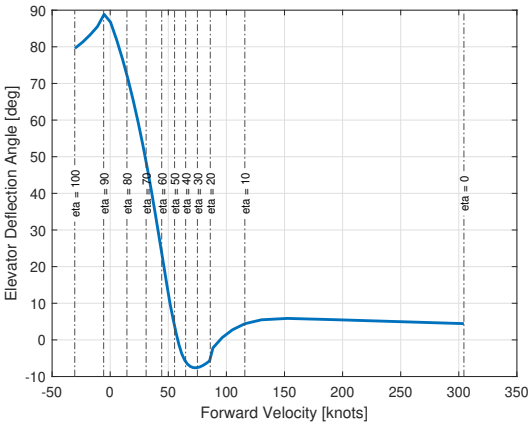

Figure 7.2: Elevator deflection set to $-1\alpha_{HS}$

Once again, below $20°$ of wing tilt, the trim algorithm solves for elevator deflection δ_e instead of tail rotor thrust T_t. At first sight, the shape of the elevator deflection curve seem similar, with a peak close to $90°$ deflection and then a trough before algorithm changes. The trough location does not change significantly and remains near $30°$ of wing tilt, but the magnitude decreases by close to $10°$. Meanwhile, the location of the peak changes. When the rule is $-2\alpha_{HS}$, the peak is around $\eta = 70°$, compared to $\eta = 90°$ for the $-1\alpha_{HS}$ rule. This is significant because the tail is much less effective around hover, meaning that such a large deflection is a bi-product of the trim, rather than necessary for it. In other words, the deflection is only large at this flight configuration because the angle of attack on the tail is large, not because the elevator deflection is necessary to maintain controlled flight.

The effect of changing the elevator scheduling method can be observed on the fuselage pitch angle using Figure 7.3 and Figure 7.4. The most notable difference is that around $70°$ of wing tilt, the aircraft needs to compensated for a lesser tail force by pitch up $2°$ more.

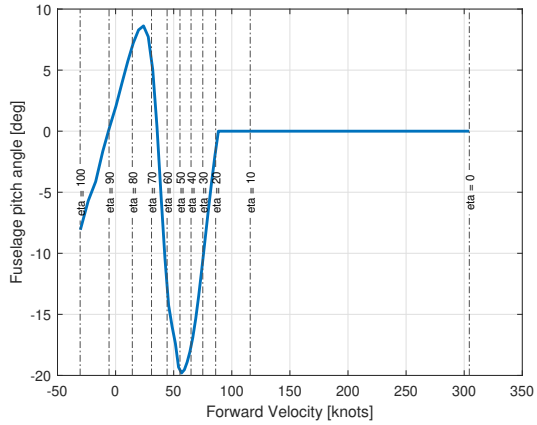

Figure 7.3: Fuselage pitch attitude when $\delta_e = -2\alpha_{HS}$

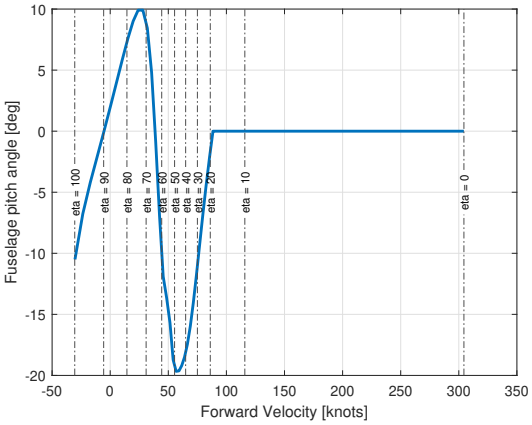

Figure 7.4: Fuselage pitch attitude when $\delta_e = -1\alpha_{HS}$

Also, the thrust required for trimmed flight is compared in Figure 7.5 and Figure 7.6. Again, the results look similar at first glance. However, several difference favor the $\delta_e = -1\alpha_{HS}$ rule. First, the hover and backward flight power curve is much smoother, and the peak in power required at $70°$ of wing tilt is slightly lower. Also, the transition in the algorithm logic at $20°$ is smoother as well. This can be readily explained by comparatively smooth transition in elevator deflection angle δ_e at the transition, as shown in Figure 7.2.

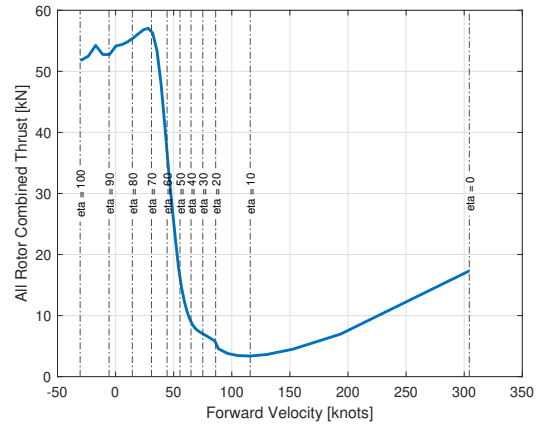

Figure 7.5: Trimmed total thrust when $\delta_e = -2\alpha_{HS}$

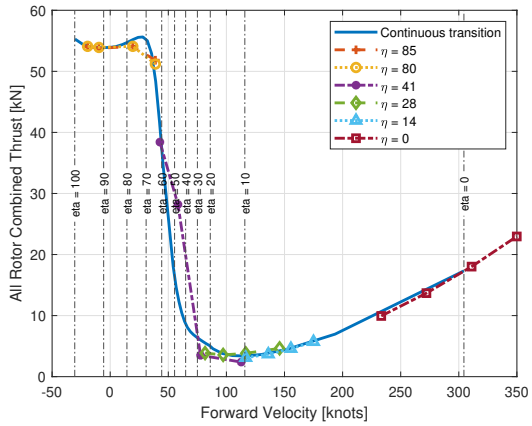

Figure 7.6: Trimmed total thrust when $\delta_e = -1\alpha_{HS}$

As a result of the comparison between the elevator scheduling rules, the $-1\alpha_{HS}$ was chosen for further investigation at several key wing tilt angles. The chosen angles were close to the ones for which validation data was available, at $85°$, $80°$, $41°$, $28°$, $14°$, and $0°$. For each value η, four airspeeds were investigated. The trim thrust output are also shown in Figure 7.6 and it seems that the thrust depends almost exclusively on the airspeed, and not on the wing tilt angle.

Figure 7.7 demonstrates the impact of changing the wing tilt angle η on the fuselage pitch attitude θ. Indeed, the $\eta = 85$ and $\eta = 80$ configurations show that, for the same airspeed, the angle of wing tilt can be compensated for by pitching the entire aircraft. Another revealing aspect of this figure is that although the airspeed variation were approximately the same for all wing tilt angles, these resulted in drastically different effects on the fuselage pitch. For instance, at $\eta = 41$, the fuselage pitch is much more affected by changes in airspeed than at any other wing incidence. In particular, when the wings are in cruise configuration, the fuselage is predictably not much affected by changes in airspeed. Finally, it is important to note that for this elevator schedule, a level fuselage pitch attitude cannot be maintained throughout the transition. To

accomplish that, it would be necessary to adapt the elevator deflection angle in a more flexible way, such as through the use of optimization algorithms.

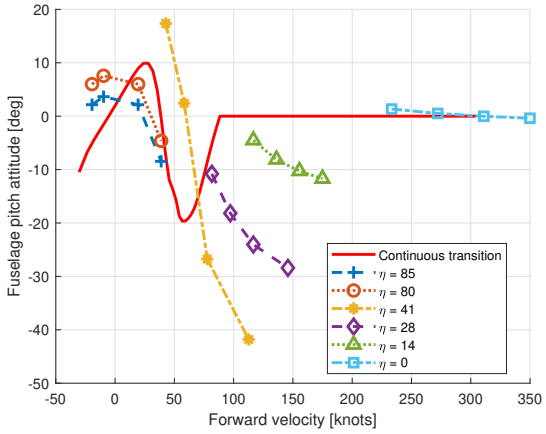

Figure 7.7: Fuselage trim pitch attitude

As for the other pilot control inputs, both the rudder and aileron deflections were kept to zero, due to the symmetrical nature of the trim corridor provided. The thrust control could be broken down into components, similar to how the longitudinal model was analysed. In this regard, the tendencies found in Chapter 5 remained valid. The main rotor induced velocity is shown in Figure 7.8, including the additional operating points. The main rotors' induced velocity confirm the relationship established in Chapter 5 that $\lambda_i \propto \frac{T}{u}$. This relationship is perhaps a little less immediately evident in Figure 7.9. This is because the tail rotor is responsible for pitch control, and the fuselage pitch changes significantly with airspeed. Consequently, the tail rotor trim thrust also changes significantly with changes in airspeed.

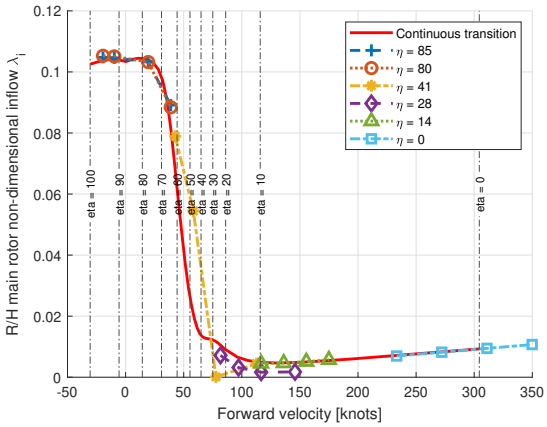

Figure 7.8: R/H main rotor induced velocity λ_i

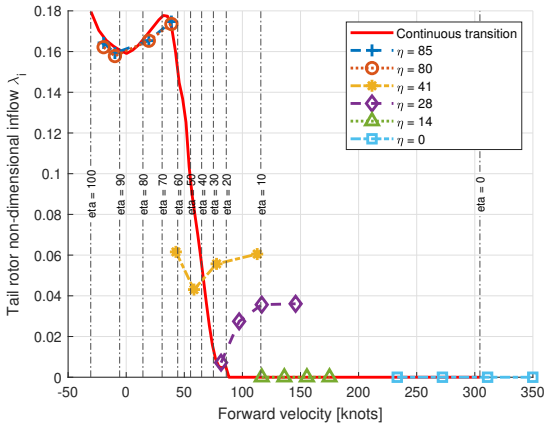

Figure 7.9: Tail rotor induced velocity λ_i

As for the propeller collective pitch, Figure 7.10 and Figure 7.11 demonstrate the model output. As discussed in Chapter 5, the collective propeller blade angle is closely linked to $\frac{T}{1+u^2}$ at low angles of wing tilt and then to $T \cdot u$ at smaller angles of wing tilt. The same tendency is true of the tail rotor, though it is once again hidden by its relationship to the fuselage pitch attitude.

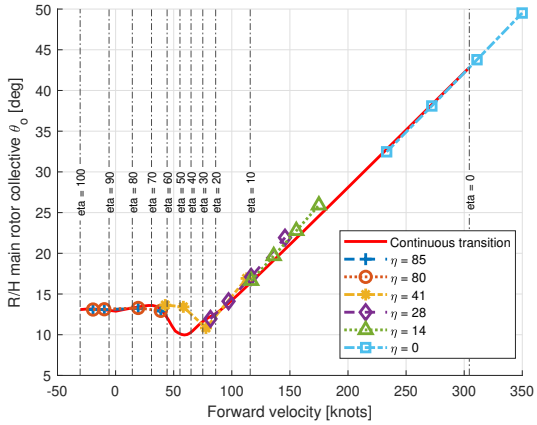

Figure 7.10: R/H main rotor propeller pitch angle

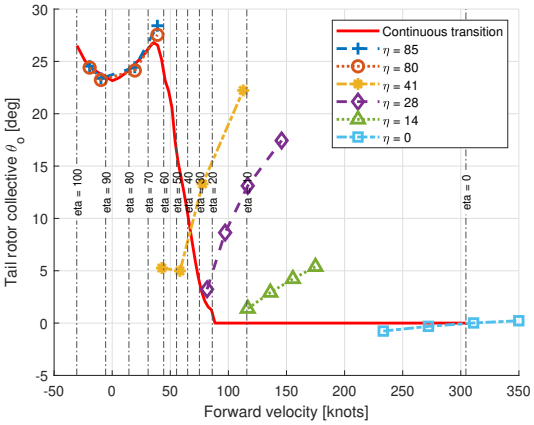

Figure 7.11: Tail rotor propeller pitch angle

Finally, when the tail rotor is deactivated, $T_t = 0$, and the induced flow follows such that $\lambda_{i_t} = 0$, the propeller collective blade angle then only depends on λ_{c_t}. This phenomenon comes from the $-(\lambda_c + \lambda_i)$ term from the BEM equation, Equation 4.1. Whereas the CL-84 folded this rotor in regions when it isn't used to prevent unnecessary drag, this model does not consider the propeller drag.

7.2. Validation

The output of the six degree of freedom model, unsurprisingly, closely matches that of the three degree of freedom model. To verify that this is the case for all validation tests from Chapter 5, the six degree of freedom model is also compared to these data. The results are presented in Figure 7.12 thru to Figure 7.15.

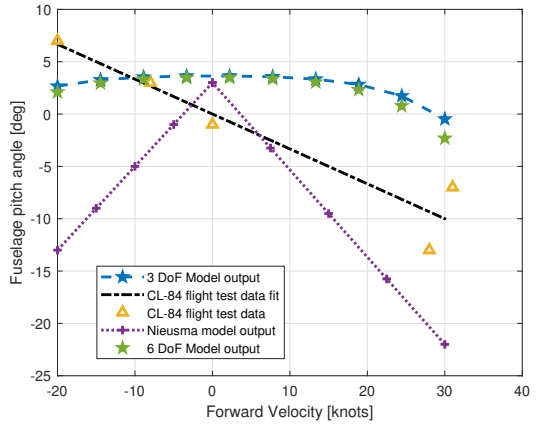

Figure 7.12: Variations in velocity at 85.1°wing tilt compared to flight test data (Nieusma, 1993)

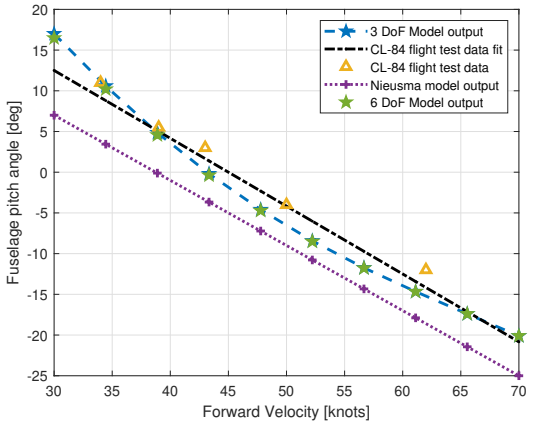

Figure 7.13: Variations in velocity at 41.5°wing tilt compared to flight test data (Nieusma, 1993)

The validation tests were reproduced with the same input data as the longitudinal model. Since the longitudinal behaviour of the six degree of freedom model is adopted from the longitudinal model, the validation data also closely matches.

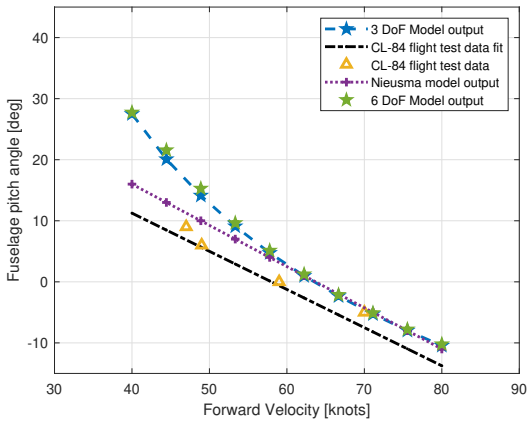

Figure 7.14: Variations in velocity at 28.6°wing tilt compared to flight test data (Nieusma, 1993)

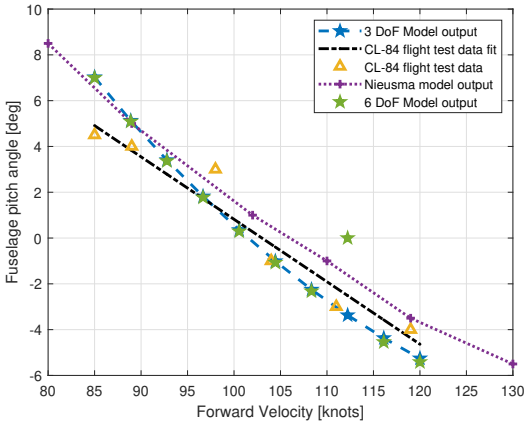

Figure 7.15: Variations in velocity at 14°wing tilt compared to flight test data (Nieusma, 1993)

Part V

Linear State Space Model

8

Linearizing and Stability Analysis

This chapter explores the stability characteristics of the model. The initial reaction to stimulus is also known as static stability. To exhibit positive static stability, the aircraft must react by correcting for disturbances and returning to its initial trim conditions. An aircraft with negative static stability steers further away from its initial conditions when disturbed. The dynamic behaviour refers to the subsequent pattern of behaviour. Dynamic oscillatory modes can result when a system over-corrects an initial disturbance, amplifying its effects. In this case, it is important to understand whether the aircraft's motion will converge to the initial condition or not. If it does, then it is considered to have positive dynamic stability, and negative if the motion naturally does not converge (Durham, 2013). First, the static stability is discussed in Section 8.1, then the dynamic behaviour is examined through the linearization of the model in Section 8.2.

8.1. Static Stability

The static stability of an aircraft is defined by its tendency to return to a trim point after disturbances. The static stability tendency in the tilt wing CL-84, as modeled in this report, is investigated at the operating points selected shown in Figure 6.4. To gain insight into the static stability of the model, it was trimmed for each given pair [η, u] then numerically disturbed. Only key stability characteristics are investigated within the scope of this report. C_{l_v} and C_{n_v} provide insight into the lateral and directional characteristics, while C_{m_u} an C_{m_w} describe the longitudinal behaviour. Although C_{m_α} is more commonly used in fixed-wing flight dynamics (for example in Durham (2013)), C_{m_w} is more useful for describing helicopter dynamics due to the way α is defined. In an effort to facilitate comparison with other aircraft, the stability derivatives are presented in their dimensionless form. They were non-dimensionalized in accordance with convention proposed by H.H.B.M.Thomas (1977), using the moment derivative with respect to velocity divisor. As a result, the longitudinal moments derivatives are divided by $\frac{1}{2}\rho V_\infty S\bar{c}$ and the lateral-directional ones by $\frac{1}{2}\rho V_\infty Sl$.

To interpret the stability derivatives related to static stability, the sign conventions used in the model development take on some importance. It is noted here that a positive increase in u indicates the aircraft gains velocity forward, a positive increase in v indicates the aircraft gains velocity toward its right wing, and a positive increment in w results in motion of the aircraft downward, toward its belly. In all cases considered this also means a movement toward the ground, but the distinction is important because the body axis is not always aligned with the NED axis. Further details on the coordinate systems are provided in Appendix D. Similarly, the pitching moment M is defined positive when the nose pitches up, the rolling moment L is defined positive when the right wing lowers and the yawing moment N is positive when the nose turns toward the right wing. Although there is no verification data available for the CL-84's stability derivatives, the results from this section still offer important insights.

First, the speed stability derivative C_{m_u} is shown in Figure 8.1 and Figure 8.2. It is positive for all wing tilt angle configurations, which means that the aircraft reacts to a disturbance that causes a positive increment in forward velocity by pitching up. Indeed, this is a stabilizing reaction because pitching up without changing other settings (such as power settings) reduces forward velocity by redirecting it and shedding kinetic energy. This derivative therefore supports the claim that the aircraft is statically stable.

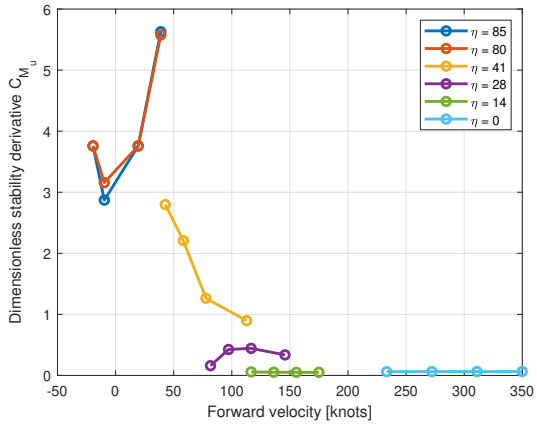

Figure 8.1: Stability derivative C_{m_u}

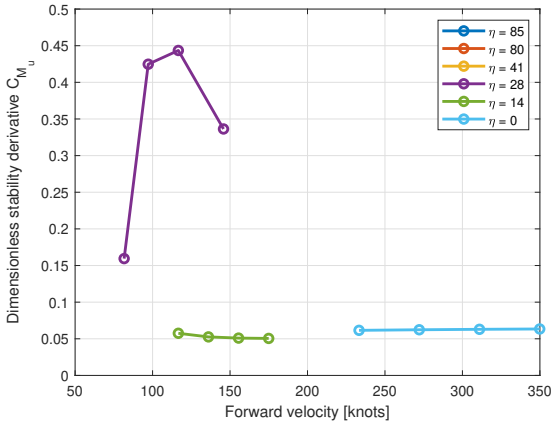

Figure 8.2: Close-up of Figure 8.1

However, this stability indicator reveals some strange behaviour: the aircraft is extremely stable in hover and high wing tilt angle configurations. Compared to the stability derivatives for the MBB-Bo105 helicopter, obtained by Pavel (1996), the values shown in Figure 8.1 are very large. Whereas typical values are below 1, the maximum value for C_{m_u} obtained here is close to 6. This can be attributed to the drag on the wings acting as a large source of damping against any movement along the body x-axis. By contrast, a comparison to the work of G.Steinbusch (2021) on tilt-rotors suggest that in the wings level configuration, the speed stability derivative values match what can be reasonably expected.

The incidence stability derivative C_{m_w} behaves somewhat similarly to the speed stability derivative, but with even more exaggerated tendencies. Figure 8.3 shows the derivative for several flight conditions. For mid-low angles of wing incidence, Figure 8.4 offers a detailed view.

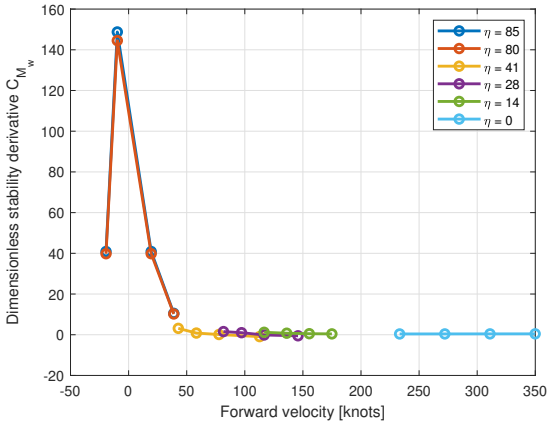

Figure 8.3: Stability derivative C_{m_w}

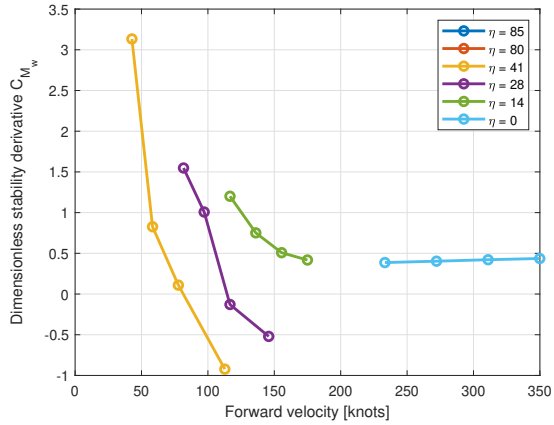

Figure 8.4: Close-up of Figure 8.3

Near and at cruising configuration, the value of the derivative is in the same order of magnitude as G.Steinbusch (2021)'s tilt rotor model and Pavel (1996)'s helicopter model. However, the value of this derivative around hover is very large, ranging from 40 to 150. This excessive value is explained by observing the behaviour of the horizontal tail. When broken down into components, the stabilizer contributions are overwhelming. For $\eta = 80°$, the contribution at each velocity tested, from slow to fast, is 89%, 93%, 89%, and 74%. The slipstream contributes to a very large negative angle on the horizontal stabilizer at low speeds. Assuming perfect hover with the wing at $90°$, the horizontal stabilizer angle of attack is entirely defined by the slipstream, resulting in $\alpha_{HS} = -90°$. Looking back to Figure 4.15, this means the lift coefficient of the tail for an equivalent angle of attack of $270°$ is approximately zero. Then, when the w increases, bringing the angle of attack closer to zero, the horizontal stabilizer's lift coefficient

goes for into the negative region. In this configuration, the wing chord is aligned with the aerodynamic perturbation, so it is not as greatly affected as the tail.

To gain better insight into the unstable behaviour at low wing tilt angles, a closer look needs to be taken into the contributing factors. This breakdown can be seen in Figure 8.5 for the flight condition at $\eta = 41$ and in Figure 8.6 for the flight condition at $\eta = 28$.

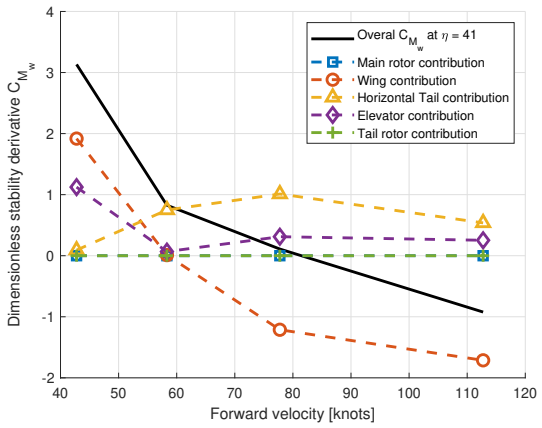

Figure 8.5: Breakdown of components of C_{m_w} at $\eta = 41°$

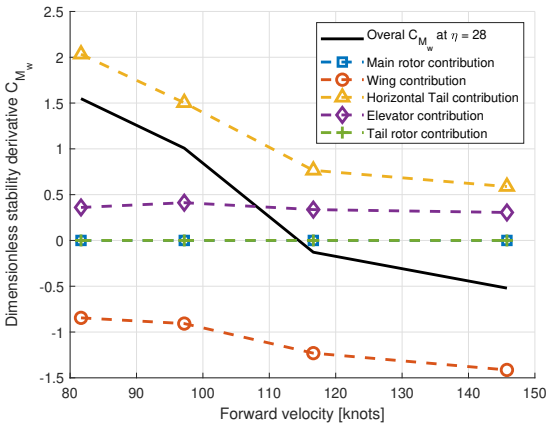

Figure 8.6: Breakdown of components of C_{m_w} at $\eta = 28°$

For both flight conditions, the factor responsible for unstable behaviour is easily identified as the wing. In both cases, when at larger forward airspeeds, the moment generated by the wing becomes destabilizing. As shown in Appendix C, the wing aerodynamic center and center of mass are both above and ahead of the overall center of gravity, even with large negative fuselage pitch angle θ, so it is implausible that the wings are causing negative pitching moments. Therefore, the likely explanation is that the pitching moment generated by the wings reduces as a response to a positive increment in vertical velocity w, which is downward flight. A positive increment in w will increase the angle of attack on the wing, and possible bring the wing past the stall region. Considering that without vertical velocity the rotor slipstream brings the resultant angle of attack on the wing above the body X-axis, at larger horizontal velocities u the increment in w is more likely to bring the the angle of attack on the wings toward the stall region. However, the initial operating point is trimmed for a specified elevator setting, which is not changed when the perturbation is applied, such that these stability derivatives depend on the elevator deflection. A different approach to determining the elevator deflection might yield more stable results.

Two important sideslip stability derivatives are explored in Figure 8.7 and Figure 8.8.

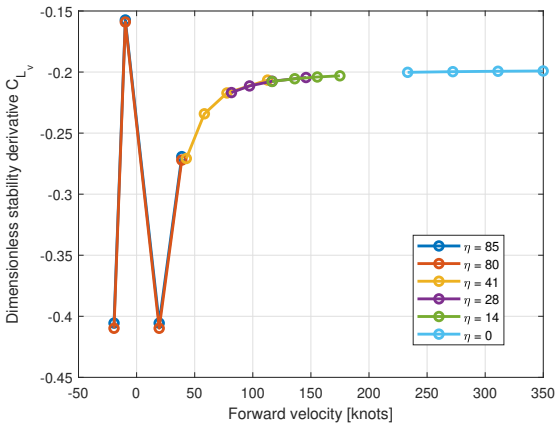

Figure 8.7: Stability derivative C_{l_v}

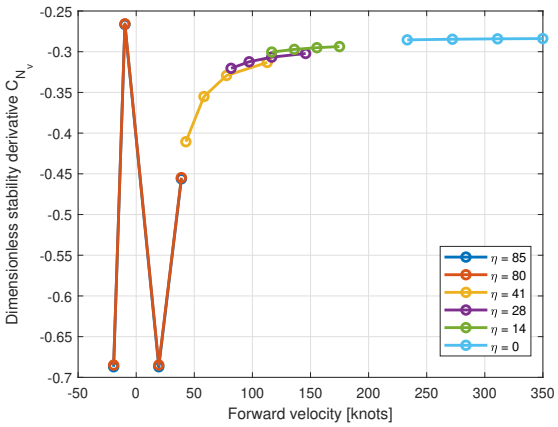

Figure 8.8: Stability derivative C_{n_v}

The dihedral stability derivative, C_{l_v}, is negative throughout the transition. This is desirable because it means that when the aircraft gains airspeed v toward the right wing it produces a negative rolling moment, lifting the right wing and initiating a turn to the left. Similarly, the weathercock derivative, C_{n_v}, is also negative throughout the transition. This can be interpreted as a negative yawing moment response to an increase in lateral speed v. In other words, the nose of the aircraft will turn toward the left wing when the aircraft gains speed toward the right wing, thus providing desirable corrective action.

Although both sideslip derivatives are stable and in a range of values comparable to the values obtained for helicopters by Pavel (1996)'s model, the tendency around hover is worth mentioning. Indeed, there seems to be a large resistance to lateral disturbance around hover, though not at hover. This can be explained by the fact that the wings are vertically deployed in this configuration, and with a bit of airspeed the drag vector from the sidelip angle β will amplify the resisting tendency. At values of β close to $90°$ or around hover, the inbound velocity slide along the edge of the wing without creating a large drag force.

8.2. Linearization

To best analyse the dynamic behaviour of the aircraft, it is easiest to formulate a linear models. Unlike the non-linear models developed in Chapter 4 and Chapter 6, linear models must be built about a specified operating point. For this reason, this Chapter presents a set of models at various operating points deemed of interest. First, some theory about linearization is introduced in Section 8.2 and Section 8.2.1. Then the linear models are analysed in Section 8.2.2 with some interpretation on the implications for the flight dynamics. An important clarification in the notation for this chapter is that the control input vector, $\boldsymbol{u}$, is written in bold to distinguish it from the forward velocity, u, which is a scalar state.

Classical methods of control require a linear mechanics model because they permit analysis in the frequency domain in addition to time domain performance. Linear models can be expressed as state space matrices or input-to-output transfer functions, and then analysed using pole location or frequency characteristics such as gain and phase. The frequency analysis offers crucial information about the stability and robustness of a systems, and provide insight into the excitation frequencies. This domain also paves the way for many control techniques such as pole placement, H_∞ loop shaping, LQR/LRT. Although there exist control tools to work on non-linear models as well, such as non-linear dynamic inversion or backstepping, these are still considered experimental and their path to certification remains unclear. Therefore, in an effort to offer a more useful contribution to understanding tilt-wing flight dynamics, this report also needs to present linear models.

A non-linear model can be linearized analytically or numerically. However, since this report aims to derive an analytical flight mechanics model, the numerical methods for linearization will not be discussed. In literature (Durham, 2013), linearization is performed by evaluating a Jacobian matrix at an operating point. To obtain a Jacobian matrix, first a set of vectors are defined to represent some key variable parameters of the system. These vectors are the state time derivatives, $\dot{\boldsymbol{x}}$, the state derivatives, $\boldsymbol{x}$, and the system control inputs, $\boldsymbol{u}$. If there are *n* state variables and *m* control variables, then the vectors $\dot{\boldsymbol{x}}$ and $\boldsymbol{x}$ contain *n* elements each and $\boldsymbol{u}$ contains *m* elements. There will also be *n* relationships between the state derivatives, the states, and control inputs, which can be written as a set of n functions $\boldsymbol{f}(\dot{\boldsymbol{x}}, \boldsymbol{x}, \boldsymbol{u})$. The next step to determine the Jacobian matrix is to formulate a Taylor series expansion of the functions $\boldsymbol{f}(\dot{\boldsymbol{x}}, \boldsymbol{x}, \boldsymbol{u})$ in the form of Equation 8.1 and evaluate it at the operating point.

$$\boldsymbol{f}(\dot{\boldsymbol{x}}, \boldsymbol{x}, \boldsymbol{u}) = \boldsymbol{f}(Ref) + \left.\frac{\partial \boldsymbol{f}}{\partial \dot{\boldsymbol{x}}}\right|_{Ref} \Delta\dot{\boldsymbol{x}} + \left.\frac{\partial \boldsymbol{f}}{\partial \boldsymbol{x}}\right|_{Ref} \Delta\boldsymbol{x} + \left.\frac{\partial \boldsymbol{f}}{\partial \boldsymbol{u}}\right|_{Ref} \Delta\boldsymbol{u} + H.O.T \tag{8.1}$$

In the pursuit of linearization of a flight mechanics model, the higher order terms (H.O.T) of the Taylor series are typically ignored (Durham, 2013). Also, when the series is evaluated at an operating point known to result in a trimmed flight conditions, the first term, $\boldsymbol{f}(Ref)$, will be zero by definition. Since $\boldsymbol{f}(\dot{\boldsymbol{x}}, \boldsymbol{x}, \boldsymbol{u})$ is a vector of functions, Equation 8.1 produces a matrix. The part of this matrix that contains the partial derivatives is known as the Jacobian matrix. This matrix can also be written in the form shown by Equation 8.2.

$$\frac{\partial \boldsymbol{f}}{\partial \boldsymbol{vars}} \equiv \begin{bmatrix} \frac{\partial f_1}{\partial var_1} & \frac{\partial f_1}{\partial var_2} & \dots & \frac{\partial f_1}{\partial var_{n+m}} \\ \frac{\partial f_2}{\partial var_1} & \frac{\partial f_2}{\partial var_2} & \dots & \frac{\partial f_2}{\partial var_{n+m}} \\ \vdots & \vdots & \ddots & \vdots \\ \frac{\partial f_n}{\partial var_1} & \frac{\partial f_n}{\partial var_2} & \dots & \frac{\partial f_n}{\partial var_{n+m}} \end{bmatrix} \tag{8.2}$$

A useful way to represent the Taylor series expansion from Equation 8.1 splits the matrix of partial derivatives into three.

$$\Delta \dot{\boldsymbol{x}} = \left[\frac{\partial \boldsymbol{f}}{\partial \dot{\boldsymbol{x}}}\right]^{-1}_{Ref} \left[\left[\frac{\partial \boldsymbol{f}}{\partial \boldsymbol{x}}\right]_{Ref} \Delta \boldsymbol{x} + \left[\frac{\partial \boldsymbol{f}}{\partial \boldsymbol{u}}\right]_{Ref} \Delta \boldsymbol{u}\right] \tag{8.3}$$

$$\Delta \dot{\boldsymbol{x}} = A\Delta \boldsymbol{x} + B\Delta \boldsymbol{u}$$

The representation achieved in Equation 8.3 is known as the state space representation. These resulting A and B matrices, with sizes $n \times n$ and $n \times m$ respectively, are a linear approximation of the full dynamics, valid around the operating point condition. The pair of matrices offer information about two key areas of interest: modal dynamics and dynamic stabilizability.

8.2.1. Modal Sensitivity Analysis

The chief contributions of various flight dynamic modes can be identified via mode sensitivity analysis. The procedure according to Durham (2013) is outlined in this section. It is assumed that the flight dynamics model has been linearized into state space form with an A matrix of size $n \times n$ and full rank. In that case there exists a matrix M called the modal matrix that contains the eigenvectors of the A matrix such that $M \equiv [\boldsymbol{v_1}\ \boldsymbol{v_2}\ \dots\ \boldsymbol{v_n}]$. The eigenvectors are vectors that fulfill the condition $A * \boldsymbol{v_i} = \boldsymbol{v_i} * \lambda_i$ for each eigenvalue λ_i. For an A matrix of full rank with n distinct eigenvalues, then the eigenvectors are also linearly independent and $|M| \neq 0$. Therefore, M^-1 exists. The rows of M and columns of M^-1 can be denoted as $r_1, r_2, \dots$ and $c_1, c_2, \dots$ respectively as shown below.

$$M = \begin{bmatrix} r_1 \\ r_2 \\ \vdots \\ r_n \end{bmatrix}, M^-1 = \begin{bmatrix} c_1 & c_2 & \dots & c_n \end{bmatrix}$$

Then, the columns of M^-1 are reshaped into n diagonal matrices of size $n \times n$, C_i.

$$c_i = \begin{bmatrix} c_{i_1} \\ c_{i_2} \\ \vdots \\ c_{i_n} \end{bmatrix}, C_i = \begin{bmatrix} c_{i_1} & 0 & 0 & \dots & 0 \\ 0 & c_{i_2} & 0 & \dots & 0 \\ \vdots & & \ddots & & \vdots \\ 0 & 0 & 0 & \dots & c_{i_n} \end{bmatrix}$$

Finally, an $n \times n$ sensitivity matrix, S can be constructed.

$$S = \begin{bmatrix} r_1 C_1 \\ r_2 C_2 \\ \vdots \\ r_n C_n \end{bmatrix}$$

The final step is to normalize the entries of S by taking the magnitude of each value and dividing it by the sum of the magnitudes of the entry in that row. Each row of S corresponds to a state and each column to an eigenmode. The entries represent the percentage contribution of the state to the eigenmode dynamic. According to Durham (2013), states with contributions lesser than 10% of the largest contributor can be safely ignored.

8.2.2. Results

Before linearizing the six degree of freedom model, some simplifications that were justified in trim need to be reconsidered. For trimming, all rotational velocities were considered to be zero and their effects were also neglected. During trimmed flight, all accelerations are considered to be 0. As a consequence, the couplings between the rotations and the angles of attack and sideslip were neglected, and no consideration was made for the moments of inertia. However, for linearization purposes the effect rotations must be accounted, which means adjusting the model to include couplings and estimates of the moments of inertia.

Rotational couplings

As for the couplings between the rotations and the angles of attack and sideslip, Durham (2013) shows that when the aircraft pitches, rolls, or yaws, the extremities experience a difference in vertical velocities and therefore a difference in effective angle of attack. To account for this effect, the angles of attack and sideslip are adjusted according to Nguyen and Tuzcu (2009). On page 8, Nguyen and Tuzcu (2009) defines the local angle of attack of a rigid body aircraft, α^*, rewritten as Equation 8.4 to accommodate the notation and simplifications (no sweep nor dihedral on the wing) used in this report.

$$\alpha^* = \alpha - \frac{-q \cdot x_i + p \cdot y_i - \alpha \cdot q \cdot z_i}{u} \tag{8.4}$$

$$= \frac{w}{u} - \frac{-q \cdot x_i + p \cdot y_i}{u} - \frac{\frac{w}{u} \cdot q \cdot z_i}{u} \tag{8.5}$$

In this case, x_i, y_i, and z_i represent the distance between the location of interest and the center of gravity of the aircraft. However, Equation 8.4 assumes no fuselage pitch, small angles of attack and negligible effects of the yawing moment on the wing angle of attack. Therefore, it is further adapted to Equation 8.6.

$$\alpha^* = \theta - \arctan\left[\frac{u(w - q \cdot x_i + p \cdot y_i) - w(q \cdot z_i + r \cdot y_i}{u^2}\right] \tag{8.6}$$

The resulting angle of attack and sideslip applied to the tail leading edge, wing leading edge and nose of the aircraft are shown in Equation 8.7.

$$\begin{aligned}
\alpha_{nose} &= \theta - atan(\frac{w - q \cdot x_{CG}}{u}) \\
\alpha_{W,L} &= \theta - atan(\frac{u(w - q \cdot x_{wing_{LE}} + p \cdot y_{wing}) - w(q \cdot x_{wing_{LE}} - r \cdot y_{wing}}{u^2}) \\
\alpha_{W,R} &= \theta - atan(\frac{u(w - q \cdot x_{HS_{LE}}) - w(q \cdot x_{HS_{LE}}}{u^2}) \\
\alpha_{HS} &= \theta - atan(\frac{u(w - q \cdot x_{wing_{LE}} - p \cdot y_{wing}) - w(q \cdot x_{wing_{LE}} + r \cdot y_{wing}}{u^2}) \\
\beta_{nose} &= asin(\frac{v + r \cdot x_{CG}}{V_\infty}) \\
\beta_{VS} &= asin(\frac{v + r \cdot X_{VS} - p \cdot z_{VS}}{V_\infty})
\end{aligned} \tag{8.7}$$

Eigenmode Analysis

With the additional consideration of its moments of inertia and rotational couplings, the six degree of freedom model is linearized by following the procedure in Section 8.2 and the states responsible for each eigenmode are identified using modal analysis as explained in Section 8.2.1. Although flight dynamics models are often non-dimensionalized before linearization to facilitate comparison with other vehicles of different mass and geometry, this report does not concerns itself with performance and control of the vehicle. The CL-84 was known to be equipped with a complicated mixing box of controller to allow stable flight, so the natural dynamics are expected to contain at least some unstable eigenmodes. Therefore, this Section focuses on eigenmode analysis and pole location rather than time domain performance and error tracking, and comparison to other vehicles is deemed to be fruitless without a controller. For this reason, the linear models obtained are dimensional.

The model is linearized at [0, 14, 28, 41, 80, 85] degrees of wing tilt to echo the verification data available from Nieusma (1993). The states selected exclude the directional orientation with respect to North, $\dot{\psi}$,

because it typically does not contribute to eigenmode dynamics, leaving eight states. For those eigenmodes that are not stable, it is useful to know that whether it is stabilizable. Each eigenmode with eigenvalues greater than 0 correspond to an unstable dynamic of the system and the greater the eigenvalue is, the more quickly the aircraft will go out of control when that eigenmode is excited. Therefore it is useful to know whether there exists a set of control inputs such that the unstable eigenmodes can be stabilized. To explore this, the rank of $(\lambda_i \boldsymbol{I} - A, B)$ must be equal to the size n of matrix $\boldsymbol{A}$ for all unstable eigenvalues, or λ with a real part greater than 0 (Olsder et al., 2011). Since the system is over-actuated, there is a large control matrix, B, and the stabilizability analysis is not pushed further in this report.

The eigenmodes are labeled consistent with both helicopter and fixed-wing convention, as exampled in the works of Pavel (1996), G.Steinbusch (2021), Durham (2013), and van Holten and Melkert (2002). An explanation of each mode and what they represent follows. When stable, the eigenmodes converge to a steady-state condition, but when they are unstable, the aircraft motion will grow larger until it is out of control. The evolution of eigenmodes is classified by Di Giorgio (2018) in Figure 8.9.

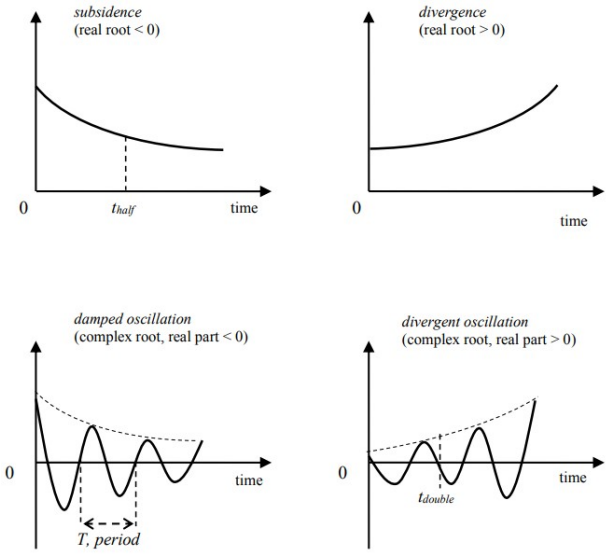

Figure 8.9: Evolution of eigenmodes during perturbed motion (Di Giorgio, 2018)

Longitudinally, the common fixed-wing modes are the Phugoid and the Short Period (Durham, 2013). They are both oscillatory patterns resulting from the interaction between two aircraft states. For the phugoid, the forward speed u and the aircraft attitude θ interact, resulting in an oscillatory pattern. The aircraft gains speed, causing a pitch up attitude, which reduces the forward speed, causing a drop in pitch attitude, once again increasing the forward speed. This mode typically has a low frequency and therefore a long period, and is usually marginally stable or even unstable. The Short Period mode functions similarly though it is dominated by the interaction between the angle of attack α and the pitching moment q. It is also characterised by a higher frequency and shorter period, as the name suggests. In helicopter flight dynamics, Di Giorgio (2018) shows that the Phugoid mode is typically similar as the fixed-wing, but the short period is not. The Heave Subsidence dominated by the heave state w and the Pitch Subsidence dominated by the pitching moment q are common. In the context of this report, a Surge Subsidence, dominated by u is also worth defining.

The lateral direction modes are normally shared by both fixed-wing and helicopters. There is usually and oscillatory mode, the Dutch Roll, dominated by v and r, a Roll Subsidence responding to perturbations in p, and a Spiral Subsidence from ϕ. It is important to stabilize the Dutch Roll. It is a swaying motion with the wingtips drawing spirals in the ski (Durham, 2013) and it is known to cause passenger discomfort and sickness. The Roll Subsidence normally is well damped, with a short period, but the Spiral Subsidence can often be unstable. Finally, the Sway Subsidence from state v needs to be identified.

Using this modal analysis, the eigenvalues, or poles can be tracked at the selected wings tilt for the specified airspeeds. The modal analysis matrices are reported in Appendix E. In general, the eigenmodes

found were often not neatly categorized into the typical modes and the interactions between the active states sometimes changes for the same wing angle as the airspeed increased.

First, the eigenmodes at wing tilt angle $85°$ are shown in Figure 8.10 and Figure 8.11. The longitudinal pitch mode is unstable in backward flight and then very stable in forward flight. This is consistent with the findings of the static stability derivatives that show a significant pitch damping near hover. The phugoid also demonstrates much more damping around hover than at faster speeds. The lateral directional eigenmodes were more mixed than typical helicopter dynamics, with a yaw mode turning to a heave mode with greater airspeed and a mixed Dutch Roll.

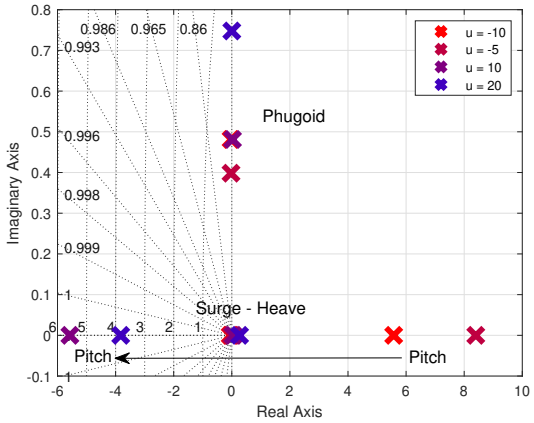

Figure 8.10: Longitudinal poles at $\eta = 85°$

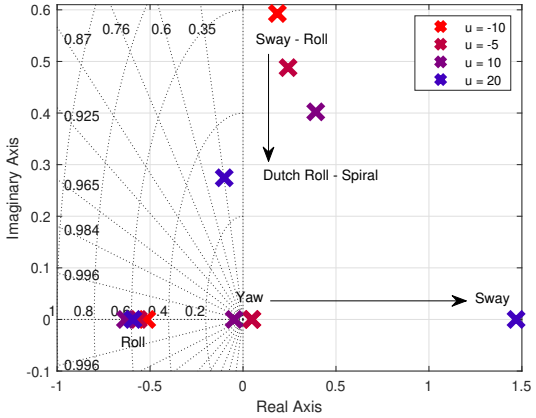

Figure 8.11: Lateral Directional poles at $\eta = 85°$

The eigenmodes of the aircraft at wing tilt angle $80°$, presented in Figure 8.12 and Figure 8.13, show very similar behaviour to the hover configuration discussed above. The modal analysis provides indicators of shifting dynamics. The phugoid is entangled with the heave mode, and the lateral directional modes are fairly mixed together.

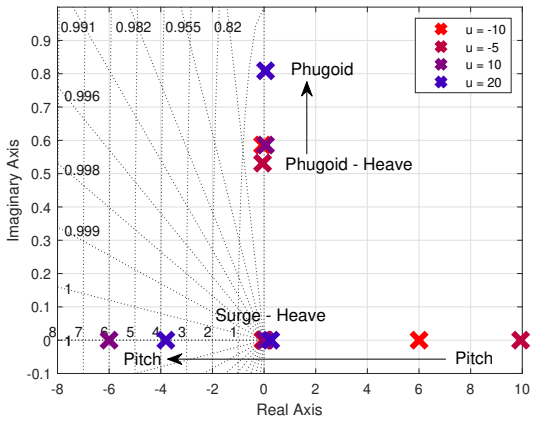

Figure 8.12: Longitudinal poles at $\eta = 80°$

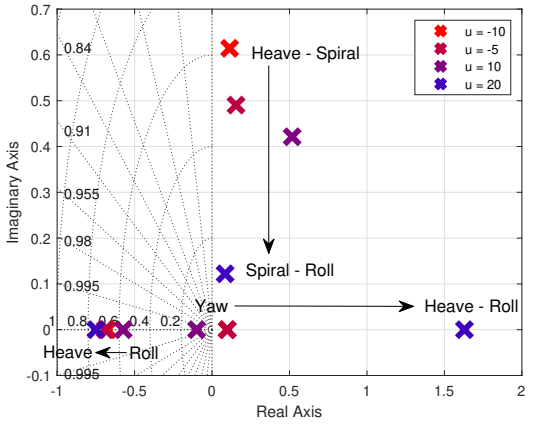

Figure 8.13: Lateral Directional poles at $\eta = 80°$

The eigenmodes of flight configurations with the wing at $41°$ are shown in Figure 8.14 and Figure 8.15. Although the longitudinal modes are not cleanly attributable to main contributing states, the phugoid pair of u and θ is recurrent. In the lateral direction figure, a trend emerges that remains true as the wing tilt angle is lowered to zero. The roll and spiral mode emerge clearly, each attribute to p and ϕ respectively. The roll mode is very unstable and the spiral mode is marginal at best. However, the dutch roll is split into two non-oscillatory modes that respond to perturbations in v and r.

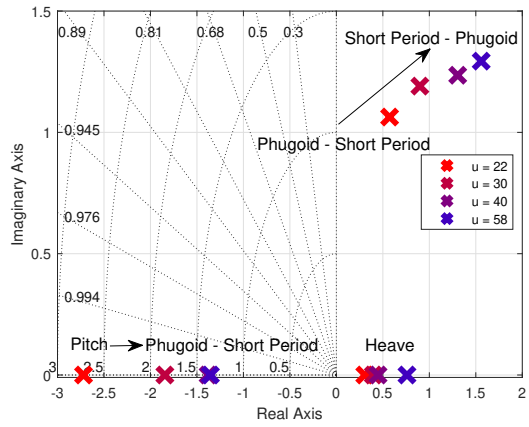

Figure 8.14: Longitudinal poles at $\eta = 41°$

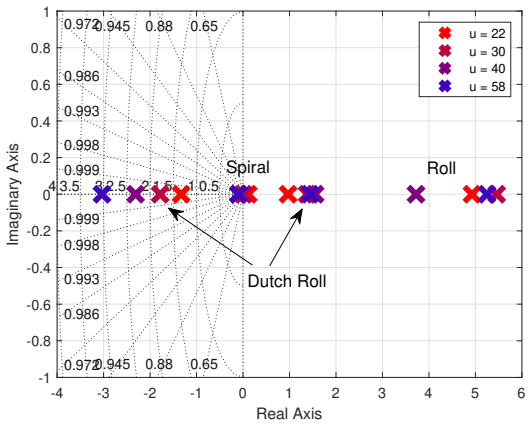

Figure 8.15: Lateral Directional poles at $\eta = 41°$

The eigenmodes of flight configurations with the wing at $28°$ are shown in Figure 8.16 and Figure 8.17. The lateral directional modes continue to behave similarly, with a distinct roll, spiral, and dutch roll mode. The roll mode continues to be very unstable and the spiral mode just marginally stable. The dutch roll is again split a stable and an unstable non-oscillatory pole. In the longitudinal poles, the heave mode becomes very distinct. The phugoid states and the pitch mode intertwine.

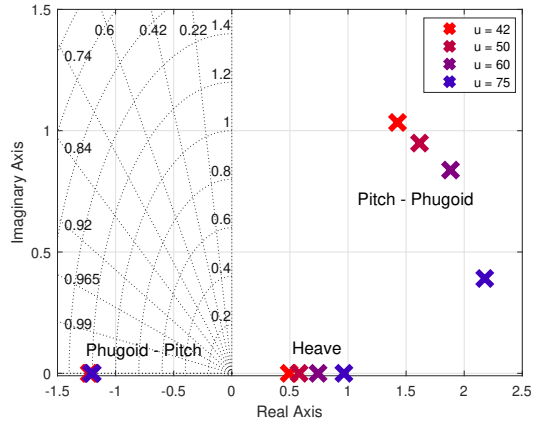

Figure 8.16: Longitudinal poles at $\eta = 28°$

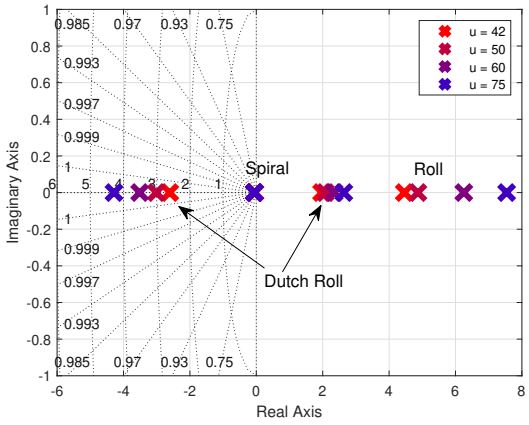

Figure 8.17: Lateral Directional poles at $\eta = 28°$

The eigenmodes of flight configurations with the wing at $14°$ are shown in Figure 8.18 and Figure 8.19. The lateral directional modes behave identically to the previous two flight conditions, though the dutch roll mode poles are separating farther along the x-axis, one pole becoming more unstable while the other becomes more stable. The roll mode is also grown more unstable as the wing tilt angle lowers. While the phugoid mode remains recognisable, the pitch and heave mode struggle to form distinct eigenmodes.

The cruise configuration is showing in Figure 8.20 and Figure 8.21. The lateral directional modes continue to grow more unstable as the wings lower and the flight speed increases. The longitudinal poles separate completely into rotational and translational modes, almost all unstable.

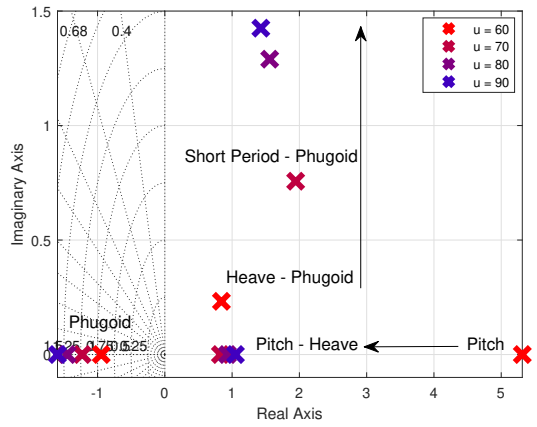

Figure 8.18: Longitudinal poles at $\eta = 14°$

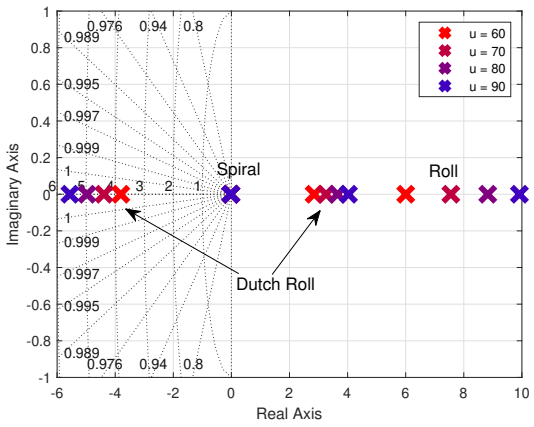

Figure 8.19: Lateral Directional poles at $\eta = 14°$

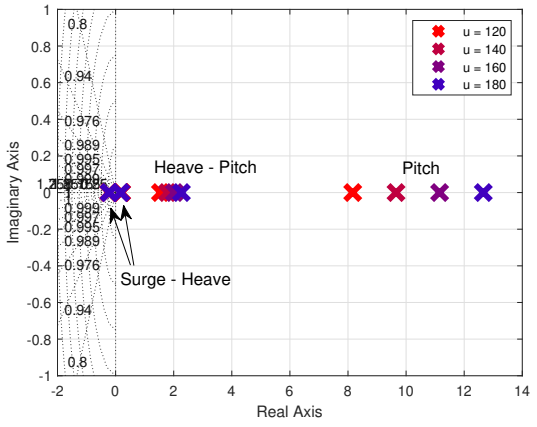

Figure 8.20: Longitudinal poles at $\eta = 0°$

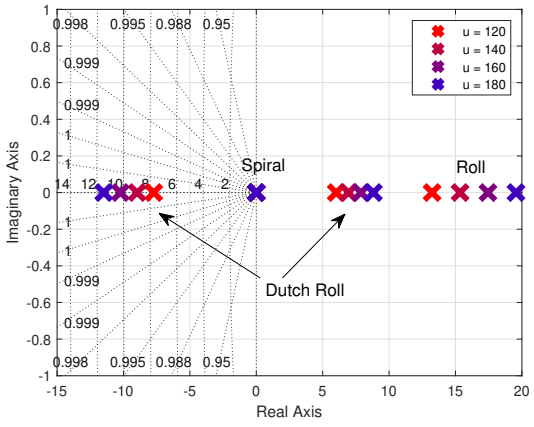

Figure 8.21: Lateral Directional poles at $\eta = 0°$

The dynamic stability of the aircraft, unstable in most hover modes, decreases further as the aircraft reaches cruise configuration. This is consistent with the feedback received from the test pilots according to Michaelsen (1971), although the CL-84 was said to have relatively good handling qualities in hover and through the transition. Besides any simplifying assumption made in this report, there is a large difference between the CL-84 and the model: the stability augmentation system (SAS). The CL-84's mixing box is not included in the model here.

Nevertheless, even without a SAS mixing box, the eigenmode representation of the model suggests that the CL-84 is not well characterised. When the wings are vertical, it is understandable that the eigenmode representation would not be typical of either helicopters or fixed-wings because the wings provide a large amount of damping. However, as the wings lower and the aircraft reaches a cruise configuration comparable to fixed-wings, the dynamics modes can reasonably expected to follow suit. As such, the expectation for the $0°$ configuration is a clean phugoid and short period oscillation in the longitudinal eigenmodes, and an oscillation caused by perturbations in v and r to form a dutch roll followed by a spiral and roll mode. Currently, the spiral and roll modes are the only ones that match the expected results. Further, the static stability coefficients suggested that a change in w or u at hover would induce a large response in pitching moment q, which reasonably might be expected to induce a change in pitch attitude θ. This interplay dynamics is not clearly visible in the linear models at and around hover shown in Figure 8.10 and Figure 8.10.

Some of the reason for this could involve the assumptions made in the model. Critically, the effect of rotations on the local angle of attack has a large influence on the eigenmodes. In this case, the local angle

of attack was assumed to be a kind of average: for example, one angle of attack is calculated for each wing at the leading edge mid-span. Similarly, one angle of attack is determined for the horizontal tail, and it is based on the average flow disturbance from the differential rotors and wing. As a result, the horizontal tail remains unaffected by lateral directional control inputs. Another possible factor for the strangeness of the eigenmode is the sizing of the elevator. It was established from the validation tests in Chapter 7 that the elevator is sized differently in this report than it was on the CL-84. On top of that, the elevator motion is designed in a most simplistic manner, which impacts the initial condition at trim. It is also possible that the trim configurations selected for evaluation in this section are impractical because the elevator deflection is inadequate.

Part VI

Closure

9

Conclusions & Recommendations

9.1. Conclusions

The research objective and associated research questions posed in Chapter 1 are repeated below for convenience.

Research Objective

- Develop a non-linear 3 degree of freedom longitudinal flight dynamics model of a tilt-wing aircraft.
- Study the trim, validate the model, and establish a flight envelope.
- Extend the non-linear flight dynamics model to 6 degrees of freedom with lateral and directional dimensions.
- Study the trim, validate the model, and establish a flight envelope.
- Linearize the 6 degree of freedom model and analyse the characteristics.

Each item within the objective is addressed in the report and contributes to answering the research questions formulated in Chapter 1. Starting with research question 1, restated below.

Research Question 1

What are the flight dynamic characteristics of the non-linear model of a tilt-wing aircraft?

The flight dynamic characteristics of the tilt wing configuration have been examined throughout the wing transition and at several velocity points for some wing tilt angles. The trim is examined from a control input viewpoint to determine what control inputs are required to establish trimmed flight throughout the wing tilt transition.

Research Question 2

What is the trim corridor of a tilt-wing aircraft?

The trim corridor of the model is established using a specific set of instructions. One of the current limitations of the model is the absence of an optimization algorithm. As a results, the trim corridor proposed in this report could be extended by increasing the freedom given to the elevator deflections.

Research Question 3

How can the non-linear model, implemented on Canadair's CL-84 Dynavert tilt-wing, be validated against flight test data?

Both the three, then the six degree of freedom models are partially validated in Chapter 5 and Chapter 7 respectively. The behaviour of the mode has room for improvement around the hover regime, but provides

a good low fidelity estimate for predicting the behaviour of the CL-84 in other flight configurations. No validation data could be used to compare the behaviour of the model in non-symmetrical flight, so this part of the model was not examine in any depth.

Research Question 4

What is the impact of the angle of wing tilt on the general dynamics and in particular on the stability? Similarly, what is the impact of the airspeed on the dynamics?

The results of the linearized model in terms of the eigen mode representation of the vehicle's response to disturbances is difficult to compare to other aircraft. The static stability characteristics offer an intriguing avenue for further research to account for the specific behaviour of the tilt wing configuration. Unfortunately, the unexpected dynamic behaviour predicted by the linearized models cannot be fully explained by the unique behaviour of the wings on the CL-84, since the cruise configuration also features strange behaviour. There is some indication that the aircraft becomes less stable and more difficult to control in the cruise configuration, which is consistent with the pilot feedback as described by Michaelsen (1971). Regardless, it is unlikely that the CL-84 exhibited such unique eigenmode behaviour.

9.2. Recommendations

The model developed in this report can be extended in several different ways. One direction could be to improve the reliability of its prediction. To achieve this, the simplified rotor-wing-tail interactions needs to be examined in greater detail and modelled with more accuracy. There is undoubtedly room for growth in this regard, as demonstrated by the validation test in the hover configuration. Currently, the slipstream model and the wing-tail interactions are considered very pragmatically while overlooking some of the dynamics at play. In a similar sense, some of the simplifying assumptions regarding the effect of the horizontal and vertical tail could be re-examined. This might include modelling the aerodynamic forces and moment more accurately and accounting for the effect of the tail rotor wake in backward flight.

Another area where the model could be refined further is the interaction between longitudinal effects and the lateral-directional ones. Even fixed-wing aircraft typically have some interplay between all three movement modes, but in this case the modal analysis from Appendix E reveal that there is a total de-coupling between longitudinal states and the lateral-directional ones. The conclusion here is that there are missing pieces in terms of the factors that affect the aerodynamic forces.

Also, the model's reach could be improved by using an optimisation algorithm to solve for the trim parameters. Improving the trimming algorithm in this regard could lead to a much wider transition corridor that might include a constant fuselage attitude. Implementing an optimization algorithm would enlarge the scope of application for this model as well, enabling research into minimal control actuation or emissions for example.

Finally, the eigenmode representation suggest that the linearized models require further fine tuning. It is difficult to pinpoint the cause of the strange behaviour of the linear models, though the rotational velocity to effective angle of attack couplings are a likely source. This is because they are the only unverified element of the linearization process, whereas all the elements used for trimming the model are verified through the trimmed transition corridor with all rotational rate set to zero.

References

J.D. Anderson. 2012. *Aircraft Performance and Design* (5th ed. ed.). Tata McGraw Hill Edition, New Delhi, India.

Joseph R. Chambers and Sue B. Grafton. 1968. Calculation of the Dynamic Longitudinal Stability of a Tilt-Wing V/STOL Aircraft and Correlation with Model Flight Tests. *NASA Technical Note NASA TN D-4344* (1968).

Joseph R. Chambers and Sue B. Grafton. 1970. Investigation of Lateral-Directional Dynamic Stability of a Tilt-Wing V/STOL Transport. *NASA Technical Note NASA TN D-5637* (1970).

William F. Chana and T. M. Sullivan. 1994. The Tilt Wing Configuration For High Speed VSTOL Aircraft. *ICAS 1994 Anaheim* 1 (1994), 871–889.

C. C. Critzos et al. 1955. Aerodynamic Characterics of NACA0012 Airfoil Section at Angles of Attack From 0 degrees to 180 degrees. *National Advisory Committee for Aeronautics, Technical Note 3361* (1955).

G Di Giorgio. 2018. *Theory of Helicopter Flight* (1st ed. ed.). Gioacchino Onorati editore, Rome, Italy. ISBN: 978–88–255–1442–1.

W. Durham. 2013. *Aircraft Flight Dynamics and Control* (1st ed. ed.). John Wiley Sons, Ltd, West Sussex, UK. ISBN: 978-1-118-64681-6.

R. J. Englar and D. G. Kirkpartick. 1969. Parametric Trade-off Analysis for Tilting Free Propulsor V/STOL Aircraft in Equilibrium Transition. *Naval Ship Research and Development Center* (1969).

C.P. Frederick. 1990. The Canadair CL-84 Experimental Aircraft Lessons Learned. *American Institute of Aeronautics and Astronautics AIAA-90-32-05* (1990).

W.J. Fredericks et al. 2017. Greased Lightning (GL-10) Flight Testing Campaign. *NASA/TM-2017-219643* (2017).

G.Steinbusch. 2021. A Theoretical Approach for Analysing the Stability Characteristics of Tiltrotor Aircraft. *Delft Institute of Technologies, MSc Thesis* (2021).

S. Gudmundsson. 2014. *Generatl Aviation Aircraft Design* (1st ed. ed.). Elsevier Inc., Oxford, UK. ISBN: 978-0-12-809998-8.

H.H.B.M.Thomas. 1977. An Introduction to the Aerodynamics of Flight Dynamics. *Royal Aircraft Establishment, Technical Memorandum Aero 1710* (1977).

William S. Hindson et al. 1993. Piloting Considerations for Terminal Area Operations of Civil Tiltwing and Tiltrotor Aircraft. *Piloting Vertical Flight Aircraft: A Conference on Flying Qualities and Human Factors* (1993).

Robert W. Kress and David F. Gebhard. U.S. Patent 5,141,176, Jun. 1991. Tilt Wing VTOL aircraft.

B. Lawrence et al. 2016. Integrating Flight Dynamics and Control Analysis and Simulation in Rotorcraft Conceptual Design. *Conference: American Helicopter Society 72nd Annual Forum* (2016).

W.S. Longhurst. 1966. A Report on Stability and Control Testing of a Tilt Wing V STOL Aircraft. *SAE Technical Paper 660315* (1966).

Marc May, Daniel Milz, and Gertjan Looye. 2021. Dynamic Modeling and Analysis of Tilt-Wing Electric Vertical Take-Off and Landing Vehicles. *AIAA 2022-0263. AIAA SCITECH 2022 Forum* (2021).

D.M. McGregor. 1965. Simulation of the Canadair CL-84 tilt-wing aircraft using an airborne V/STOL simulator. *National Research Council Aeronautical Report LR 435* (1965).

O.E. Michaelsen. 1971. Application of V/STOL Handling Qualities Criteria to the CL-84 Aircraft. *AGARD Conference Proceedings No. 106 on Handling Qualitities Criteria* (1971).

Daniel Milz and Gertjan Looye. 2022. Tilt-Wing Control Design for a Unified Control Concept. *AIAA 2022-1084. AIAA SCITECH 2022 Forum* (2022).

N. Nguyen and I. Tuzcu. 2009. Flight Dynamics of Flexible Aircraft with Aeroelastic and Inertial Force Interaction. *AIAA* (2009).

W.J Nieusma. 1993. An investigation of twopropeller tilt wing VSTOL aircraft flight characteristics. *Naval Postgraduate School* (1993).

G.J. Olsder et al. 2011. *Mathematical System Theory* (4th ed. ed.). VSSD, Delft, The Netherlands. ISBN: 13-978-90-6562-280-8.

M. D. Pavel. 1996. “Six Degree-of-Freedom Linear Model for Helicopter Trim and Stability Calculation”, Memorandum M-756.

G Perez, D et al. 2023. High-Fidelity Simulations of a Tiltwing Vehicle for Urban Air Mobility. *AIAA* (2023).

Felix Rubin. 2018. Modelling Analysis of a TiltWing Aircraft. *Master Thesis for Royal Institute of Technology Stockholm, Sweden* (2018).

L. M. Sanchez-Rivera et al. 2020. Transition Flight Dynamics of a Dual Tilt-Wing UAV. *IEEE 2020 International Conference on Unmanned Aircraft Systems (ICUAS)* (2020).

D. Scholz. 2017. High Lift Systems and Maximum Lift Coefficients. *Lecture Notes* (2017). `https://www.fzt.haw-hamburg.de/pers/Scholz/HOOU/AircraftDesign_8_HighLift.pdf` Last updated 13/06/2023.

John W.R. Taylor. 1960. *Jane’s all the world’s aircraft 1959-1960*. Marston Co.

Joseph J. Totah. 1992. A mathematical model of a tilt-wing aircraft for piloted simulation. *NASA technical memorandum 103864* (1992).

T. van Holten and J. A. Melkert. 2002. *Helicopter Performance, Stability and Control*. TU Delft.

The Vertical Flight Society VFS. 2020. *Urban Air Taxis Underway — UAM at Heli-Expo*. `https://evtol.news/news/urban-air-taxis-underway-uam-at-heli-expo` Last accessed 14/12/2023.

The Vertical Flight Society VFS. 2024. *V/STOL Aircraft and Propulsion Concepts*. `https://vtol.org/vstol/wheel.htm`

A

Trim Algorithms

This appendix contains the algorithms used for trimming. The trim routine is perform in two steps. The first step resolves the equations of motion at a specified wing tilt angle and forward velocity. This part of the trim procedure is presented by Table A.1 for the longitudinal equations of motion and the expansion to directional lateral motion is presented by Table A.2. The first step results in the operating point value for some of the control input vector, $[\eta, \delta_e]$ and the state variables, $[\theta, u, w, T_m, T_t]$. However, the thrust parameters are presented as control variables with respect to the equations of motion in preparation for the second trimming procedure. The second step in the trimming procedure works through the thrust values to determine the effective control inputs, $\omega_{m,t}$ and $\theta_{0_{m,t}}$. The additional considerations required for trimming the six degree of freedom equations of motion with lateral directional capabilities are presented in Table A.2.

Table A.1: Trim algorithm for longitudinal equations of motion

Aircraft parameters	S_i x_i z_i $CG_{x,z}$ k_{1f} $\Delta_{c_{l_{flap,max}}}$ C_{d_b} $C_{d_{o_f,n}}$ F_f $C_{L_w}(\alpha)$ $C_{D_w}(\alpha)$
Control variables	η δ_e T_m T_t
State variable	θ w u
$0\ deg < \eta < 90\ deg : \delta_f(deg)$ and $\delta_{HS}(deg)$ are scheduled with η:	Eqs. (4.19) and (4.23)
Estimate k_{2_f} and k_{3_f} with $\delta_f(deg)$:	Eqs. (4.17) and (4.18)
Estimate $\Delta_{c_{l_{flap}}}$ with k_{1_f}, k_{2_f}, k_{3_f}, and $\Delta_{c_{l_{flap,max}}}$:	Eq. (4.16)
Recall $V \equiv \sqrt{u^2 + w^2}$ and $\bar{q} \equiv \frac{1}{2}\rho V^2$	Using definitions
Recall $\alpha \equiv \theta - arctan(\frac{w}{u})$. At w = 0, $arctan(\frac{w}{u}) = 0 \ \forall \ u > 0$	Using definition
Estimate ζ	Eq. (4.7)
Define $\alpha_s = \eta + \alpha - \zeta$	Eq. (4.8)
Estimate $\bar{q}_s$	Eq. (4.9)
Optional: Estimate L_N and D_N	Eqs. (4.29) and (4.31)
Estimate L_F and D_F	Eqs. (4.33) and (4.35)
Estimate α_w from δ_f, α_s, and geometry	Eqs. (4.11) to (4.15)
Estimate L_W, D_W, and M_{AC_W}	Eqs. (4.20) to (4.22)
Estimate ε	Eq. (4.24)
Estimate $\alpha_{HS} = \alpha - \zeta - \varepsilon + \delta_{HS}$	Eq. (4.25)
Estimate L_{HS}, D_{HS}, and $M_{AC_{HS}}$	Eq. (4.27)
Estimate L_e, D_e, and M_{AC_e}	Eq. (4.28)
Set accelerations to 0 and solve $\sum \mathcal{F}_x = 0$, $\sum \mathcal{F}_z = 0$, and $\sum \mathcal{M}_q = 0$	Eq. (4.40)
Solve for $[\theta, T_m, T_t]$ until $T_{t_{eff}} = 0$. Then solve for $[u, T_m, \delta_e]$	

Table A.2: Trim algorithm for lateral directional equations of motion based on Table A.1

Aircraft parameters	$S_i \quad x_i \quad z_i \quad y_i \quad I_{yy} \quad CG_{x,z} \quad C_{d_b} \quad C_{d_{o_{f,n}}}$
Control variables	$\delta_a \quad \delta_r \quad T_{m,L} \quad T_{m,R}$
State variable	$\phi \quad \psi \quad v$
T_m separates into $[T_{m,L}, T_{m,R}]$	
δ_f separates into left ($+\delta_a$) and right ($-\delta_a$): $[\delta_{f,L}, \delta_{f,R}]$	
ζ separates into left $[\zeta_L, \zeta_R]$	
Recall $\beta \equiv -arctan(\frac{v}{u})$. At v = 0, $\beta = 0 \; \forall \; u > 0$	Using definition
Estimate $L_{f,Y}$ with β instead of α:	Eqs. (4.33) and (4.35)
Estimate L_{VS}, D_{VS}, and $M_{AC_{VS}}$	Eq. (4.27)
Estimate L_r, D_r, and M_{AC_r}	Eq. (4.28)
Define $\alpha_{s_{L,R}} = \eta + \alpha - \zeta_{L,R}$	Eq. (4.8)
Estimate $\bar{q}_{s_{L,R}}$	Eq. (4.9)
Average left and right contribution of ζ and ε on horizontal stabilizer	
Estimate $L_{W_{L,R}}$, $D_{W_{L,R}}$, and $M_{AC_{W\,L,R}}$	Eqs. (4.20) to (4.22)
Estimate α_{HS} using $\bar{\zeta}$ and$\bar{\varepsilon}$	Eq. (4.25)
Estimate L_{HS}, D_{HS}, and $M_{AC_{HS}}$	Eq. (4.27)
Estimate L_e, D_e, and M_{AC_e}	Eq. (4.28)
Set all accelerations to 0	
Solve $\sum \mathcal{F}_x = 0$, $\sum \mathcal{F}_y = 0$, $\sum \mathcal{F}_z = 0$, $\sum \mathcal{L}_p = 0$, $\sum \mathcal{M}_q = 0$, and $\sum \mathcal{N}_r = 0$	Eqs. (6.4) to (6.9)

Table A.3: Trim algorithm for propeller forces

Aircraft parameters $\quad R_{m,t} \quad T_{m,t} \quad c_{l_\alpha}$
Control variables $\quad \eta \quad \lambda_{i_{m,t}} \quad \Omega_{m,t} \quad \theta_{0_{m,t}}$
State variable $\quad \theta \quad w \quad u$
$V = \sqrt{u^2 + w^2}$
$\alpha = \theta - arctan(\frac{w}{u})$
$\alpha_{c_m} = \frac{\pi}{180} - \eta - \alpha$
$\alpha_{c_t} = \frac{\pi}{180} - \alpha$
$\Omega_m = 0.98 * c - \lvert u \cdot sin(\eta) \rvert / R_m$
$\Omega_t = 0.98 * c - \lvert u \rvert / R_t$
$\mu_{m,t} = \frac{V cos(\alpha_{c_{m,t}})}{\Omega_{m,t} R_{m,t}}$
$\lambda_{c_{m,t}} = \frac{V sin(\alpha_{c_{m,t}})}{\Omega_{m,t} R_{m,t}}$
$C_{T_{m,t}} = \frac{1}{2} \frac{T_{m,t}}{\rho (\Omega_{m,t} R_{m,t})^2 \pi {R_{m,t}}^2}$
$C_{T_{glau,m,t}} = \lambda_{i_{m,t}} \sqrt{\left(\frac{V}{\Omega_{m,t} R_{m,t}} cos(\alpha_{c_{m,t}}) \right)^2 + \left(\frac{V}{\Omega_{m,t} R_{m,t}} sin(\alpha_{c_{m,t}}) + \lambda_{i_{m,t}} \right)^2}$
Solve $C_{T_{glau,m,t}} = C_{T_{m,t}}$ for $\lambda_{i_{m,t}}$. Select the real, positive solution.
$C_{T_{BEM,m,t}} = \frac{1}{4} c_{l_\alpha} \sigma \left[\frac{2}{3} \theta_{0_{m,t}} \left(1 + \frac{2}{3} {\mu_{m,t}}^2 \right) - (\lambda_{c_{m,t}} + \lambda_{i_{m,t}}) \right]$
Solve $C_{T_{BEM,m,t}} = C_{T_{m,t}}$ for $\theta_{0_{m,t}}$

B

Geometry of the CL-84

This appendix stores the geometry and parameters used to personalize the model to the CL-84.

Parameter	Value	Units	Source
Main rotor radius R_m	14	ft	Taylor (1960)
Tail rotor radius (coaxial) R_t	7 (x2)	ft	Taylor (1960)
Main rotor solidity σ	0.16	-	Nieusma (1993)
Tail rotor solidity σ	0.16	-	Assumed
Wingspan	10.16	m	Taylor (1960)
Wing average chord	2.13	m	Taylor (1960)
Fuselage cross sectional area	2.13	m^2	Estimated based on Taylor (1960)
Fuselage equivalent plane plate factor	0.4	-	Estimated based on Pavel (1996)
Tailplane area	8.13	m^2	Taylor (1960)
Tailplane chord	5.25	ft	Nieusma (1993)
Elevator proportion of tailplane	30	%	Estimated based on Taylor (1960)
Vertical stabilizer area	5.49	m^2	Taylor (1960)
Rudder area	0.38	m^2	Taylor (1960)
Flap area	3.28	m^2	Taylor (1960)
Flap $\Delta_{CL_{max}}$	1.72	-	Taylor (1960)
Flap k_1	0.81	-	Scholz (2017)
Nacelle profile drag coefficient C_{d0_n}	0.045	-	Englar and Kirkpartick (1969)
Basic cylindrical drag coefficient C_{db}	1	-	Englar and Kirkpartick (1969)
Fuselage profile drag coefficient C_{d0_f}	0.0167	-	Englar and Kirkpartick (1969)
NACA$_6$33418 drag coefficient C_{D_W}	$C_{D_W}(\alpha)$	-	Englar and Kirkpartick (1969)
NACA$_6$33418 lift coefficient C_{L_W}	$C_{L_W}(\alpha)$	-	Englar and Kirkpartick (1969)

Table B.1: CL-84 parameters

Attribute	Value	Units	Source
Fuselage weight	3350	lb	Nieusma (1993)
Fuselage station location	228	in	Nieusma (1993)
Fuselage waterline location	70	in	Nieusma (1993)
Payload weight	2625	lb	Nieusma (1993)
Payload station location	195.7	in	Nieusma (1993)
Payload waterline location	69	in	Nieusma (1993)
Wing weight	1237	lb	Nieusma (1993)
Wing station location (at $\eta = 80$)	192	in	Nieusma (1993)
Wing waterline location (at $\eta = 80$)	108	in	Nieusma (1993)
Wing buttock (y-axis) location (at $\eta = 80$)	$\frac{wingspan}{4}$	in	Estimated based on Taylor (1960)
Nacelles weight	2613	lb	Nieusma (1993)
Nacelles station location (at $\eta = 80$)	158	in	Nieusma (1993)
Nacelles waterline location (at $\eta = 80$)	86	in	Nieusma (1993)
Propellers station location (at $\eta = 80$)	119.5	in	Nieusma (1993)
Propellers waterline location (at $\eta = 80$)	86.8	in	Nieusma (1993)
Propellers buttock (y-axis) location (at $\eta = 80$)	3.15	in	Taylor (1960)
Fuel weight	1400	lb	Nieusma (1993)
Fuel station location (at $\eta = 80$)	183	in	Nieusma (1993)
Fuel waterline location (at $\eta = 80$)	107	in	Nieusma (1993)
Tailplane weight	210	lb	Estimated by ratio to wing planform
Tailplane station location	440.7	in	Nieusma (1993)
Tailplane waterline location	77.4	in	Nieusma (1993)
Tailplane buttock (y-axis) location (at $\eta = 80$)	$\frac{wingspan}{8}$	in	Estimated based on Taylor (1960)
Vertical stabilizer weight	142	lb	Estimated by ratio to wing planform
Vertical stabilizer station location	9.7	in	Estimated based on Taylor (1960)
Vertical stabilizer waterline location	1.96	m	Estimated based on Taylor (1960)
Wing pivot station location	200	in	Nieusma (1993)
Wing pivot waterline location	112	in	Nieusma (1993)

Table B.2: CL-84 weight and balance data

C

Center of Gravity

As the wing tilts, the weight distribution of large items such as the wings themselves, fuel, nacelles, and propellers shifts. This appendix describes how the shifting of the center of gravity (CG) is estimated and as a consequence how the moment of inertia of the aircraft is affected. Appendix C offers details on how the CG location varies with the tilting of the wings, while Figure C discusses the implication of the moments of inertia.

Center of Gravity

Information is available from Nieusma (1993) about the weight and balance of the CL-84 at wing tilt angle $\eta = 80$. The CG at $\eta = 0$ is known, which means that the station of waterline location of the moving elements can be tracked as they pivot. As the wings tilt, it is found that the center of gravity location can vary up to 9% along the body-x axis and 15% in the body-z axis, a difference that cannot be ignored. Therefore, the model proposed in this report considers a variable center of gravity with respect to wing tilt angle as shown in Figure C.1 below. It is noted that this effect does not consider any shift in center of gravity due to fuel consumption.

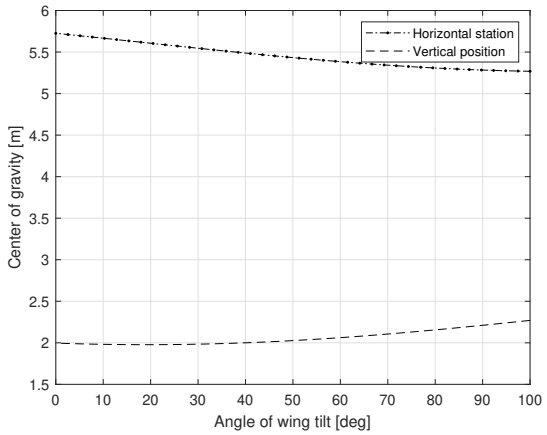

Figure C.1: Center of gravity distance to reference origin along the body-x and body-z axis at all wing tilt angles

A resulting complication of the shifting center of gravity is that it defines the origin of the body-fixed axes. This effect is taken into consideration because the location of the center of gravity is updated in the model for wing tilt angle. Therefore, all moment arms are adjusted accordingly.

Moments of Inertia

A vehicle's moment of inertia describes how its distribution of mass and geometry affects the way it rotates. An in-depth exploration of the dynamics of rotating bodies is outside the scope of this work and it is enough

here to estimate how the distribution of mass of an aircraft bears incidence on the way in which this body rotates. The moments of inertia, defined as in Equation C.1, provide information on how rotational accelerations affect a body such as an aircraft.

$$\begin{bmatrix} I_{xx} & -I_{xy} & -I_{xz} \\ -I_{xy} & I_{yy} & -I_{yz} \\ -I_{xz} & -I_{yz} & I_{zz} \end{bmatrix} = \begin{bmatrix} \int_m (y^2+z^2)dm & -\int_m (xy)dm & -\int_m (xz)dm \\ -\int_m (xy)dm & \int_m (x^2+z^2)dm & -\int_m (yz)dm \\ -\int_m (xz)dm & -\int_m (yz)dm & \int_m (x^2+y^2)dm \end{bmatrix} \tag{C.1}$$

There are various way to approximate an aircraft's moment of inertia without going through the trouble of integrating the mass over all its axes. Firstly, the non-diagonal elements in Equation C.1 show that a symmetry eliminates terms. In aircraft, the X-Z plane is typically a plane of symmetry, leaving only four moments of inertia to determine, I_{yy}, I_{xx}, I_{zz}, and I_{xz}. In this case, Nieusma 1993(1993) catalogues mass and location information available about various elements of the CL-84 so a pragmatic approach can be undertaken and the integrals are treated as summations. The resulting moments of inertia can be visualized at varying angle of wing tilt below.

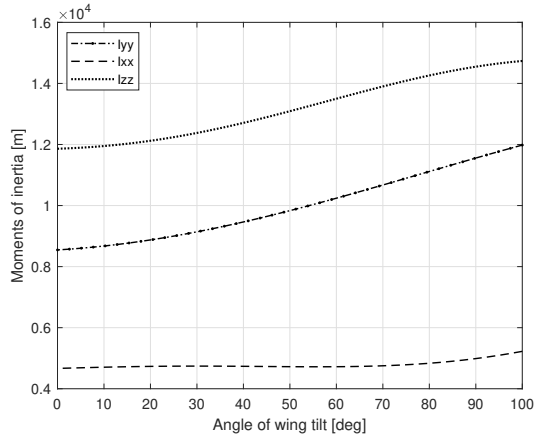

Figure C.2: Moments of inertia I_{yy}, I_{xx}, I_{zz} vs. η

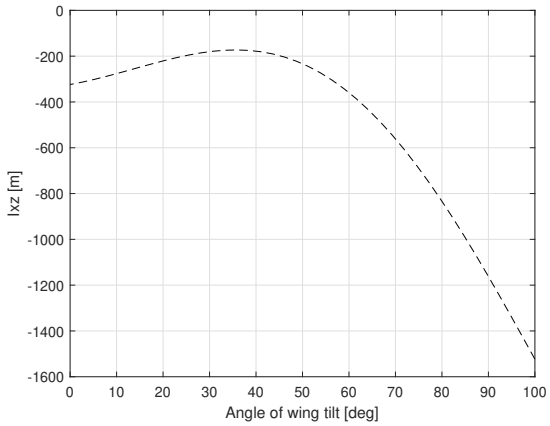

Figure C.3: Coupled moment of inertia I_{xz} vs. η

Unsurprisingly, there are significant changes in the values of the moments of inertia with respect to the wing tilt angle. This is unsurprising considering both the changes in center of gravity of the aircraft and that the wing's pivot is not aligned with the tilting system's center of gravity. The ratios between the highest and lowest absolute values for each moment of inertia are display in Table C.1 below.

I_{yy}	0.71
I_{xx}	0.81
I_{zz}	0.89
I_{xz}	0.11

Table C.1: Ratio of the lowest to highest absolute value for each moment of inertia

D

Coordinate System

This Appendix presents a discussion of some relevant coordinate systems and provides justification for selecting the convention used in this report. A fundamental aspect of studying flight dynamics is the use of coordinate systems to describe the position, orientation, and motion of an aircraft. Different coordinate systems provide various perspectives and simplify the analysis of different flight dynamics problems.

Inertial Coordinate System

An inertial coordinate system is defined by an origin that experiences absolutely no acceleration. In the strictest sense, if such a point even exists it might be the exact point from which the entire universe diverges. However, by loosening the definition and by assuming that the Earth's motion is negligible compared to that of an aircraft, the center of the Earth could also be considered to be the origin of an inertial reference system. This coordinate system is known as the Earth-Centered reference frame (Durham, 2013) and is useful when the object of study is considered to move very slowly relative to the Earth. When this assumption is made and the origin is placed at the center of the earth, this coordinate system is called the earth-centered reference frame. It is a fundamental reference frame in the study of aircraft flight dynamics. This coordinate system is used to describe the absolute motion of the aircraft with respect to the Earth. It is essential for understanding how the aircraft moves in a global context and for transforming coordinates between different reference frames.

The inertial coordinate system, represented visually in Figure D.1, is defined as follows:

- **Origin:** The origin of the inertial coordinate system is at the center of the Earth.
- The **x-axis**, x_{EC}, points towards the intersection of the lines of $0°$ longitude and $0°$ latitude, at the intersection of the Prime Meridian and the equator.
- The **z-axis**, z_{EC}, points toward the North through the axis of rotation of the Earth.
- The **y-axis**, y_{EC}, is determined using the right hand rule.

The inertial coordinate system is used in various applications within flight dynamics, such as tracking aircraft position and velocity in a global context or analysing a flight path relative to the Earth. This reference frame is built on several assumptions, including:

- **Non-rotating Earth:** The Earth is assumed to be non-rotating in the inertial frame.
- **Spherical Earth:** The Earth is assumed to be a perfect sphere, ignoring its actual oblate spheroid shape.
- **Constant Gravitational Field:** The gravitational field is often assumed to be uniform and constant, ignoring variations in the Earth's gravitational field.

Some aerospace and flight dynamics applications, such as satellite navigation or high precision methods, require a level of precision beyond the assumptions listed above. However, for the purpose of building a flight dynamics model of a relatively low speed and short range aircraft operating at arbitrary altitudes and latitudes, the assumptions of an inertial Earth are reasonable simplifications.

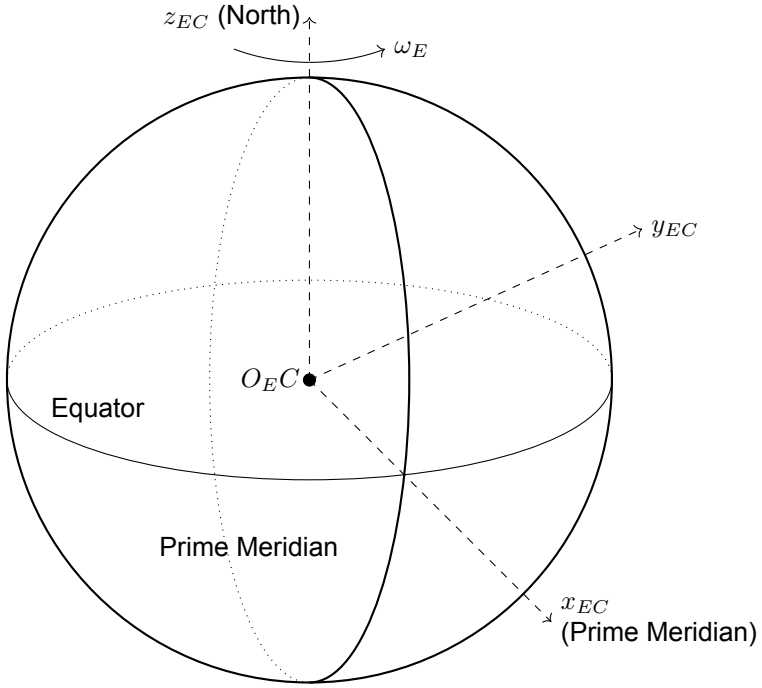

Figure D.1: Inertial Coordinate System: Definition of the Origin and Axes

Local Coordinate Systems

Although inertial reference frames can describe very accurately the position and acceleration of an object with respect to the Earth, it is difficult to use that framework to describe the object's orientation. Since an aircraft's attitude is defined with respect to the Earth's surface it is convenient to use reference frame with an origin on the Earth's surface or at least connected to a point on the Earth's surface. Such reference frames enable working with an X-Y plane parallel to the Earth surface at a point of interest. In this section, the Earth-fixed, and the North-East-Down (NED) reference frames are presented.

The Earth-fixed coordinate system is centered about an arbitrary point on the Earth's surface. This means that the entire reference frame rotates along with the Earth.

The Earth-fixed coordinate system is defined as follows:

- **Origin:** The origin is at a point of interest on the surface of the Earth. It is shown in Figure D.2 as O_E.
- The **x-axis**, x_E, points to the magnetic north.
- The **z-axis**, z_E, points toward the center of the Earth.
- The **y-axis**, y_E, points to magnetic east.

The assumptions behind this system are:

- **Spherical Earth:** The Earth is assumed to be a perfect sphere, ignoring its actual oblate spheroid shape.
- **Flat Earth Approximation:** The Earth is assumed to be flat to allow the use of Cartesian coordinates. This assumption is permissible, as long as the object under analysis stays close to the origin.

This reference frame is very useful for geological and ground-based applications. It is easily possible to described a vehicle's orientation with respect to the ground in this framework. However, it becomes somewhat cumbersome with sign conventions when it is necessary to describe flying objects.

The North-East-Down (NED) coordinate system is therefore designed describe changes in altitude. As shown in Figure D.2, the NED system is defined as follows:

- **Origin:** The origin is fixed to an arbitrary point of interest that could even be in motion with respect to the Earth.

- The **x-axis**, x_{NED}, points to the magnetic north.
- The **z-axis**, z_{NED}, points toward the center of the Earth.
- The **y-axis**, y_{NED}, points to magnetic east.

Although the same assumptions as the Earth-fixed reference frame typically hold, the rotation of the Earth and her curvature can be taken into account. Still, in this report all of the assumptions discussed before will remain intact.

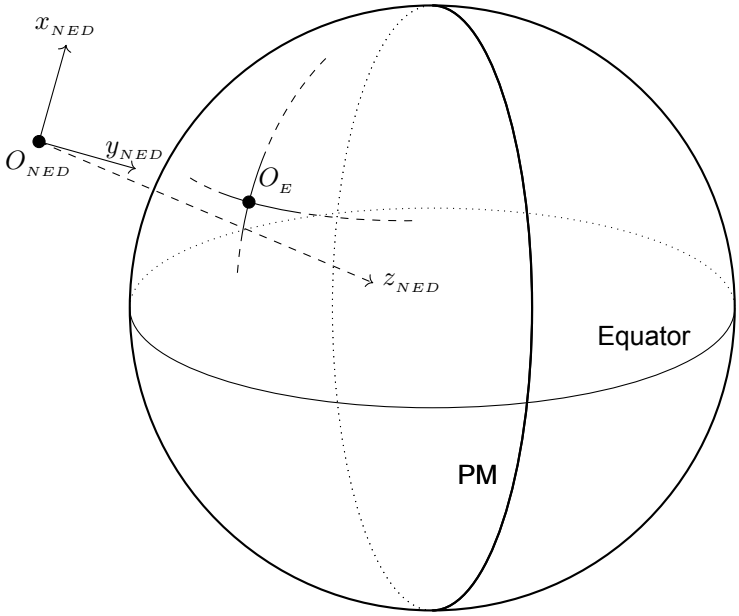

Figure D.2: NED Coordinate System: Definition of the Origin and Axes

This coordinate system specializes in describing the attitude of an aircraft to the ground, and it a popular choice for atmospheric navigation.

Aircraft Coordinate Systems

At last the body-fixed reference system can be introduced. This frame is essential in aerospace engineering because it simplifies the description of the vehicle's orientation and motion relative to its own structure, which is crucial for control, navigation, and stability analysis. The origin and axes are defined with respect to the nominal geometry of the aircraft (Durham, 2013) as opposed to a body-carried frame in which the axes can freely rotate relative to a fixed origin.

The body-fixed coordinate system is defined as follows:

- **Origin:** The origin is on the aircraft, usually (though not exclusively) at the center of gravity.
- The **x-axis**, x_B, lies along the plane of symmetry (right-left) and points forward.
- The **z-axis**, z_B, lies along the plane of symmetry (right-left) and points downward.
- The **y-axis**, y_B, perpendicular to the plane of symmetry (right-left) and points to the right wingtip.

The definition for the x-axis and z-axis are vague, leading to a number of useful sub-definitions. Two interpretations are most common: the x-axis points to the geometric nose of the aircraft, or to the direction of motion. In this report, the x-axis is defined as pointing to the nose of the aircraft.

The Body-fixed reference frame is a coordinate system attached to and moving with the aircraft. The following assumptions are commonly made when using this reference frame:

- **Rigid Body Assumption:** The aircraft is considered a rigid body, meaning that the distances between any two points on the aircraft remain constant over time. This assumption simplifies the analysis by ignoring deformations and structural flexibility.

- **Uniform Mass Distribution:** The mass distribution of the aircraft is assumed to be uniform or known. This simplifies the calculation of the center of mass and the moments of inertia.
- **Fixed Axes Orientation:** The orientation of the body-fixed axes (X, Y, Z) is fixed relative to the aircraft.
- **Negligible Aerodynamic Interactions:** The aerodynamic forces and moments are assumed to act at the center of mass or another fixed reference point. The interaction between different parts of the aircraft (e.g., wings and tail) is often simplified or neglected.
- **Inertial Reference Frame:** The Earth is often approximated as an inertial reference frame for short-duration flight dynamics studies. This means that the Earth's rotation and curvature are neglected, simplifying the transformation between the inertial and body-fixed frames.

These assumptions help to simplify the complex dynamics of an aircraft, making it feasible to analyze and design control systems. However, it is important to recognize the limitations of these assumptions and to account for them in more detailed studies or when higher accuracy is required. Indeed, in this report the assumptions that aerodynamic interactions are negligible is selectively challenged.

To complicate matters, the reference frame used to define the location of parts on an aircraft is also distinct. According to Durham (Durham, 2013), this terminology was coined by Liming in 1945 inspired by naval lingo. He defined the coordinate system when the aircraft is "rigged" as such:

- **Origin:** The origin is at the nose of the aircraft.
- The **x-axis**, also known as fuselage station, lies along the plane of symmetry (right-left) and extends parallel to the ground.
- The **z-axis**, also known as waterline, lies along the plane of symmetry (right-left) and points upward.
- The **y-axis**, also known as buttock, perpendicular to the plane of symmetry (right-left) and points toward the wingtip.

This reference frame is important to mention because the geometry of the CL-84 as obtained from (Nieusma, 1993) is defined in those terms.

E

Modal Analysis

This appendix presents the results of the modal analysis of the linearized models. The full size matrices are 8×8 with complete separation between the longitudinal and lateral-directional modes. Instead of transcribing entries full of zeros, the sensitivity matrices have been sorted into longitudinal and lateral-directional modes respectively. All flight conditions at a specified angle of wing tilt η are grouped together and color coded to identify the flight velocity conditions.

Airspeed	Longitudinal Eigenvalues			Lateral-directional Eigenvalues			
$u = -10$	5.6	-0.024 ±0.48i	-0.054		0.18 ±0.59i	-0.52	0.048
$u = -5$	8.4	-0.027 ±0.39i	-0.013		0.24 ±0.49i	-0.56	0.047
u=10	-5.6	0.024 ±0.48i	0.054		0.39 ±0.40i	-0.63	0.048
u=20	-3.8	8e-05 ±0.75i	0.27		-0.10 ±0.27i	-0.59	1.47
State	**Contribution [%]**			**State**	**Contribution [%]**		
$\dot{u}$	1.2	**35.4**	**27.9**	$\dot{v}$	**44.1**	9.5	2.3
	0.2	**13.0**	**73.9**		**37.2**	**24.1**	1.4
	1.2	**35.4**	**27.9**		**26.8**	**44.0**	2.4
	6.8	**38.8**	**15.7**		**11.6**	**52.4**	**24.5**
$\dot{w}$	5.2	**35.0**	**24.8**	$\dot{p}$	**21.8**	**45.7**	**10.7**
	2.1	**42.6**	**12.7**		**28.8**	**34.8**	7.6
	5.2	**35.0**	**24.8**		**43.8**	0.5	**11.9**
	9.3	**24.8**	**41.0**		**28.4**	**29.9**	**13.3**
$\dot{q}$	**91.2**	4.3	0.1	$\dot{r}$	**12.6**	**16.9**	**57.9**
	93.5	3.2	0		9.5	3.3	**77.7**
	91.2	4.3	0.1		**17.4**	3.7	**61.5**
	81.3	9	0.7		**40.8**	**10.2**	8.2
$\dot{\theta}$	6.2	**40.9**	**12.0**	$\dot{\phi}$	**19.1**	**27.8**	**34.0**
	3.8	**46.1**	4.1		**26.6**	**25.9**	**21.0**
	6.2	**40.9**	**12.0**		**24.5**	**17.2**	**33.8**
	9.7	**32.6**	**25.1**		**35.3**	**26.8**	2.7

Table E.1: Sensitivity matrix at $\eta = 85°$

Airspeed	Longitudinal Eigenvalues			Lateral-directional Eigenvalues			
$u=-10$	6.0	-0.054 ±0.59i	-0.045		-0.67	0.11 ±0.61i	0.096
$u=-5$	9.9	-0.056 ±0.53i	-0.011		-0.69	0.15 ±0.49i	0.099
$u=10$	-6.0	0.054 ±0.59i	0.045		-0.57	0.52 ±0.42i	-0.099
$u=20$	-3.8	0.058 ±0.81i	0.26		-0.75	0.08 ±0.12i	1.6
State	**Contribution [%]**			**State**	**Contribution [%]**		
$\dot{u}$	1.1	**23.5**	**51.9**	$\dot{v}$	8.2	**44.9**	2
	0.1	7.2	**85.5**		**19.2**	**29.8**	1.2
	1.1	**23.5**	**51.9**		**48.9**	**23.0**	5
	8.7	**40.8**	9.7		**59.8**	5	**30.2**
$\dot{w}$	6.2	**36.7**	**20.5**	$\dot{p}$	**53.2**	**13.0**	**20.8**
	2.2	**44.4**	9.1		**44.3**	**20.3**	**15.2**
	6.2	**36.7**	**20.5**		7.7	**36.1**	**20.0**
	9.9	**25.5**	**39.2**		**15.8**	**30.6**	**22.9**
$\dot{q}$	**90.5**	4.7	0	$\dot{r}$	**12.0**	**15.1**	**57.9**
	93.4	3.3	0		0.2	**12.0**	**75.8**
	90.5	4.7	0		5.9	**14.6**	**64.8**
	79.2	**10.1**	0.6		2.6	**46.2**	5
$\dot{\theta}$	6.8	**41.9**	9.4	$\dot{\phi}$	**25.0**	**23.4**	**28.2**
	3.9	**46.6**	2.9		**21.2**	**29.5**	**19.8**
	6.8	**41.9**	9.4		**23.0**	**23.7**	**29.6**
	9.9	**32.9**	**24.4**		9.6	**43.9**	0.027

Table E.2: Sensitivity matrix at $\eta = 80°$

Airspeed	Longitudinal Eigenvalues			Lateral-directional Eigenvalues			
$u=22$	-2.7	0.6 ±1.1i	0.31		4.9	-1.3	0.97	0.11
$u=30$	-1.8	0.9 ±1.2i	0.39		5.5	-1.8	1.4	0.01
$u=40$	-1.4	1.3 ±1.2i	0.05		3.7	-2.3	1.6	-0.09
$u=58$	-1.4	1.6 ±1.3i	0.76		5.3	-3.0	1.4	-0.10
State	**Contribution [%]**			**State**	**Contribution [%]**			
$\dot{u}$	**16.3**	**27.5**	**28.6**	$\dot{v}$	1.6	**42.0**	**53.8**	2.7
	34.4	**31.7**	2.2		2.6	**45.2**	**52.0**	0.2
	39.8	**27.4**	5.4		**16.7**	**47.4**	**35.2**	0.6
	30.8	**25.5**	**18.2**		**24.7**	**50.8**	**24.1**	0.5
$\dot{w}$	**14.8**	**27.3**	**30.7**	$\dot{p}$	**93.2**	3.1	3.1	0.7
	12.1	**22.5**	**42.9**		**91.6**	3.1	5.3	0
	13.9	**15.0**	**56.1**		**65.7**	5.1	**28.6**	0.5
	22.1	**20.1**	**37.6**		**47.4**	**10.2**	**42.0**	0.4
$\dot{q}$	**53.8**	**22.7**	0.8	$\dot{r}$	0.1	**49.8**	**31.8**	**18.3**
	31.1	**34.0**	0.9		0.8	**53.7**	**33.4**	**12.1**
	17.8	**41.1**	0.1		**12.4**	**56.9**	**17.2**	**13.5**
	12.3	**43.1**	1.5		**16.0**	**62.0**	**12.7**	9.3
$\dot{\theta}$	**10.8**	**34.1**	**21.0**	$\dot{\phi}$	1	8.9	7.9	**82.2**
	5.5	**35.9**	**22.7**		1	4.2	8.6	**86.2**
	49.5	**20.7**	9.1		3.1	1.4	**14.4**	**81.2**
	34.1	**19.6**	**26.8**		0.8	0.2	9.7	**89.2**

Table E.3: Sensitivity matrix at $\eta = 41°$

Airspeed	Longitudinal Eigenvalues			Lateral-directional Eigenvalues			
u=42	-1.2	1.4 ±1.0i	0.49	4.5	-2.6	1.9	-0.04
u=50	-1.2	1.6 ±0.9i	0.58	4.9	-3.0	2.1	-0.06
u=60	-1.2	1.9 ±0.8i	0.74	6.3	-3.5	2.3	-0.06
u=75	-1.2	2.1 ±0.4i	0.96	7.5	-4.3	2.6	-0.06

State	Contribution [%]			State	Contribution [%]			
$\dot{u}$	**41.0**	**29.4**	0.2	$\dot{v}$	7.5	**45.3**	**46.8**	0.3
	38.5	**30.6**	0.3		**13.1**	**46.2**	**40.3**	0.4
	32.4	**29.7**	8.2		**13.0**	**46.7**	**39.9**	0.4
	17.4	**39.0**	4.7		**16.1**	**47.4**	**36.2**	0.3
$\dot{w}$	2.6	6	**85.4**	$\dot{p}$	**84.5**	2.7	**12.7**	0.1
	7.6	6.2	**79.9**		**73.2**	4.1	**22.6**	0.1
	16.6	**27.2**	**29.0**		**71,8**	5.1	**23.0**	0.1
	13.1	**28.1**	**30.6**		**65.3**	6.4	**28.3**	0.1
$\dot{q}$	**13.9**	**43.0**	0.1	$\dot{r}$	5.7	**55.6**	**29.1**	9.6
	10.5	**44.6**	0.2		9.1	**57.1**	**25.6**	8.2
	7.4	**46.2**	0.2		7.9	**58.4**	**28.1**	5.6
	2.6	**48.4**	0.6		9.7	**59.6**	**26.7**	0.4
$\dot{\theta}$	**32.2**	**27.8**	**12.3**	$\dot{\phi}$	2.6	1.8	**10.0**	**85.5**
	28.9	**26.2**	**18.6**		2.1	1.2	9	**87.7**
	37.4	**25.1**	**12.5**		1.1	0.6	6.2	**92.2**
	24.5	**23.4**	**28.7**		0.7	0.3	4.6	**94.4**

Table E.4: Sensitivity matrix at $\eta = 28°$

Airspeed	Longitudinal Eigenvalues			Lateral-directional Eigenvalues			
u=60	-0.9	0.8 ±0.2i	5.3	6.0	-3.8	2.8	-0.01
u=70	-1.2	1.9 ±0.8i	0.83	7.6	-4.4	3.2	-0.02
u=80	-1.5	1.6 ±1.3i	0.93	8.8	-4.9	3.7	-0.02
u=90	-1.6	1.4 ±1.4i	1.0	9.9	-5.6	4.0	-0.02

State	Contribution [%]			State	Contribution [%]			
$\dot{u}$	**43.8**	**27.5**	1.2	$\dot{v}$	7.4	**44.7**	**47.8**	0.1
	33.6	**32.3**	1.8		7	**44.9**	**48.0**	0.1
	38.2	**29.1**	3.5		7.3	**45.0**	**47.6**	0.1
	36.5	**30.2**	3		7.9	**45.2**	**46.9**	0.1
$\dot{w}$	7.7	9.3	**41.5**	$\dot{p}$	**85.4**	2.1	**12.5**	0
	8.7	**39.7**	**11.8**		**85.3**	2.4	**12.3**	0
	14.9	**34.4**	**16.3**		**84.3**	2.7	**13.0**	0
	16.1	**31.8**	**20.3**		**82.9**	3	**14.1**	0
$\dot{q}$	5.9	4.4	**85.3**	$\dot{r}$	5.2	**56.3**	**33.5**	4.9
	7.4	**46.2**	0.2		4.3	**56.9**	**35.3**	3.4
	16.7	**41.4**	0.5		4.2	**57.3**	**35.8**	2.6
	20.7	**39.5**	0.4		4.5	**57.6**	**35.8**	2.1
$\dot{\theta}$	3.9	8.5	**43.8**	$\dot{\phi}$	1.7	1.1	5.4	**91.8**
	26.3	**23.5**	**26.6**		0.9	0.7	3.7	**94.7**
	19.0	**26.3**	**28.3**		0.6	0.5	2.8	**96.0**
	18.8	**26.3**	**28.6**		0.5	0.4	2.3	**96.8**

Table E.5: Sensitivity matrix at $\eta = 14°$

Airspeed	Longitudinal Eigenvalues				Lateral-directional Eigenvalues				
u=120	8.2	1.5	-0.23	0.21		-7.7	13.2	6.0	0.002
u=140	9.7	1.8	-0.23	0.19		-8.9	15.3	6.9	0.0006
u=160	11.2	2.0	-0.22	0.19		-10.2	17.4	7.9	-2.2e-05
u=180	12.7	2.3	-0.22	0.19		-11.5	19.5	8.8	-0.0003

State	Contribution [%]				State	Contribution [%]			
$\dot{u}$	0	0.1	**52.3**	**47.6**	$\dot{v}$	**44.1**	3.4	**52.5**	0
	0	0.1	**53.6**	**46.3**		**44.1**	3.9	**51.9**	0
	0	0.1	**54.7**	**45.2**		**44.2**	4.3	**51.5**	0
	0	0.1	**55.7**	**44.3**		**44.2**	4.5	**51.2**	0
$\dot{w}$	**13.1**	**30.7**	**25.3**	**31.0**	$\dot{p}$	1	**93.0**	6	0
	12.6	**31.6**	**24.3**	**31.4**		1.2	**91.9**	6.9	0
	12.2	**32.6**	**23.4**	**31.8**		1.3	**91.1**	7.6	0
	12.0	**33.3**	**22.7**	**32.1**		1.4	**90.6**	8	0
$\dot{q}$	**97.0**	0.4	1.2	1.4	$\dot{r}$	**56.7**	2	**40.3**	1
	97.5	0.3	1	1.1		**56.9**	2.2	**40.2**	0.8
	97.9	0.3	0.8	0.9		**57.0**	2.4	**40.1**	0.6
	98.2	0.3	0.7	0.8		**57.0**	2.5	**40.0**	0.5
$\dot{\theta}$	**13.1**	**69.4**	7.4	**10.2**	$\dot{\phi}$	0.3	0.3	1.1	**98.3**
	12.6	**68.4**	7.7	**11.4**		0.2	0.2	0.8	**98.7**
	12.2	**67.5**	7.9	**12.4**		0.2	0.2	0.6	**99.0**
	11.9	**66.8**	8.1	**13.2**		0.1	0.1	0.5	**99.2**

Table E.6: Sensitivity matrix at $\eta = 0°$